UNIVERSITY OF CALIFORNIA,
IRVINE

Magnetization dynamics in $Pt/Ni_{80}Fe_{20}$ nanowires induced by spin Hall effect

DISSERTATION

submitted in partial satisfaction of the requirements
for the degree of

DOCTOR OF PHILOSOPHY

in Physics

by

Liu Yang

Dissertation Committee:
Professor Ilya Krivorotov, Chair
Professor Philip Collins
Professor Jing Xia

2015

DEDICATION

To

my family:
Xuehua Yang, Yuxiang Liu and Guang Yang

TABLE OF CONTENTS

LIST OF FIGURES

Page

LIST OF TABLES

ACKNOWLEDGMENTS

I would like to express the deepest appreciation to my committee chair, Professor Ilya Krivorotov. He has great knowledge of physics and sharp insights into problem solving, and it is always a pleasure discussing with him, either it be physics topics or other topics. In his group, I have had the opportunity to collaborate with some of the very best experimental and theoretical physicists in the field, and to work with the very best leaders in the field in industry including Intel, Samsung, Micron and HGST. Without his guidance and persistent help this dissertation would not have been possible. I would like to thank my committee members, Professor Philip Collins and Jing Xia.

I also like to thank all the individuals in Ilya's group I was lucky enough to spent the last 5~6 years with: Xiao Cheng, Jian Zhu, Graham Rowlands, Zheng Duan, Igor Barsukov, Brian Youngblood, Yu-Jin Chen, Andrew Smith, Han Kyu Lee, Jenru Chen, Jieyi Zhang, Alejandro Jara, Chris Safranski, Josh Dill, Chengcen Sha, Alexandre Goncalves, Riccardo Tomasello and Tobias Schneider. I enjoyed discussing physics and sharing the lab space with them. I also want to thank all my other friends here at UC Irvine that have always been there for me. Ph.D. was not easy, but you guys made it easier.

I also want to acknowledge my collaborators including Jurgen Linder, Vladislav E. Demidov, Sergej O. Demokritov, Roman Verba, Vasil Tiberkevich, Andrei N. Slavin and Rodrigo Arias. I also want to acknowledge my managers Dehua Han and Robert Beach for their guidance and mentorship during my summer internships at Western Digital and Samsung.

CURRICULUM VITAE

Liu Yang

Education

2008	Exchange student, City University of Hong Kong
2009	Bachelor of Science in Physics, Nanjing University
2009	Visiting Researcher, National Taiwan University
2011	Master of Science in Physics, University of California, Irvine
2015	Ph.D. in Physics, University of California, Irvine

Research

Research Intern, Western Digital, Jun ~ Sep, 2013

- Fabricated DOE thin film wafers with different materials using different tools and process conditions
- Statistically characterized magnetic and mechanical properties of the deposited thin films (TEM, VSM, MOKE, FMR, stress, XRF, uniformity, etc.)
- Clarified effects of materials and process conditions on film properties and optimized magnetic thin film material and fabrication condition for next generation of high speed hard drives

Research Intern, Samsung Semiconductor, Jul ~ Sep, 2014

- Designed and built magneto-optical-Kerr-effect (MOKE) instrument system involving hardware, software, mechanical, optical and RF components, which

quantifies polarization change of laser light upon reflection off surface of nano-scale novel memory devices

- Identified main source of noise, optimized and engineered optical and mechanical system, and achieved signal-noise-ratio more than 50 times better than commercial MOKE systems
- Investigated properties of innovative nano memory devices with MOKE and analyzed results with JMP

Research Assistant, University of California, Sep 2009 ~ present

- Designed and fabricated wafer-scale non-volatile memory (NVM) devices with multiple photo/ebeam lithography, dry/wet etching, deposition, and metrology characterization steps
- Developed NVM tests protocols including magneto-transport, high speed write/read reliability, FMR spectroscopy, and sub-ns dynamics with oscilloscopes
- Discovered nanowire oscillators driven by Spin Orbit Torques, which has the highest known to date active volume in spin torque oscillators, making sharp spectral linewidth and real world application a possibility
- Proposed and implemented shape asymmetry into nanowire oscillators, which greatly improved the coherence of oscillations and overall performance of the devices
- Electrically studied parametrically excited spin wave modes in Py/Pt nanowires under the influence of spin Hall effect, which enables accurate measurement of mode dependent critical current

Selected Honors

Exchange fellowship 2008
Shun Hing Education Fund, Hong Kong

Regent's fellowship 2009-2011
UC Irvine

Best Poster Award 2013
Laboratory for Electron and X-ray Instrumentation, UC Irvine

Data Scientist fellowship 2015
The data incubator

Data Scientist fellowship 2015
Insight data science

Publications

1. A. M. Goncalves, I. Barsukov, Y.-J. Chen, L. Yang, J. A. Katine, and I. N. Krivorotov, *Spin torque ferromagnetic resonance with magnetic field modulation*. ***Appl. Phys. Lett.*** 103, 172406 (2013)

2.Z. Duan*, A. Smith*, L. Yang*, B. Youngblood* and I. N. Krivorotov. *et al. Nanowire Spin Torque Oscillator Driven by Spin Orbit Torques.* ***Nature Comm***, 5, 5616 (2014) (*equal contribution)

3. L. Yang, R. Verba, V. Tiberkevich, T. Schneider, A. Smith, Z. Duan, B. Youngblood, K. Lenz, J. Lindner, A. N. Slavin and I. N. Krivorotov *Tapered Nanowire Spin Torque Oscillator Driven by Spin Orbit Torques. Submitted to* ***Scientific Reports***

Selected Presentations

1. L. Yang, G. E. Rowlands, J. A. Katine, J. Langer, and I. N. Krivorotov, *Magnetic field dependence of spin torque switching in nanoscale magnetic tunnel junctions,* ***APS meeting****, Boston, 2012*

2. L. Yang, Z. Duan, A. Smith, B. Youngblood and I. N. Krivorotov, *Parametric resonance in Py/Pt nanowires tuned by Spin Hall Effect*, ***MMM***, Denver, 2013

3. L. Yang, Z. Duan, A. Smith, B. Youngblood and I. N. Krivorotov, *Spin Hall Effect* excited *Parametric resonance in Py/Pt nanowires*, ***APS meeting***, Denver, 2014

4. L. Yang, A. Smith, B. Youngblood, Z. Duan and I. N. Krivorotov, *Tapered Nanowire Spin Torque Oscillator Driven by Spin Orbit Torques,* ***MMM***, Honolulu, 2014

5. L. Yang, A. Smith, B. Youngblood, Z. Duan, and I. N. Krivorotov, *Tapered Nanowire Spin Torque Oscillator Driven by Spin Orbit Torques,* ***APS meeting****, San Antonio, 2015*

ABSTRACT OF THE DISSERTATION

Magnetization dynamics in Pt/$Ni_{80}Fe_{20}$ nanowires induced by the spin Hall effect

By

Liu Yang

Doctor of Philosophy in Physics

University of California, Irvine, 2015

Professor Ilya Krivorotov, Chair

Spin current is the flow of electron spin angular momentum. It can either be partially spin polarized current generated due to the exchange interactions of spins and local magnetization, or pure spin current generated from spin orbit interaction. Both sources of spin current are under intensive study for their efficient interaction with nanoscale magnetic structures, and potential application of magnetoresistive random-access memory (MRAM), spin torque nano-oscillators (STNOs) and other innovative devices.

In this dissertation, spin Hall effect mediated magnetization dynamics in Platinum/Permalloy nanowires are excited by different means and studied experimentally. This includes stead state self-oscillation of magnetization in a ferromagnetic nanowire serving as the active region of a spin torque oscillator driven by spin orbit torques. Our work demonstrate that magnetization self-oscillations can be excited in a one-dimensional magnetic system and that dimensions of the active region of spin torque oscillators, for the

first time, can be extended beyond the nanometer length scale. We also demonstrate that via proper design of the nanowire shape, which results in spatial non-uniform spin current density, we can significantly decrease the phase noise of spin orbit torque oscillators. It also stabilizes the single-mode generation regime, and points out a path for partial control of multi-mode excitation in nanostructures. We also parametrically excite magnetization dynamics in the nanowires, and it demonstrates that nonlinear dynamic magnetic effect can have a larger efficiency than the direct linear excitation in spin Hall structures, and it provides additional information about excited spin wave mode systems owing to its threshold nature that is unavailable from direct excitation.

INTRODUCTION

Magnetization dynamics historically has been mostly studied by ferromagnetic resonance [1, 2, 3, 4]. In this case a strong static magnetic field is applied to largely pin the magnetization, while a small dynamic radio-frequency field excites small magnetization motions. They are described by linearizing the Landau-Lifshitz equation around the equilibrium state and by analytically solving the linearized equation [5]. However, with the introduction of spin transfer torque and downscale of magnets [6, 7], highly nonlinear magnetization dynamics becomes a possibility. These new areas of research include stead state self-oscillation induced by spin polarized current injected in spin valves and magnetic tunnel junctions [8, 9], and strongly nonequilibrium dynamics states driven by parametric resonance in point contact devices [10]. Recently it is discovered that through spin orbit interaction in nonmagnetic heavy metals, pure spin current large enough to excite magnetization dynamics can be generated [11, 12, 13]. Besides, the pure spin currents do not require a conducting path. This provides a new possibility for previously non-accessible magnetic device design, and new means of controlling large amplitude highly nonlinear magnetization dynamics. At the same time, implementing the spin orbit torque in planar geometry raises several important physics questions. Can we fully control the magnetic damping of planar ferromagnetic structures in extended length? Can we eliminate nonlinear scattering channels to induce large angle magnetization dynamics? Can we suppress the spin wave modes competition in multi-mode excitation? Can we efficiently control the nonlinear dynamics through the control of magnetization relaxation

characteristics and excite nonlinear dynamics parametrically at relatively low microwave drive? All of these questions depend critically on our quantitative characterization and control of the dynamical characteristics of nanomagnets.

Besides the new physics, spin Hall effect induced magnetization dynamics can also lead to technological applications. It is with no doubt that data is being created at ever increasing speed and volume, usually in more and more complex and variable form, and dominantly in digital format [14,15]. The majority of data is stored in the form of magnetic medium, including PC hard disks, computer servers and digital tapes. It becomes a challenge to store, and to access, the new type of data at faster speed.

Computer hard drive storage has been keeping up with and beating Moore's Law pretty well. Cost/bit has went down by 100 million times, and cost/drive has went down 1000 times, data bit density has increased by 340 million times [16], mainly due to the introduction of giant magnetoresistance and tunneling magnetoresistance. These new designs of magnetic read heads allows order of magnitude of increase in read out signal voltage, and as a result, a possibility to decrease the storage bit size by the same order of magnitude while still maintaining the signal noise ratio. However, as storage bits shrink in size, they become thermally unstable at room temperature and there are limits to the bit down scaling. With the introduction of perpendicular recording where magnetic grains can be shrunk in plane and elongated out of plane, planar storage density keeps on increasing. For further improvement in data bit density, it requires the usage of magnetic material with higher anisotropy and will maintain high level of thermal stability, but the writing process would be harder and requires energy assist. And the entire industry is betting on heat assisted magnetic recording HAMR to work. It uses a tiny laser light on each drive

head to heat up a portion of the disk before the writing operation, and leaves the magnetic information thermally stable while unheated at room temperature, even at smaller grain size [17]. An alternative to HAMR is Microwave assisted magnetic recording (MAMR), where a drive head that emits a microwave field from a spin torque oscillator (STO) to assist the writing operation in the media [18]. MAMR is much easier than HAMR in design and fab integration, and is expected to be in final products much earlier than HAMR, providing time to perfect the design of HAMR. STOs are broadband microwave signal generators where a direct current excites and controls a magneto dynamics via the spin transfer torque effect [21, 22]. It is important because of its potential application in microwave communication, for example, where several frequency bands could be handled by a single oscillator, and in MAMR application in hard drives as pointed out before. Even though it is under intensive study, output properties of STO, especially output power and spectral linewidth, are prohibiting its application. STO is the key design of MAMR and it is highly desirable to design STOs with better performance functionality.

Besides the requirement to increase data bit density, it is also desired to develop storage with faster read and write speed. Currently, operations are more than Gb/s, and it is approaching the intrinsic oscillation frequency of magnetic materials, and magnetization dynamics, especially in nanoscale devices, is important for the design of faster hard drives.

On the other hand, computer memory is lagging behind the progression of Moore's Law. And this is important since the computer operating speed depends largely on the memory, and it has become the one of the critical bottlenecks in the progression of processing power. This is a major problem that spintronics set out to solve. Instead of using just the electric properties of electrons in electronics, spin angular momentum is also

employed to interact with magnetization, which would be faster and more energy efficient. A new kind of memory magnetoresistive random-access memory (MRAM) is proposed to replace the current SRAM and DRAM [19]. It is believed that the advantages of MRAM, mainly it's non-volatility and fast speed, is so overwhelming over other types of memory that it might eventually become dominant for all types of memory, becoming the universal memory[20]. The core component of MRAM includes a magnetic tunnel junction (MTJ). Currently there are several fundamental physics problems that are preventing the industrial level adoption of this new technology, for example how to improve switching reliability and how to decrease switching current and time, and magnetization dynamics measurement of nanodevices helps to answer these questions.

This dissertation will discuss the magnetization dynamics of Pt/$Ni_{80}Fe_{20}$ nanowires excited with the present of pure spin current, which is generated by spin Hall effect from Pt layer. It is composed of two parts, auto-oscillation and driven oscillation.

In Chapter 1, I will introduce the idea of spin current from spin filtering and spin Hall effect, and the spin transfer torque from the spin current which can excite magnetization dynamics. In Chapter 2 I will talk about the nanowire fabrication process in detail. Chapter 3 includes experimental methods. I will give a grief introduction to the experiment setup, and summarize my experience handling electrostatic discharge sensitive devices.

In Chapter 4, I will demonstrate that using spin Hall effect, we can excite for the first time, spin current driven magnetization dynamics in more than 1μm in size. The reason is some nonlinear scattering channels (four-magnon scattering for example) which can contribute to nonlinear damping and attenuate magnetization dynamics, are turned off in

our one dimensional design. It has potential to output more coherent oscillation thanks to the large oscillation volume.

In Chapter 5, we will demonstrate that using proper design of Pt/$Ni_{80}Fe_{20}$ nanowires, for example tapering the nanowire shape, we can achieve STO with better performance. This is due to the non-uniform current density, and as a result a non-uniform spin current which stabilizes the single-mode generation regime. As a result, cleaner and higher power, more coherent oscillation is achieved.

In Chapter 6 we present driven magnetic dynamics in Pt/$Ni_{80}Fe_{20}$ nanowires under the influence of spin Hall effect. This includes direct excitation of the nanowire at the resonance frequency, and parametric excitation with microwave current drive at twice the resonance frequency. It demonstrates that nonlinear dynamics in spin Hall devices can be controllably excited and provides a unique opportunity for the experimental investigation of mode dependent critical current and damping through the threshold behavior.

References

1. Arkad'ev, V. K. *J. Russ. Phys. Chem. Soc*. **44**, 165 (1912)
2. Griffiths, J. *Nature* **158**, 670 (1946)
3. Kittel, C. *Phys. Rev*. **73**, 155 (1948)
4. Vonsovskii, S. V. Ferromagnetic Resonance, *Pergamon*, *Oxford*, 1966
5. Mayergoyz, Isaak D., Giorgio Bertotti, and Claudio Serpico. Nonlinear magnetization dynamics in nanosystems. Elsevier, 2009.
6. Slonczewski, J. C. Current-driven excitation of magnetic multilayers. *J. Magn. Magn. Mater.* **159**, L1–L7 (1996).
7. Berger, L. Emission of spin waves by a magnetic multilayer traversed by a current. *Phys. Rev. B* **54**, 9353–9358 (1996).

8. Kiselev, S., et al. Microwave oscillations of a nanomagnet driven by a spin polarized current. *Nature* **425**, 380 (2003).

9. Ozyilmaz, B., Kent, A. D., Sun, J. Z., Rooks, M. J. and Koch, R. H. Current-induced excitations in single cobalt ferromagnetic layer nanopillars. *Phys. Rev. Lett*. **93**, 176604 (2004).

10. Wang, C., Seinige, H. and Tsoi, M. Current-driven parametric resonance in magnetic multilayers. *J. Phys. D: Appl. Phys*. **46** 285001 (2013)

11. Dyakonov, M. I. & Perel, V. I. Possibility of orienting electron spins with current. *JETP Lett.***13**, 467 (1971).

12. Hirsch, J. E. Spin Hall effect. *Phys. Rev. Lett.* **83**, 1834–1837 (1999).

13. Hoffmann, A. Spin Hall effects in metals. *IEEE Trans. Magn.* **49**, 5172–5193 (2013).

14. Fuller, B. R. Critical Path New York: *St Martin's Press*, (1981)

15. http://www-935.ibm.com/services/no/cio/leverage/levinfo_wp_gts_thetoxic.pdf

16. http://www.pcworld.com/article/127105/article.html

17. Kryder, M.H. et al, *Proceedings of the IEEE*, Heat Assisted Magnetic Recording, **96**, 1810 (2008)

18. Zhu, J. G., Zhu, X. and Tang, Y. Magnetics, Microwave Assisted Magnetic Recording, *IEEE Transactions*, **44**, 125 (2008)

19. Tehrani, S. et al, Progress and outlook for MRAM technology, Magnetics, *IEEE Transactions*, **35**, 2814 (1999)

20. Akerman, J. APPLIED PHYSICS: Toward a Universal Memory. *Science* **308** (5721): 508–510 (2005)

21. Sankey, J. C. et al. Spin-transfer-driven ferromagnetic resonance of individual nanomagnets. *Phys. Rev. Lett*. **96**, 227601 (2006).

22. Akerman, J. Spin Torque Oscillators. The 2014 Magnetism Roadmap, 9 (2014)

Chapter 1. Background

1.1. Spin polarized current

In ferromagnetic metal, it is energetically favorable for electrons (mostly 3d valence electrons for transition metals) to occupy one spin direction than the other spin direction due to the quantum mechanical exchange interaction according to Stoner model [1]. As a result electron bands split into majority band and minority band, with sometimes quite different density of states at the Fermi level. It follows that electric currents flowing through ferromagnetic metals are spin dependent, since only electrons with energy close to the Fermi level participate in electrical conduction process, resulting in spin polarized current.

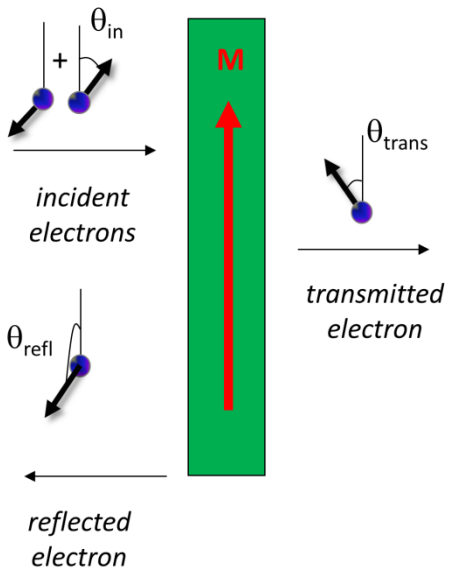

Figure 1.1 Schematic of electrons transmitting through and getting reflected from ferromagnet metal, with the transverse spin component absorbed during the process.

Following the spin-dependent scattering theory, Slonczewski and Berger predicted spin transfer torque for current flowing perpendicular to the plane of metallic multilayers [2, 3]. Assuming ballistic conditions and using WKB wave function, Slonczewski pointed out that ferromagnet magnetization changes the flow of spin angular momentum of spin polarized current, and in return, flowing spins of electrons must exert a torque on the ferromagnet with same amplitude and opposite direction [2].

M. D. Stiles and A. Zangwill showed through free-electrons models and first principles electronics structure calculations that, when Spin-transfer torques occur in magnetic heterostructures due to multiple processes of 1) spin-dependent reflection and transmission, 2) rotation of reflected and transmitted spins, 3) spatial precession of spins in the ferromagnet, when summed over all Fermi surface electrons, these processes reduce the transverse component of the transmitted and reflected spin currents to nearly zero for most systems of interest [4]. Therefore, to a good approximation, the torque on the magnetization is proportional to the transverse component of the incoming spin current.

In the end, the sign of the spin transfer torque is such as to rotate the spin-angular momentum of the electron spins toward the direction of the ferromagnet magnetization, or equivalently to rotate the magnetization of the ferromagnet toward the direction of the moment of the incoming electrons, as shown in Figure 1.2. This torque can be strong enough to reorient the magnetization of the ferromagnet, and switch the static magnetic orientation [5, 6, 7]. It can also excite magnetization dynamics and result in steady state precession following the impinging of spin polarized current [8].

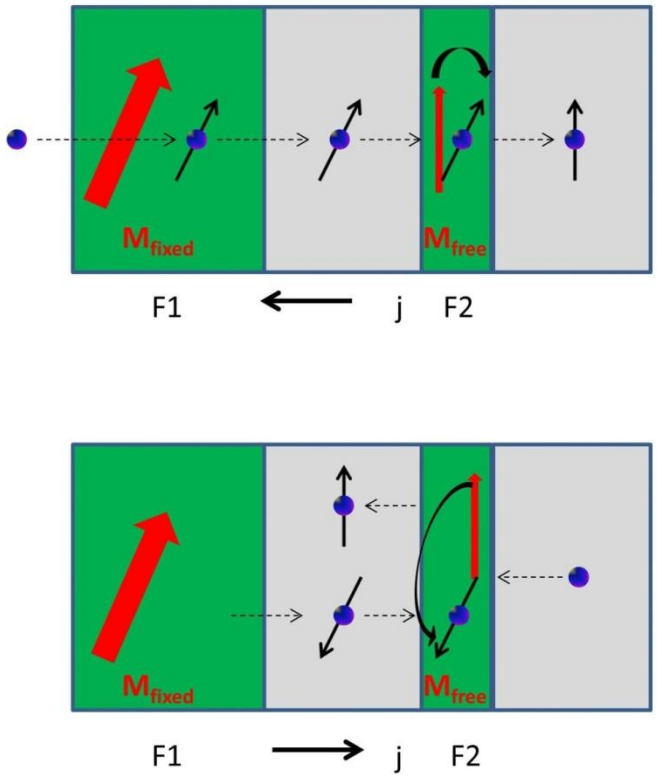

Figure 1.2 Schematic of current becoming spin polarized through F1 layer, and exerting spin transfer torque on F2 layer that prefers parallel or antiparallel magnetization direction with respect to F1 layer depending on current direction.

1.2. Magnetization dynamics with spin transfer torque

When the magnetization deviates away from equilibrium, the magnetization precesses around the instantaneous local effective field direction [9]. Landau and Lifshitz introduced the Landau-Lifshitz equation to describe the rotational precessing of magnetization in field [10]. The equation of motion can be written as

$$\frac{dM}{dt} = -\gamma\, M \times H_{eff} - \lambda\, M \times (M \times H_{eff})$$

where γ is the electron gyromagnetic ratio. H_{eff} is the effective field, which is a combination of the external magnetic field, demagnetizing field, anisotropy field and exchange field. Demagnetizing field, also called stray field, is due to the magnetic charges at the boundaries when there is component of the magnetization transverse to the surface. It has a tendency to reduce the total magnetic moment, and it is typically numerically tedious to calculate except for the special case of ellipsoids. Anisotropy field arises when the magnetization of the non-isotropic nanoparticles is energetically preferred to constrain to lie along one or more easy axes in the absence of external field. There are several sources of magnetic anisotropy, including magnetrocrystalline anisotropy arising from the atomic structure of crystal, shape anisotropy which arises when the particle shape is not perfectly spherical, magnetoeleastic anisotropy due to tension. Exchange field is a quantum effect arising from the electron-electron exchange interaction. These terms add onto the external applied field and modify the effective field. In the absence of dissipation, the magnetization distribution stays on a constant energy surface, and λ is a phenomenological damping parameter introduced to describe the energy dissipation.

In 1955 Gilbert introduced a slightly different form of damping torque[11].

$$\frac{dM}{dt} = -\gamma\, M \times H_{eff} - \frac{\alpha}{M_s}\, M \times \frac{dM}{dt}$$

Here α is the Gilbert damping parameter. These two forms are known to be equivalent and Gilbert damping term can be transformed into the Landau-Lifshitz form.

Damping of magnetization dynamics can arise from many mechanisms, including intrinsic mechanisms of the materials such as magnetoelastic scatting, or extrinsic mechanisms like two-magnon scattering from inhomogeneities.

In the case of spin-angular momentum exchange taking place in the ferromagnet, spin transfer torque arises as discussed before. This can happen when a spin polarized current passes through a magnetic layer with spin that is not collinear to the magnetization. In this case, the magnet absorbs the spin angular momentum that is transverse to its magnetization. The change of spin angular momentum exerts a torque on the spin polarized current to reorient the spin direction, and in return, there is an equal and opposite torque on the ferromagnet. This torque called spin torque can be described by the following equation.

$$\frac{d\vec{m}}{dt} = -\gamma \cdot \vec{m} \times \vec{H}_{eff} + \frac{\alpha}{|\vec{m}|} \cdot \vec{m} \times \frac{d\vec{m}}{dt} + \eta \cdot \vec{m} \times \left(\vec{m}_{fixed} \times \vec{m} \right)$$

η is the current spin polarization and $\underset{\text{m fixed}}{\rightarrow}$ is the current spin polarization direction, and the double cross term defines the direction of the spin transfer torque.

The orientations of all these torques are shown in Fig 1.3. The direction of the field torque is decided by the direction of the effective magnetic field and is perpendicular both to the effective field and the magnetization. The damping term always tends to reduce the precessional angle. The direction of the spin transfer torque is decided by the current

polarization direction. And it rotates the magnetization towards the direction of incoming electrons magnetic moments as previously stated.

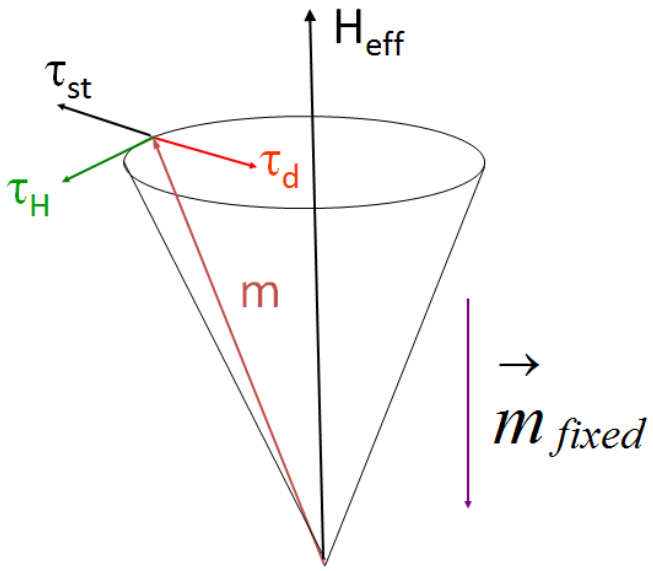

Figure 1.3 Magnetization m oscillates around effective magnetic field H_{eff} under the combined effect of field torque, damping torque and spin transfer torque.

Ralph and Stiles summarized possible dynamics of magnetization under the influence of spin transfer torque. [12] In the absence of damping or spin transfer torque, if the magnetization moment M is instantaneously tilted away from H_{eff}, then it will precess in a circle due to the field torque τ_H. If there is damping in addition to an effective field H_{eff}, the damping torque will push m back toward the low energy configuration along H_{eff}. It will precess with gradually decreasing precession angle back toward H_{eff} along a spiral path. When a spin polarized current is applied, the spin transfer torque can be either parallel to the damping torque, or antiparallel to it, depending on the sign of the current, contributing to an effective damping term. When the effective damping term is positive, m simply still spirals back to H_{eff} following any perturbation. For 0 or negative effective damping, m will spiral away from the low energy configuration with increasing precessional angle. One

possibility, which may occur if the damping torque increases with precession angle faster than the spin torque, is that the initial increase in precession angle may eventually be limited, so that M may achieve a state of dynamical equilibrium, precessing continuously at some fixed average angle in response to the direct current (see Fig. 1.4(c)). In this state, the energy gained from the spin torque during each cycle of precession is balanced by the energy lost to damping. The second possible class of spin-torque-driven magnetic dynamics is that the precession angle may be excited to ever-increasing values until eventually it reaches 180°, meaning that M is reversed. The above description is without considering the magnetic anisotropy. For real thin-film devices where magnetic anisotropy generally limits the magnetization to be close to the plane, oscillation and switching trajectory are pressed to be ellipse.

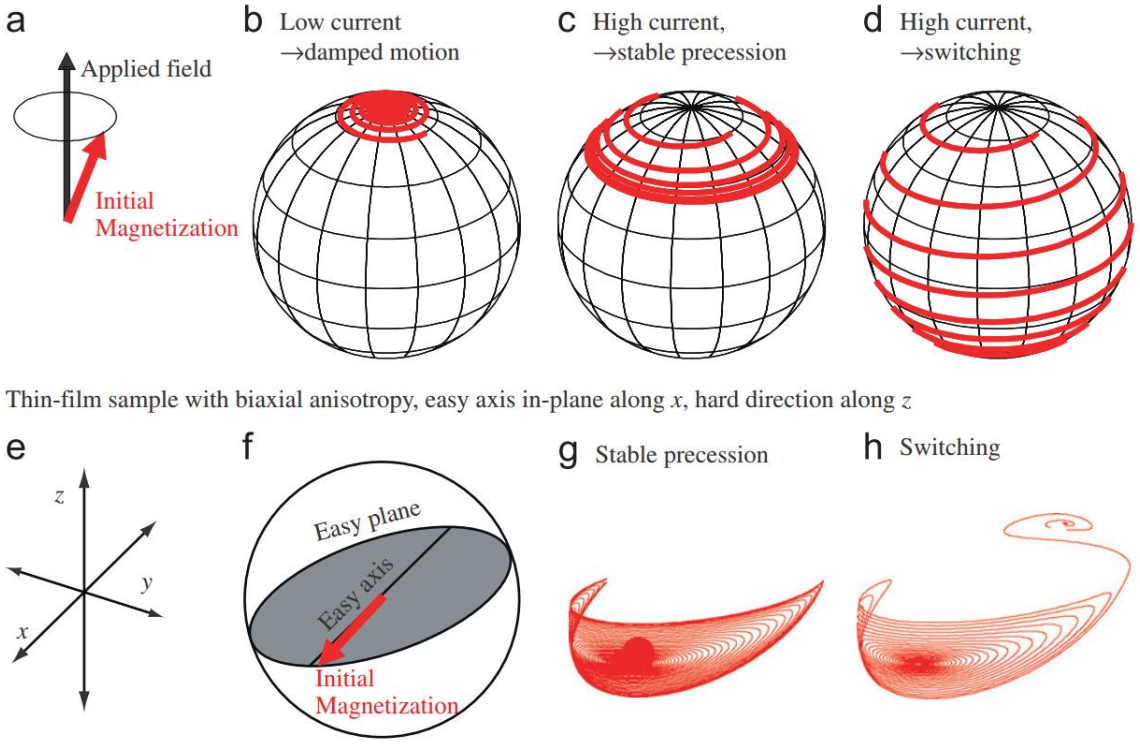

Figure 1.4 D. C. Ralph and M.D. Stiles (2008) Trajectories of spin-torque-driven dynamics for the magnetization vector M. (a) with positive effective damping (b) with stable precession (c) with switching and (e,f,g,h) considering easy plane anisotropy.

1.3. Spin orbit torques

In 1.1 we discussed the origin of spin polarized current, and it is due to spin filtering effect of electrons in ferromagnetic metal due to imbalanced density of states of spin up and spin down electrons in ferromagnets. More recently, it is recognized that non-magnetic conductors can play a more important role in the generation of pure spin current via spin Hall effects, a spin dependent scattering process.

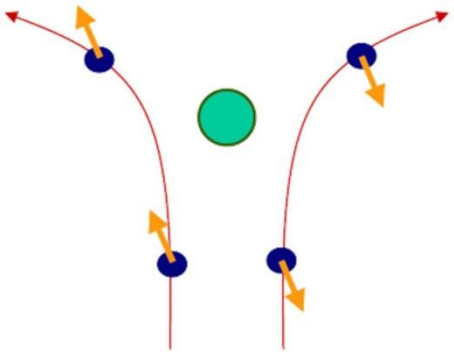

Dyakonov, Perel (1971)

Figure 1.5 Schematic of spin dependent scattering.

Edwin H. Hall first discovered in 1879 that in the presence of a magnetic field, a conductor develops a transverse voltage due to the Lorentz force experienced by the electrons and it is linear to external magnetic field. [13] He also discovered that in ferromagnetic metals, besides the linear dependence term on magnetic field, as in non-magnetic materials, there is an additional term that depends on the magnetization. This is known as anomalous Hall effect [14]. When electrons with different spin orientations move through a ferromagnetic layer, they acquire opposite transverse speed. This combined with the imbalance of majority and minority spins in ferromagnetic materials, result in a net transverse voltage. In 1971 D'yakonov and Perel' pointed out that this spin dependent scattering is the result of charge and spin currents coupling from the spin orbit

interactions, and the same transverse velocity is also present in a non-magnetic material [15]. Without the present of spin numbers imbalance in non-magnetic material, net transverse charge current is zero. However it does create spin accumulation with opposite spin polarity at opposite side of sample edges, known as spin Hall effect – the term first coined by Hirsch [16].

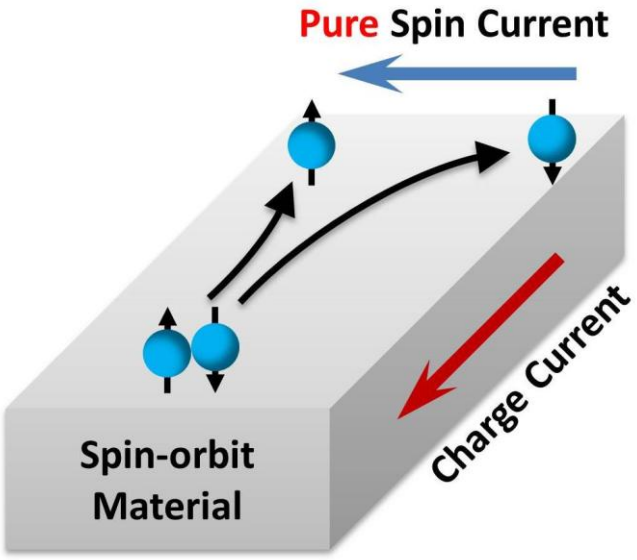

Figure 1.6 Schematic of charge current generating pure spin current in spin orbit material from spin Hall effect. Pure spin current direction is perpendicular both to the spin polarization and the charge current direction.

Only until recent few years has spin Hall effect attracted large attention, largely due to the experimental demonstration of spin dependent scattering in heavy metals large enough for practical excitation of magnetization dynamics [17, 18, 19, 20, 21, 22]. There are many mechanism that contributes to the spin dependent scattering, including intrinsic spin Hall effects due to spin-orbit coupling [23], and extrinsic spin Hall effects including spin skew and side jump scattering[24, 25]. Extrinsic mechanism refers to the acquisition of a transverse velocity during the scatting of electrons due to spin-orbit coupling. Spin skew scattering is a mechanism where the direction of the electron momentum after scattering

becomes spin-dependent. It was first proposed by Smit [24] that the spin-orbit coupling results in an effective magnetic field gradient within the scattering plane, therefore, a spin dependent scattering force. According to spin skew scattering, the spin Hall conductivity is linearly proportional to the longitudinal charge conductivity, leaving their ratio, spin Hall angle as a constant independent of impurity level. Spin skew scattering dominates the spin Hall effect in highly pure samples at low temperature. In contrast, side-jump scattering describes a spin-dependent displacement during each scattering. It is proportional to the impurity concentration, and mostly plays a small role in the spin Hall conductivity unless in alloys with high enough concentration of impurities. As a result, work has been done to increase the spin Hall effect through side jumping mechanism by doping rare earth elements into metals [29].

The intrinsic spin Hall effect describes the spin dependent transverse velocities originated from the effect of spin-orbit coupling on the electronic band structure, and it occurs generally in between scattering events instead of during the scattering. Guo et al suggested that intrinsic spin Hall conductivity is strongly temperature dependent, for example for Pt it is expected that as temperature increase, intrinsic spin Hall effect will decrease, and the same trend is observed in experiment [26, 27, 28].

Pure spin current from spin Hall effect can be described by the following formula.

$$\hat{\sigma} = \widehat{J_c} \times \hat{n}$$

Here $\widehat{J_c}$ is the charge current unit vector, and n is the unit vector that describes the spin current flow direction. $\hat{\sigma}$ describes the polarization of the pure spin current. It is clear from the equation that spin polarization is perpendicular to the charge current direction, as describe before, and it is also perpendicular to the spin current flow direction.

Similar to exchange mediated spin polarized current, pure spin current from spin Hall effect can exert a spin transfer torque on the ferromagnetic magnetization too. It can be describe by:

$$\tau_{SH} = \gamma \frac{\hbar}{2e\mu_0 M_S t_F} J_s(\hat{m} \times \hat{\sigma} \times \hat{m})$$

$\hat{m} = \frac{\vec{M}}{M_s}$ is the normalized magnetization, γ is the gyromagnetic ratio, $\hbar$ is the plank constant, e being the unit charge, μ_0 is the permeability and t_F is the thickness of the ferromagnetic layer. J_s is the pure spin current density.

Adding the spin Hall torque term τ_{SH} onto the LLG equation, we get similar equation to the LLG with spin transfer torque:

$$\frac{d\hat{m}}{dt} = -\gamma \hat{m} \times \overrightarrow{H_{eff}} + \alpha\, \hat{m} \times \frac{d\hat{m}}{dt} + \tau_{SH}$$

Due to the non-conservative nature of the injected pure spin current, it can act as damping like term, and resulting in either enhanced or damped effective damping term depending on the polarity of the pure spin current. Similar to spin transfer torque discussed previously, this spin torque can lead to the decrease of the relaxation rates of spin waves in both metallic and insulating ferromagnets [17, 18, 19, 20, 21, 22], and excite large amplitude of magnetizations including steady state self-oscillation and switching of magnetization [20, 21, 22].

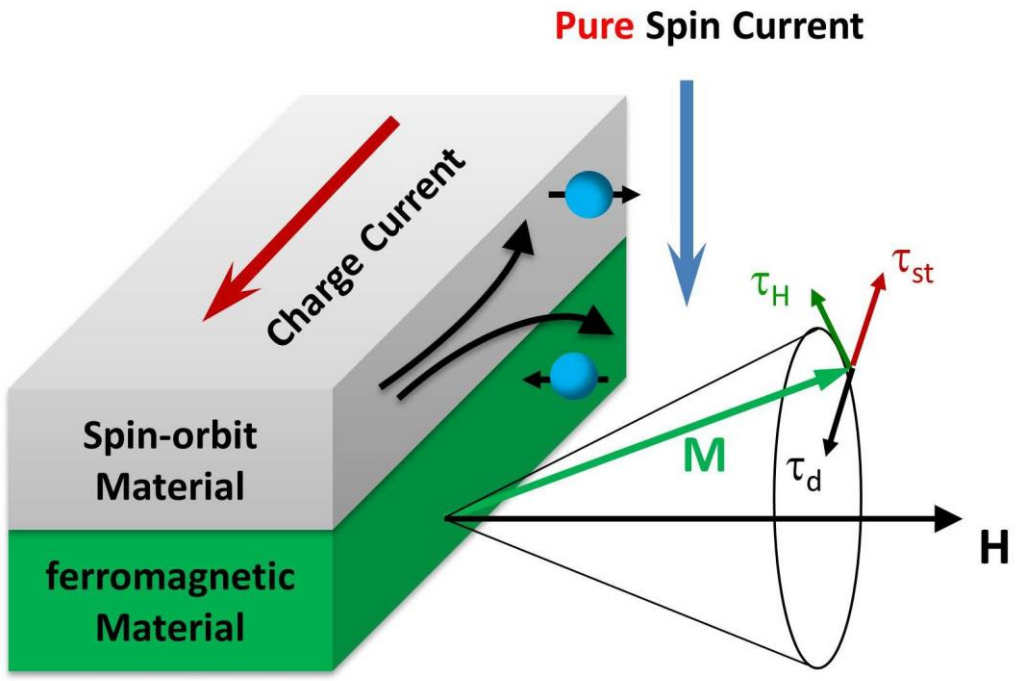

Figure 1.7 Schematic of charge current in heavy spin orbit metal generates pure spin current and inject into adjacent ferromagnetic material, modifies relaxation characteristics and driving magnetization dynamics.

1.5. References

1. E. C. Stoner. *In Magnetism and Matter*. Methuen, 1934.
2. J. C. Slonczewski. Current-driven excitation of magnetic multilayers. *J. Magn. Magn. Mater*.**159**, L1–L7 (1996).
3. L. Berger. Emission of spin waves by a magnetic multilayer traversed by a current. *Phys. Rev. B* **54**, 9353–9358 (1996).
4. M. D. Stiles and A. Zangwill. Anatomy of spin-transfer torque. *Phys. Rev. B*, **66**, 014407, (2002).
5. Z. Li and S. Zhang. Thermally assisted magnetization reversal in the presence of a spin-transfer torque. *Phys. Rev. B* **69**, 134416 (2004)
6. A. D. Kent., B. Ozvilmaz. And E. del Barco. Spin-transfer-induced precessional magnetization reversal. *Appl. Phys. Lett*. **84**, 3897 (2004)
7. Y. Huai. P. P. Nguyen. Magnetic element utilizing spin transfer and an MRAM device using the magnetic element. *US Patent* **6714444** B2
8. S. I. Kiselev, J. C. Sankey, I. N. Krivorotov, N. C. Emley, R. J. Schoelkopf, R. A. Buhrman and D. C. Ralph. Microwave oscillations of a nanomagnet driven by a spin-polarized current. *Nature* **425**, 380 (2003)
9. Charles Kittel. On the theory of ferromagnetic resonance absorption. *Phys. Rev.*, **73**(2):155–161, (1948).
10. L. Landau and E. Lifshitz. *Phys. Z. Sowjet.*, **8**:153, (1935).
11. T. L. Gilbert. *Supplementary Report*, page unpublished, May 1, (1956).
12. D.C. Ralph and M.D. Stiles. Spin transfer torques. *Journal of Magnetism and Magnetic Materials*, **320**(7):1190 – 1216, (2008).
13. E. H. Hall, On a new action of the magnet on electric currents, *Am. J. Math.*, vol. **2**, no. 3, p. 287, (1879)
14. E. H. Hall, On the "rotational coefficient" in nickel and cobalt, *Philos. Mag*., vol. **12**, no. 74, p. 157, (1881)
15. M. I. D'yakonov and V. I. Perel', Spin orientation of electrons associated with the interband absorption of light in semiconductors, *Sov. Phys. JETP*, vol. **44**, p. 1252, (1971)
16. J. E. Hirsch, Spin Hall effect, *Phys. Rev. Lett.*, vol. **83**, no. 9, p. 1834, (1999).

17. Kimura, T., Otani, Y., Sato, T., Takahashi, S. and Maekawa, S. Room-temperature reversible spin Hall effect. *Phys. Rev. Lett*. **98**, 156601 (2007)

18. Ando, K., et al. Electric manipulation of spin relaxation using the spin Hall effect. *Phys. Rev. Lett.* **101**, 036601 (2008).

19. Hahn, C., Loubens, G. de., Klein, O., Viret, M., Naletov, V. V. and Youssef, J. Ben. Comparative measurements of inverse spin Hall effects and magnetoresistance in YIG/Pt and YIG/Ta. *Phys. Rev. B.* **87**, 174417 (2013).

20. Pai, C.-F., Liu, L., Tseng, H. W., Ralph, D. C. and Buhrman, R. A. Spin transfer torque devices utilizaing the giant spin Hall effect of tungsten. *Appl. Phys. Lett.* **101**, 122404 (2012).

21. Liu, L., Pai, C.-F., Li, Y., Tseng, H. W., Ralph, D. C. and Buhrman, R. A. Spin-torque switching with the giant spin Hall effect of tantalum. *Science* **336**, 555 (2012).

22. Woo, S. -H., Mann, M., Tan, A. J., Caretta, L. and Beach, G. S. D. Enhanced spin-orbit torques in Pt/Co/Ta heterostructures. *Appl. Phys. Lett.* **105**, 212404 (2014).

23. R. Karplus and J. M. Luttinger, Hall effect in ferromagnetics, *Phys. Rev.,* vol. **95**, no. 5, p. 1154, 1954

24. J. Smit, The spontaneous Hall effect in ferromagnetics ii, *Physica*, vol. **24**, no. 1–5, p. 39, 1958.

25. L. Berger, Side-jumpmechanism for the Hall effect in ferromagnets, *Phys.Rev.B*, vol.**2**, no.11, p.4559,1970

26. G. Y. Guo, S. Murakami, T.-W. Chen, and N. Nagaosa, Intrinsic spin Hall effect in platinum: First-principles calculations, *Phys. Rev. Lett.*, vol. **100**, no. 9, p. 096401, 2008.

27. O.Mosendz, V.Vlaminck, J.E.Pearson, F.Y.Fradin, G.E.W.Bauer, S. D. Bader, and A. Hoffmann, Detection and quantification of inverse spin Hall effect from spin pumping in permalloy/normal metal bilayers, *Phys. Rev. B*, vol. **82**, no. 21, p. 214403, 2010.

28. M. Morota, Y. Niimi, K. Ohnishi, D. H. Wei, T. Tanaka, H. Kontani, T.Kimura, and Y. Otani, Indication of intrinsic spin Hall effectin4 and 5 transition metals. *Phys. Rev. B*, vol. **83**, no. 17, p. 174405, 2011.

29. Asomoza, R., Fert, A., and Reich, R. Gadolinium-heavy rare earth alloys: Preperation, metallographic study and extraordinary Hall effect. *J. Less-Common Met*., **90**, 177 (1983).

Chapter 2. $Pt/Ni_{80}Fe_{20}$ nanowire design and fabrication

We have designed and fabricated nanowire samples by two different techniques, namely liftoff and etching techniques, for the study of self-oscillation and driven oscillation in the $Pt/Ni_{80}Fe_{20}$ nanowires. They will both be described. Fabrication turnaround time for nanowires is much shorter, involving much less processes than the magnetic tunnel junctions (MTJ) fabrication described in Dr. Duan's thesis. The main reason is, for nanowires, current flows in the plane of the sample (CIP), whereas in the MTJs, current flows perpendicular to the plane of the sample (CPP). As a result, it is sufficient to apply and measure DC and RF voltage in the nanowires just with two leads at different sides on each sample. However, for the MTJs, there would be top and bottom leads in order to have CPP configuration, and a lot of additional processes are dedicated to ensure the top and bottom leads are sufficiently isolated to each other. Less fabrication processes, however, does not mean nanowire fabrication is easy. There are some issues that require special care/design in nanowires. First, nanowires have smaller cross section area, and for our purpose of dynamics excitation, it requires much higher current amplitude than MTJs. As a result, working current density in the nanowire is much higher than MTJs. This leads to the issue of sample heating, which we estimated to be around 150K even for helium cooled samples, and substrate with good thermal conductivity should be chosen. This also requires good connection, and more importantly, sufficient contact area, between the leads and the nanowire. Otherwise, current density at the connections will degrade the contact

quality very quickly. Second, signal from Pt/$Ni_{80}Fe_{20}$ nanowires is based on the Anisotropic Magnetoresistance of Py ($Ni_{80}Fe_{20}$ = Permalloy = Py) layer, which on its best performance of 1%, is still 2 orders smaller than Tunneling magnetoresistance of MTJs. This leads to much smaller measureable signal, and a requirement for careful design and optimization of the layer material and thickness, and good isolation between the sample and current shunting sources.

For both liftoff and etch defined nanowires, the fabrication process can be broken down to thin film deposition, pattern definition by e-beam lithography, nanowire formation either through liftoff or etching, and leads define. We will first quickly go through each method, and then go to more details in the fabrication process.

The etching technique is a legacy method that we do not use any more. For this technique, all layers of the Pt(5 nm)/Py(5 nm)/AlO_x(4 nm)/(GaAs substrate) samples are deposited by magnetron sputtering at room temperature. The 6 μm long nanowires are defined via e-beam lithography and Ar plasma etching using e-beam evaporated Cr mask. The Au(35 nm)/Cr(7 nm) leads with a 1.8 μm gap between them defining the active region of the nanowire are made via e-beam lithography and e-beam evaporation of the Au/ Cr bilayer followed by lift-off. The liftoff technique is the currently preferred method due to less edge magnetization damage. For this technique, the fabrication process of the AlO_x(2 nm)/Py(5 nm)/Pt(7 nm)/(c-plane sapphire substrate) samples starts with the deposition of a 5-nm thick Pt layer onto a sapphire substrate at 585 °C and annealing for 1 h at the same temperature, which results in growth of a continuous Pt film as verified by high-resolution SEM and atomic force microscopy imaging. Then the nanowire is defined on top of the Pt film via e-beam lithography, brief Ar plasma cleaning immediately followed

by in situ room temperature sputter deposition of AlO_x(2 nm)/Py(5 nm)/Pt(2 nm) trilayer and lift-off. The Au(35 nm)/Cr(7 nm) leads are defined via e-beam lithography and e-beam evaporation of the Au/Cr bilayer followed by lift-off. At the final fabrication step, Ar plasma etching is used to remove the 5-nm thick bottom Pt layer everywhere but under the Py nanowire and the Au/Cr leads.

2.1. Thin film deposition

As we mentioned before, because of the thermal conductivity of substrates, we went from Si wafer to GaAs substrates. However, GaAs does not have an unconducive oxide top layer like Si wafers, and the small band gap of 1.424 eV often makes GaAs substrate conductive, when impurities got introduced in the substrate, especially in the case of etching process to define the nanowire. This results in applied current that gets shunt, and more importantly, signal shunting that makes it hard to measure small signals. The first sample we fabricated directly on GaAs requires more than 20 mA of current into the 200nm wide sample to generate self-oscillation, because the substrate is conductive and most current applied got shunt into the substrate.

In order to solve this issue, an insulating layer needs to be introduced between the GaAs substrate and the nanowires, and we chose AlO_x. This can be done by first sputter 4 nm of Al onto the substrate, followed by a vacuum break that oxides the Al layer into AlO_x. This proves to be sufficient to isolate the substrate even in the etching steps to be followed, owing to the slow etching rate of AlO_x, and at the same time maintain smooth enough surface for the sputtering of 5 nm of $Ni_{80}Fe_{20}$ and 5 nm of Pt layer. The thickness of $Ni_{80}Fe_{20}$ and Pt is chosen so that when current is applied into the bilayer, about the same amount of

current goes into the Pt layer to generate pure spin current from spin Hall effect, and same amount goes into $Ni_{80}Fe_{20}$ layer that generate voltage signal following any magnetization dynamics from the anisotropic magnetoresistance. Pt layer is on top of $Ni_{80}Fe_{20}$ layer, protecting it from getting oxidized, and we end up with GaAs/AlO_x(4nm)/ $Ni_{80}Fe_{20}$ (5nm)/Pt(5nm) (from bottom to top) thin film stacks.

Reversed order of Pt/ $Ni_{80}Fe_{20}$ is needed because Pt is not transparent, and it is impossible to measure the dynamics of $Ni_{80}Fe_{20}$ layer using optical method through Pt cap layer of 5 nm. At the same time, AlO_x mixes with $Ni_{80}Fe_{20}$ and damages the magnetic properties, and when we put the $Ni_{80}Fe_{20}$ on the top without direct contact with the substrate, it is natural to go with sapphire substrate (C-plane single crystal Al_2O_3), which we never have to worry about conductive substrate issues.

The first attempt at making this kind of devices failed to yield working devices. And it was concluded from the measurement that spin Hall efficiency was bad. And we broke down the processes to target where the problem was. We used high resolution of Scanning Electron Microscopy (SEM) to image 3 nm of Pt grown on top of Sapphire, as shown in Fig 2.1, and it is not a continuous film. In order to solve this issue, we sputter deposit 5 nm of Pt with decreased deposition speed which increases the film quality. After the deposition of Pt at elevated temperature of 585 °C degrees, at 15% of the 50W power instead of 30% power, the sample is baked at 585°C for 1 hour, which helps with the formation of high quality continuous Pt film. As confirmed from SEM and AFM imaging, (SEM image shown), at slow deposition speed at elevated temperature followed by 1 hour high temperature baking, we end up with high quality Pt film on Sapphire.

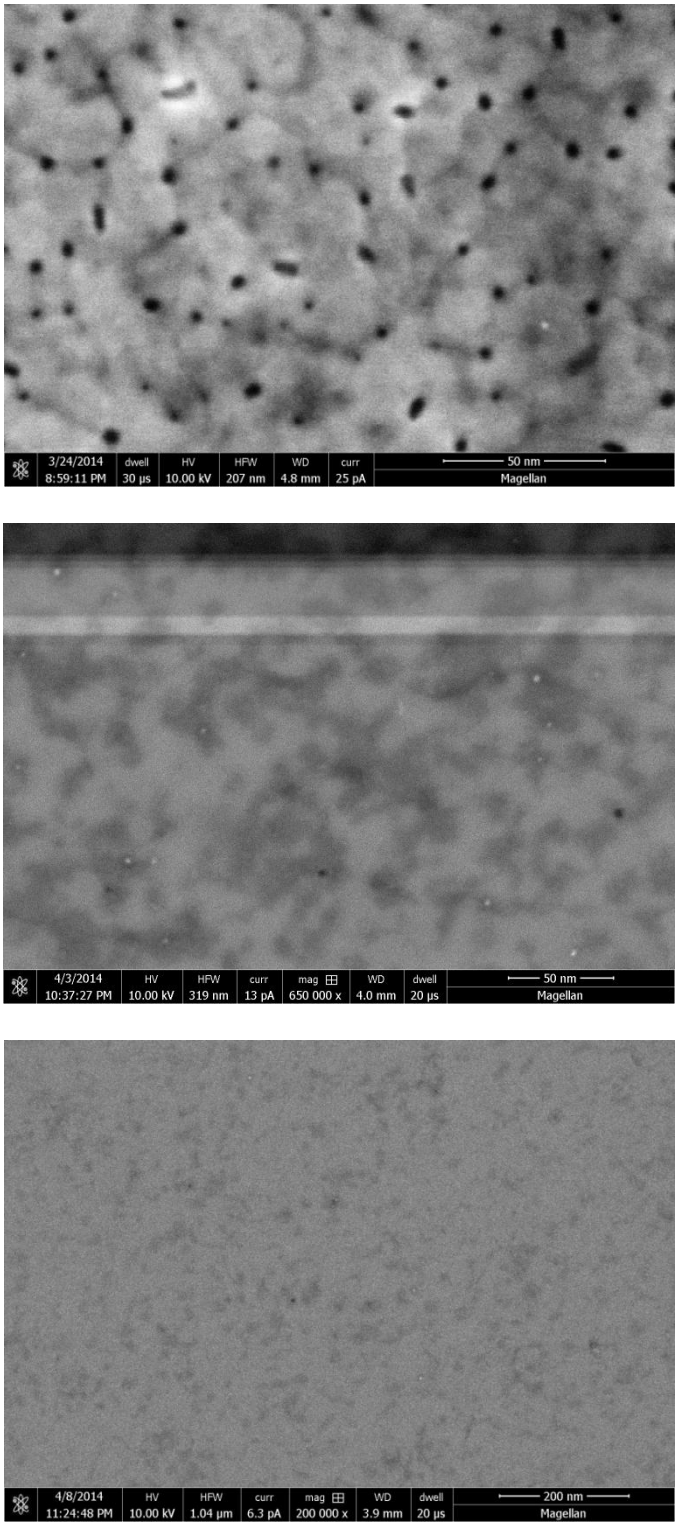

Figure 2.1 High resolution SEM images of Pt on Sapphire

(a) 3nm Pt sputtered on sapphire at room temperature with 30% power (b) 5 nm Pt sputtered on sapphire at elevated temperature with 30% power (c) 5 nm Pt sputtered on sapphire at elevated temperature with 15% power

2.2 Spin coating

The next step is definition of nanowires with e-beam lithography, and in order to do that, we have to coat the sample with ebeam resist, which is an electron-sensitive film that enables selective removal of the region either exposed (positive) or non-exposed regions (negative) by immersing it into a solvent. We mostly use PMMA in the fabrication of nanowires, which is a transparent versatile polymeric material with chains that break under exposure of high energy ebeam and can be dissolved by a solvent. First I will briefly talk about how to handle ebeam resist.

When selecting bottles for PMMA, always choose brown ones. PMMA is not very sensitive to light, but we use one bottle for half a year sometimes, and it's better to use a UV light proof bottle. We can also wrap the bottle with aluminum foil and make it more light proof but it's not necessary.

For the bottle cap, it's better to use a cap without any debris/dust that might fall into the bottle. Most bottles, however, has a low quality buffering paper inside, we'd rather use a drop bottle cap since everything is glass, even though we use disposable pipettes and do not use the dropper.

The bottle needs to be thoroughly cleaned before used for PMMA. Take off any rubber part, like in the dropper, and put everything else made of glass and hard plastic into a beaker, pour Acetone and cover the bottle, and then ultrasonic shake the beaker for 15~30 minutes. After ultrasonic shake, take the bottle out and spray with IPA inside and outside thoroughly, before blow drying with N_2. This can be done in the lab.

Bring the bottle into cleanroom environment and spray the inside of the bottle with Acetone, followed by IPA, and blow dry the bottle. Make sure the bottle is thoroughly dried inside the bottle, otherwise residue will get into PMMA.

Pour PMMA into the cleaned bottle, and wipe out the tip of both bottles for any residues before capping the bottles.

PMMA bottles needs to be upright all the time. Don't put it upside down, or rotate the bottle by 90 degrees.

When taking PMMA from the bottle, first get a disposable pipette, and clean it with a compress N_2 blow gun for any dust. Then press the tip of the pipette and release air from the pipette, dip the pipette into PMMA, and then release and PMMA will suck into the pipette. Never press the tip of the pipette when it's inside the bottle. Since air inside the pipette will go through PMMA and it will be bad for the solvent. This is important in that due to the viscosity of PMMA, air bubbles, especially small ones, will get trapped inside PMMA. When PMMA is spun on substrates, trapped air bubbles will make the coating less uniform. Also, the size of air bubbles are orders of magnitude larger than the nanoscale devices we are patterning, and at places where there is an air bubble, patterns cannot be defined.

Before ebeam lithography session, we spin coat PMMA onto the substrate. First we dice the substrate sputtered with thin film stacks from 2.1 into a small piece, usually 1X0.5 inch, which is easier to handle in our ebeam writer/SEM load lock system. After dicing, there would be debris at the cutting lines, and it is recommended to clean the sample first. Hold the sample with a tweezer, and blow with compressed N_2 gas. It is important to hold the sample with a tweezer securely so that the sample does not get blown away by

compressed N_2. Generally speaking, it is better to increase the contact area between the tweezer tips and the sample, since it makes the grip stronger, while trying to avoid contact of the tweezer to important area on the substrate surface where patterns are located. As a result, using a metal tweezer to hold one corner of the substrate is the best option. Then spray with acetone, and soak in a beaker with acetone and ultrasonic shake for 1 minute (optional). Then use a tweezer to pick up the sample by one corner from the beaker and spray with IPA, and blow dry with N_2. It is important to keep tweezers clean and stored with the caps in personal boxes, since they will be in direct contact with substrates for nanoscale patterning. To clean them, spray acetone onto a clean and fiber free wipe, and scrub the tweezer tips with the wipe, both the inside and outside of the tips, followed by the same process with IPA. The physical rubbing will clean any adhesive dust on the tweezers.

Then the sample is ready for spin coating with the following procedure.

1. Remove the foil from the spin coater. The foil is used to keep the spin coater clean, since the chemical hood is negative pressure, and air, as well as dust in air gets sucked into the hood, creating contamination 10 times or more bigger than nanodevices we are making.

2. Turn up the N_2 pressure to 60 psi. N_2 is used to prevent coating solvent from getting into the motor when spin coater is operating, and without enough N_2 pressure, spin coater will not work and display “Need CDA” on the screen.

3. Prebake the sample at higher than 100 °C for 1 minute to remove any water residue.

4. Check that the O ring is clean and the substrate is dry. It is important that in the case the O ring is dirty, cleaning should be done when the O ring is taken off the spin coater, not on the spin coater. The reason is that liquid and cleaning solvent like IPA and acetone at around the chuck tip will be sucked into the vacuum and damage the pump. And for cleaning, just spray IPA onto a clean and fiber free wipe and scrub the O ring with the wipe. New O rings are also available at around the spin coater. When the O ring is clean, place the substrate on the O ring and center it for uniform coating. Ensure that the substrate is larger than the size of the O ring. We have chucks of different sizes to accommodate different sample sizes.

5. Open the N_2 and Vacuum lines. Check that the pump is on and the N_2 tank is not empty.

6. Turn on the vacuum pressing the "vacuum" button on the keypad. Ensure that the vacuum reading on the screen is sufficient. A typical value is in the range of 18-20.

7. To deposit resist onto the substrate, first pick a new pipette from the box. Blow dry the pipette with N_2, then compress the dropper slightly and insert into the resist without touching the sides. Draw in the resist slowly avoiding injecting air into it. Remove the pipette carefully and drop the resist onto the substrate. The resist should cover the entire substrate. For small chips (1 cm by 1 cm) 2-3 drops is sufficient.

8. Close the lid to the system. (this step can be done before step 6)

9. Select the desired recipe and press the “Start” button. Spin coating recipe should be chose in accordance to thickness requirement of the resist, which can be found in Dr. Duan’s thesis.

10. Once the process is complete let the spinner come to a full stop before opening the lid. Forcing the spinner to stop will damage it.

11. To remove the sample, turn off the vacuum by pressing the “vacuum” button

12. Soft bake the coated sample at 180 °C for 45 seconds.

13. Close the vacuum and N_2 lines and set the N_2 tank pressure back to 30 psi, which is used for compressed N_2 blow dry. 60 psi is too strong and will blow the sample away from the tweezers. Close the spinner and put the foil back on top. Lower the window for the hood to prevent dust from getting in. After spin coating, sample should be stored in clean sample holders. Since the dimension of the pieces we use are arbitrary, sample holder springs cannot provide enough support of the pieces to stop them from moving around in the sample holder. As a result, we store these pieces without the springs. It’s better to be kept faced down, so that dust particles will not fall onto the surface. And if a sample holder is not clean, we can clean them with fiber free wipe sprayed with IPA, followed by compressed N_2 gas blow dry.

2.3 Ebeam lithography

After spin coating of PMMA, sample is ready for ebeam lithography to define patterns, and the first pattern to be defined are the alignment marks. This is done at Calit2 on the Magellan SEM. Using the same electron beam source and blanker, but controlled by the

Nanometer Pattern Generation System (NPGS). Electron beam is first optimized using SEM imaging, and we typically scratch a short line at the corner of the sample, to make it easier to focus and optimize the beam condition on the otherwise supposedly smooth thin film surface. For Magellan SEM, EBL is done at 30 KV voltage, 7 mm working distance.

NPGS software is installed on a different computer from the SEM imaging computer. When starting the NPGS computer, after logging in, the NPGS software will attempt to establish connection to the beam blanker, and will turn off the beam for ~ 30 seconds, and calibrate the DAC connections. It seems like this step is essential in the correct logic control of the blanker. It has happened in history many times that the NPGS computer is on and shows that it is ready for use, but the control for the blanker is turned on when it is supposed to be off and turned off when it is supposed to be on. This mostly happens when the NPGS computer and software is left on for extended period of time, and the SEM computer and software is restarted during the process, which messed up the control. As a result, I suggest restarting the NPGS computer with the SEM software on before Ebeam lithography. There are also ways to check NPGS control is functioning as it is supposed to be, which I will mention later.

After restarting the NPGS computer and the initial test, NPGS software can be initiated by double clicking the icon on the desktop. This software is the interface that controls the alignment and writing process of Ebeam lithography.

Since the size of pattern we are writing is of very different order, for example ~100nm for the nanowire and 50μm for the leads, we typically use different current magnitude of electron beam for different sizes. Smaller currents write patterns slower, but have higher resolution, and are used for fine structures like the nanowire, and bigger

currents with lower resolution but faster speed are used for less critical structures like the alignment marks and the leads. The control of current can be done manually in the SEM software, but it becomes a hassle and prevents the auto-writing processes, especially in leads patterning, where it takes up to half an hour to write one leads, and during this time we have to manually change the beam current value many times.

An alternative to control the beam current is from spotsize of NPGS. Spotsize in NPGS does not do anything in default mode. So by changing spotsize values it doesn't change our beam size. However, by changing the scope driver, we can predefine spotsize in NPGS runfile to control the beam current, so for 4 layers of different currents we can just set different spotsizes for each layer in NPGS runfile, and we don't need to change manually every 2 minutes like we did before. To change the scope driver, from options/system files/PG-CMND.sys, change the #9 line (scope driver) from scope.bat into scope2.bat, this enables spotsize to control the beam current for all runfiles in the personal folder.

SEM software gives certain values of current values from the calibration when the SEM was setup. However, we should calibrate the actual current of the beam using the Faraday Cup to make sure it is up to date. This can be done by focusing the ebeam onto the Faraday Cup center and recording the current value from the Keithley currentmeter. The correct current value can be input into the NPGS runfile, which will adjust the correct exposure time calculated from the right current.

Spotsize	SEM current	Actual current from Faraday cup
-9	1.6pA	1.45pA
-8	3.1pA	2.75pA

-7	6.3pA	6.2pA
-6	13pA	13pA
-5	25pA	26pA
-4	50pA	52.5pA
-3	100pA	105pA
-2	200pA	205.5pA

Table 1 Spotsizes with corresponding SEM currents and actual current as calibrated from Faraday cup

In table 1 we list the spotsizes in NPGS and the corresponding SEM currents, together with the latest actual beam current calibrated by Faraday Cup. Positive spotsize just corresponds to higher current. 99 spotsize means no change, which corresponds to the default current of 26pA.

After setting up the NPGS software, it is ready to use. Both pattern definition and alignment are done with the NPGS runfile and requires a pattern in the format of dc2 in DesignCAD. We have a copy of DesignCAD installed on the lab main computer. However, most group members prefer to use a free version of LayoutEditor and design patterns in format of gds, and then open it up in DesignCAD on the NPGS computer and change the format to dc2.

Finding a nanoscale device on a macroscopic chip of substrate is even harder than finding a needle in the haystack, unless we have a coordinate system to help us, and this is another use of the scratch mark at the corner of the chip, besides using it to focus the SEM beam.

Typically I zoom in onto the tip of the scratch mark, focus my SEM beam, and then move up by 1 mm. We like to make our samples on the chip with 2mm spacing in both x and y directions, due to the historical reason that the maximum size of sample we can fit in some 4-port sample holders is 2mm X 2mm.

The first step is to write alignment marks, so that when we come back to write the nanowire or leads, we have a reference to align to. How accurate the alignment is depends on the magnification when aligning the alignment mark. The more it is zoomed in, or the smaller the size of the alignment mark, better accuracy of alignment is. We typically use two sets of alignment marks, 15 μm X 5 μm L shaped alignment marks, and 2 μm X 2μm square alignment marks.

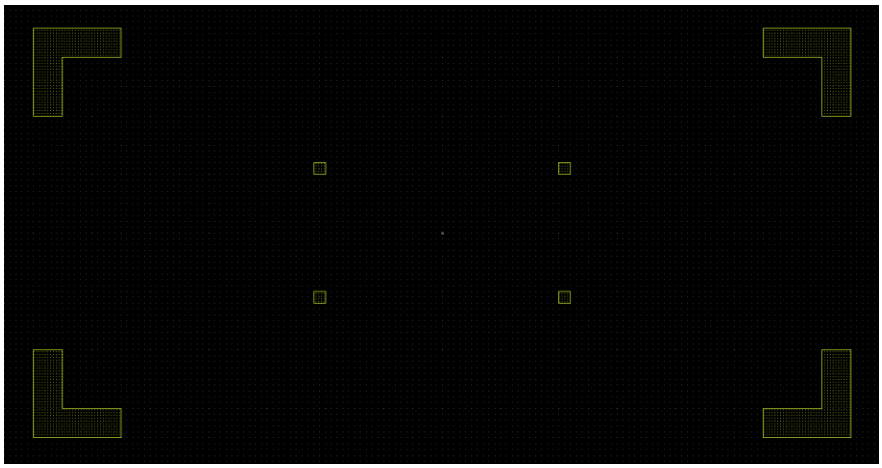

Figure 2.2 Two sets of alignment marks in LayoutEditor. Squares in the center are of size 2 μm X 2μm, and L shaped alignment marts are 15 μm in length and 5 μm in width.

The shape of patterns should be filled polygons. For polygons, ebeam just follow the contour of the polygons, not the inside of polygons. For filled polygons, ebeam sweep back and forth inside the polygon, at defined line spacing and center to center distance from the runfile, and the connected dots form the polygon.

After the pattern is designed and transferred into dc2 format, we can start building the NPGS runfile. As in the Figure 2.3, for the initial alignment marks, we want them to be equally distanced at 2 mm X 2 mm, and just choose the entity to be “array”, and select the pattern to be written and the spacing parameters. One thing that needs to be paid special attention to is NPGS calculate everything according to the center position, for example, center position of a pattern and center position of an array. As a result, we should move the stage position to the center of the desired array before the array writing step, and this can be done with the “Moveonly” entity, as shown in step 1 in the figure 2.3.

Then select the desired center to center distance, line spacing and beam current/spotsize, and area dosage. The software will calculate the exposure time using the following formula:

$$Area\ Dose = \frac{(beam\ current) \times (exposure\ time)}{(center\ to\ center) \times (line\ spacing)}$$

We typically use dosage of around 300 uc/cm^2 for PMMA. A dosage test can be done with varied values of dosage, and the best dosage that yields the same size of designed pattern can be chosen. This is essential when changing the substrate, for example from GaAs to Sapphire. Sapphire substrate is much less conductive and builds up charges easily, and requires less dosage than GaAs. Also it is noticed that when using smaller beam current, it seems like area dosage can be lowered, even when the exposure time is adjusted to accommodate the smaller beam current. For example, writing the same pattern with same dosage but different current, and the smaller current defined pattern will turn out to be bigger than the one defined by a bigger current. That is why when we do calibration of

the dosage, we use the most critical pattern (nanowires) at the current we plan to use, and stick to the same current for nanowires for all lithography.

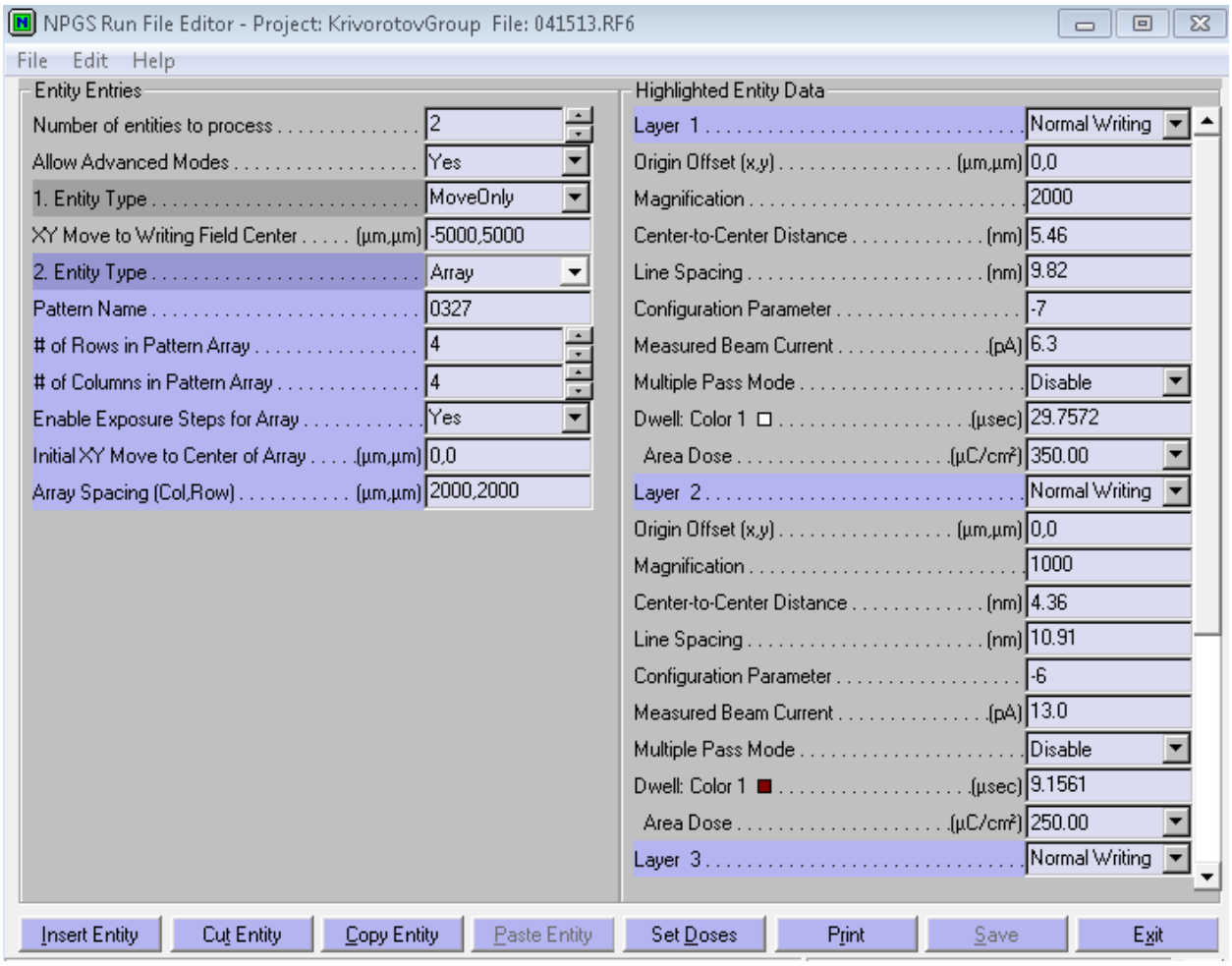

Figure 2.3 NPGS runfile for moving the stage and writing nanowires.

After the runfile is created and saved, it can be run and the NPGS will take over control of the blanker and ebeam current, and write alignment mark arrays (or any other pattern) as directed in the run file.

2.4. Development and evaporation

After the ebeam lithography step, PMMA ebeam resist can be developed in developer. We typically use MIBK:IPA=1:3 solvent and develop for 45 seconds, followed by soaking in IPA for another 45 seconds. The longer the development process, the bigger the pattern will turn out to be. And after development, regions that are exposed by ebeam (polygon area in the design) will be dissolved into the developer. And now patterns are defined on the PMMA layer it is ready for deposition.

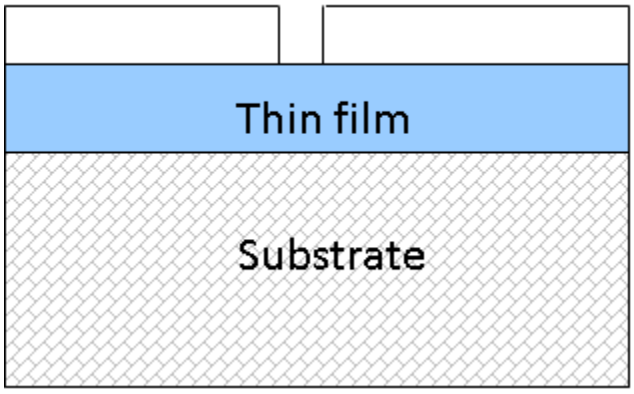

Figure 2.4 Schematic of PMMA dissolve after ebeam exposure and development

Sometimes there are residues of PMMA left behind the exposed area, and it will affect the adhesion of deposited films onto the surface. It is required to perform plasma cleaning to get rid of the organic residue before deposition.

Standard Operating Procedures: Harrick O_2

1. Log in Harrick O_2
2. Open O_2 from the back, just turn on the main valve, and do not adjust the PSI control. Turn on mechanical pump
3. Turn on power of pressure gauge from the side, pressure range should be at 6M

4. Turn on O_2 valve from the front of the door and vent, open door when positive pressure flows out and makes noise
5. Turn off O_2 valve and load sample into the chamber. Turn on pump valve after closing the door
6. After pump down to 100 mTorr, turn off pump valve, open O_2 valve again and purge chamber and then pump, back and forth a few times
7. After pumping down to 55 mTorr (Plasma can be sustained from 30 to 60 mTorr, depend on sample), turn on Power
8. Start timing when plasma is on and purple glow shows up
9. Turn off power, turn off pump,
10. Purge a few times to get rid of toxic gases
11. Open needle valve to vent, take out sample, close needle valve and pump, 100 mTorr is fine, Turn off pump
12. Turn off O_2 valve from the back, and turn down the pump
13. Log off

30 seconds of O_2 plasma cleaning is enough. Longer is not better in this case. Since O_2 plasma etches not just residues, but also PMMA on the surface that is supposed to be protecting the surface, PMMA thickness becomes thinner, making it harder to liftoff.

After O_2 plasma cleaning, we can evaporate Cr/Au alignment marks with ebeam evaporator. Cr is used as seeding layer because of its good adhesion properties, and Au is chosen because it is brightly visible under ebeam, and this is essential for alignment process, since alignment is done with alignment marks covered by more than 100 nm of PMMA, and a sharply visible material is required. Also by using the same material stack

with leads, these evaporation processes can be done together with samples that require leads deposition. The SOP of ebeam evaporator is detailed in Dr. Duan's thesis. I just want to point out a few things to be kept in mind during the operation that is not listed in Dr. Duan's thesis. First, sometimes pressure will go up during evaporation, this is due to degassing from the target. Pressure impacts the mean free path, and as a result the deposition quality. Material quality is best to be controlled so that film quality is consistent, especially in the case of etching hard mask, since etching rate strongly depends on the material quality/density. As a result, when the pressure increases during the ramping up of current, it is best to slow down a bit and wait for the pump to catch up and maintain the pressure level. It might not be very important for alignment mark and leads deposition, but it is required for hard mask deposition. Second, deposition speed is best kept at low speed, <0.5A/s for the first and last 50 A. This helps with the seeding and roughness of deposition. Slower deposition gives better adhesion and smaller surface roughness. Third, for Cr source, which is left in air for storage, it is actually mostly oxidized into CrO_x. However, the etching rate we are using seems to generate no issue of over or under etching. I think the reason is, etching rate of "Cr" is actually calibrated for a mixture of Cr and CrO_x. That is why our "Cr" etching rate is smaller than literature.

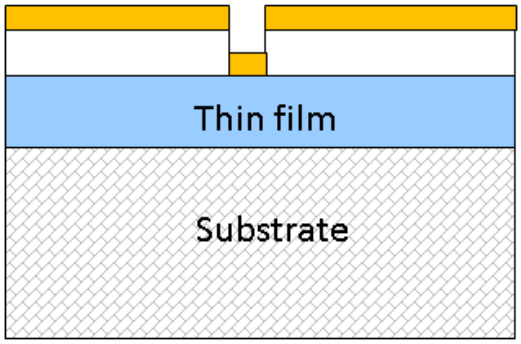

Figure 2.5 Schematic of evaporation of metal layer onto the sample after PMMA development

2.5 Liftoff

After the deposition, we can lift off the deposited part that is on top of the PMMA surface. During liftoff, they will come off into the solvent, together with the PMMA under it. The part that makes direct contact to the thin film under it, however, will remain after the lift off. To achieve best liftoff result, it is recommended that total thin film stack in evaporation step in 2.4 should be equal to or smaller than 1/3 of the PMMA thickness. If it is close to the PMMA thickness, all the evaporated thin film connects to each other through side walls, and it is hard to lift off. For thicker thin film stack, we can use 2 layers or even 3 layers of PMMA to increase PMMA thickness. Generally it is hard to liftoff smaller patterns, like nanometer scale nanowires. Below is the recommended procedure for lift off.

1. In the ideal case, first spray sample with acetone until color of unpatterned area changes when most photoresist comes off. This is the ideal case which gives the best lift off. However it takes a lot of acetone to do so. Also for some samples, it is impossible to do so (for example, thin Al_2O_3 lift off) because it requires soaking. In this case, just quickly spray the sample.

2. Soak the sample in acetone. DO NOT SOAK OVERNIGHT or for extended period of time, for example for 2 hours. This is important because soaking overnight would solve all the photoresist, and metal above PR would re-attach to the surface, and it would be impossible to lift off again. Recommended soaking time is somewhere before 30 mins to 1 hr depending on the sample.

3. Use a tweezer and pick up the sample. BEFORE acetone dries on the sample, spray with acetone on the sample to help wash off flakes.

4. Finish with IPA, N_2 blow and check under microscope.

5. If lift off is not perfect, soak in acetone, and ultrasonic shake for 10s.

6. Repeat 3, 4, 5 until lift off is good. Total ultrasonic shake time depends on the sample, and the smaller the sample, the easier it is for the sample to come off, the shorter we can ultrasonic shake since nanometer samples might come off from the substrate. In the case of nanowires, however it seems to be very adhesive and does not come off in ultrasonic shake.

7. If lift off is still bad, soak in acetone and use Q-tips and gently rub the area of sample. Finish with 4

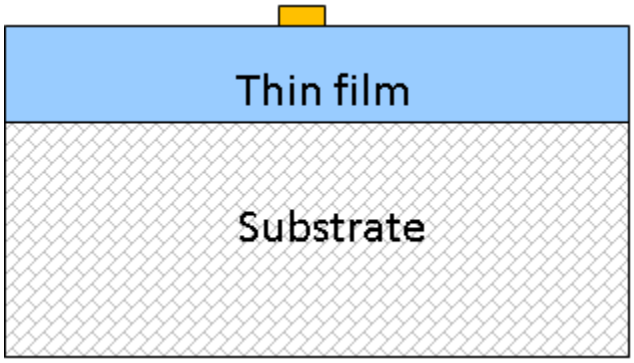

Figure 2.6 Schematic of device after liftoff

After liftoff, we end up with alignment mark arrays on the surface.

2.6. Alignment

With the alignment marks on the chip, we can start defining nanowires. First O_2 plasma clean the surface to get rid of organic residues on the surface, then spin coat PMMA as instructed in 2.2. Now for ebeam lithography, we want to align with the alignment marks so that we know where we are writing the nanowires at. This can be done by adding an entity of alignment to the NPGS runfile.

First using the scratch mark as a reference, we can roughly move to where the alignment marks are supposed to be. Then alignment marks are used to accurately pin point where nanowires should be. For the alignment step, ebeam also scans and image the sample so that we know where the sample is located at. This exposure in ebeam, however, might leave undesired regions developed due to the ebeam exposure. To solve this, we use much bigger center to center distance and line spacing value of 300 nm, as shown in Figure 2.8. In this way, we have less area dose on the PMMA surface. We end up scanning the surface with less pixels, but it is enough for the alignment of micron sized alignment marks. Also when aligning, we can scan the surface just once, instead of over and over again like in SEM imaging, to reduce the total exposure time onto PMMA. When aligning in NPGS, an "overlay" of what the alignment mark is supposed to be is displayed on the screen, together with a window of SEM scan image. This window should be big enough so that at least part of the alignment mark is visible in the window. Then using arrows to move the overlay on top of the alignment mark in the SEM scan, coordinate system of the substrate and the nanowire design is aligned, and we can start writing the nanowires.

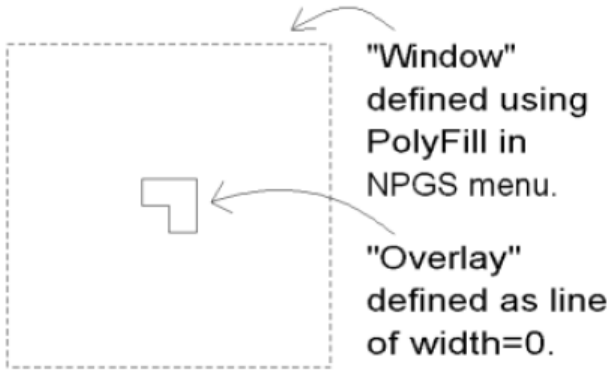

Figure 2.7 Alignment windown in NPGS with overlay of alignment mark

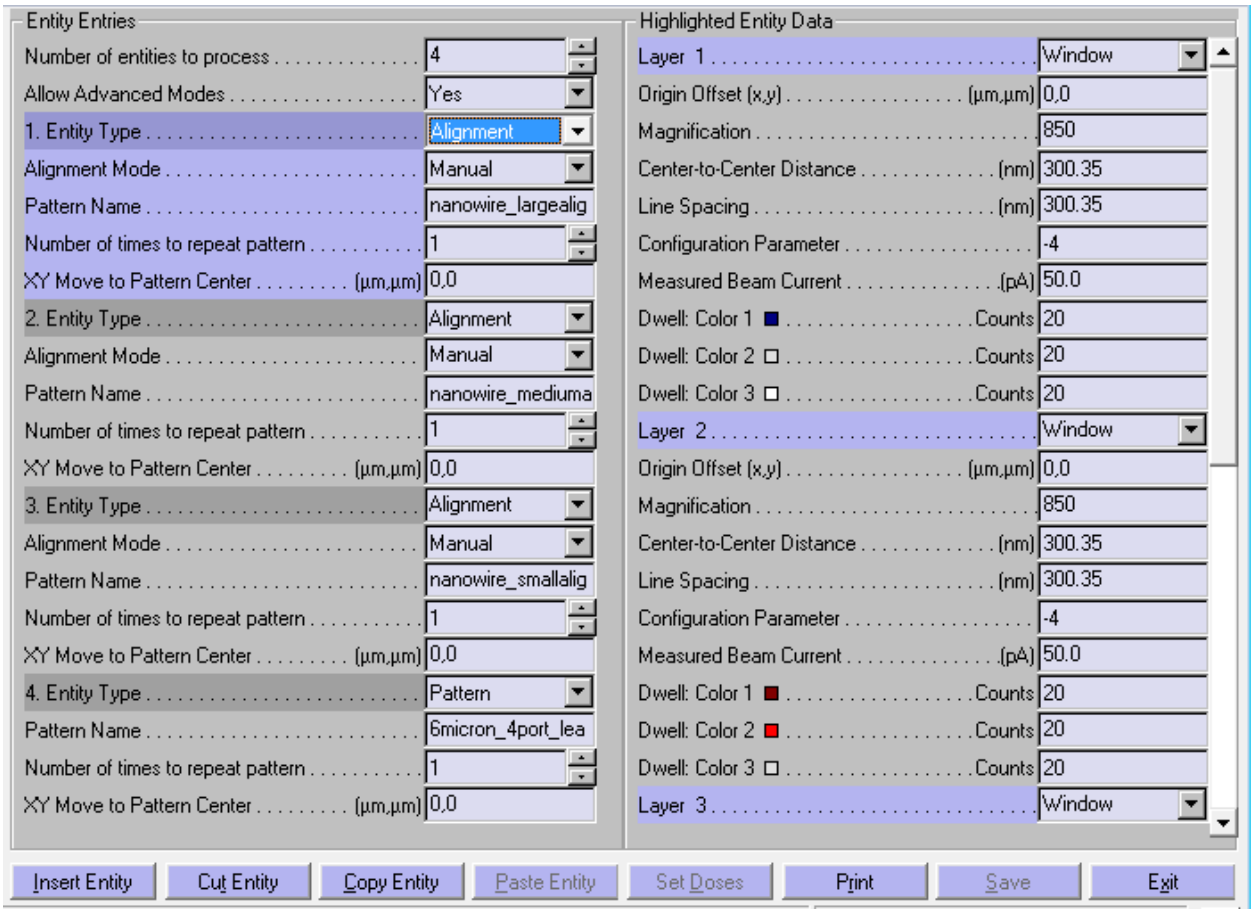

Figure 2.8 Example of NPGS runfile for alignment procedure with "Alignment" entity. Center to center distance and line spacing are kept at 300 nm to minimize ebeam dosage to PMMA during the alignment step.

Besides the alignment step, scanning window with low dosage can also be used to check if ebeam lithography is performing like it is supposed to be. This is recommended at the beginning of each ebeam lithography session, and will save hours of time in case ebeam lithography does not work, which can be frequent. Test write the alignment mark at an unimportant location, and then use alignment window to check if anything is written. If it is working, regions that are exposed to ebeam will have a blue color in contrast to the red background. This is fast and easy and so far proves to be the best way to make sure EBL is working as desired.

The biggest pattern NPGS can write once without moving the stage is the size of the scanned window. As a result, for bigger patterns like the leads, we use smaller magnification. However, for more critical patterns, like the nanowire, we zoom to the center with at least 2000 magnification, and use smaller current (for example 6.3pA), because it is sharper, and the nanometer scale pattern takes very short time to write, even for a small beam current.

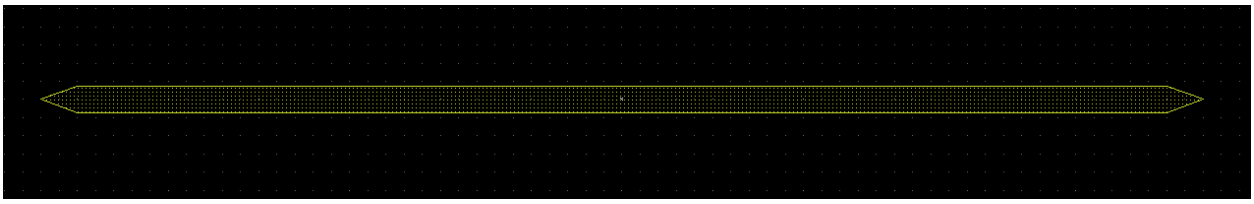

Figure 2.9 Design of 6 μm nanowire with triangle tips in LayoutEditor.

When Magellan is perfectly aligned by the engineers, the beam aperture is not supposed to change when changing the beam current. However, this is usually not the case, and the shift in beam position and condition can be large when changing the beam current. As a result, we should adjust and optimize the beam condition at the current used for the most critical feature, the nanowire (6.3pA in this case). For the nanowire, we leave the ends of a wire to be triangles to minimize the reflection of spin wave modes at the edge of the wires. It is better to use longer wires due to bigger contact area under the leads, while the active region is defined by the gap between two leads where applied current is not shunted by the leads. With an aspect ratio of 30 or higher, the nanowire is very elongated. It is better to write the nanowire with ebeam scanning parallel to the nanowire axis. When ebeam scans along the hard axis of the nanowire, there is more turning of the ebeam path which increases writing time, and also for narrow wires with width around or below 100

nm, nanowire does not develop. After the ebeam lithography, it can be developed as instructed in 2.4.

For the GaAs/AlO_x/Py/Pt samples, we are going to evaporate Cr hard mask from ebeam evaporator, and we use O_2 plasma cleaning to get rid of PMMA residues as mentioned before. Cr thickness is chosen so that it will survive the etching step later that defines the nanowire, meaning

$$thickness_{Cr} \geq \left(\frac{thickness_{Pt}}{etchingrate_{Pt}} + \frac{thickness_{Py}}{etchingrate_{Py}}\right) * etchingrate_{Cr}$$

We typically leave 30 seconds ~ 1 minute etching buffer time to ensure that we do not etch into the Pt layer under Cr.

For Sapphire/Pt thin film, we are going to sputter deposit Pt(2nm)/Py(5nm) /Al(2nm) in the sputtering system at room temperature, and the pre-deposition plasma cleaning can be done in situ with Ar plasma cleaning at 10% power for 30 seconds. Besides etching off residues of PMMA, this process also clean up the Pt layer so that good interface between Pt is formed, which is essential for spin Hall effect. After the cleaning, sputter deposit the multilayer stack at room temperature.

After evaporation, we can lift off as instructed in 2.5 to form nanowire shapes on the chip.

For Sapphire/Pt(7nm)/Py(5nm)/AlO_x(2nm), the multilayer nanowire is defined and ready to connect to leads. For GaAs/AlOx(4nm)/Py(5nm)/Pt(5nm) samples, we need to etch define the wires first. At first we used Ar plasma etching at 90% power in the sputtering system. It works, but the plasma etching is non-directional. It will damage the magnetization from the edge of the nanwires. Also it is less reliable, and the etching rate

seems to be unstable after each vacuum break. Now that we use ion milling to etch define the nanowires, it is more repeatable, and there is less edge damage to the edges of the nanowire. AlO_x in between the GaAs susbtrate and the Py/Pt thin film has a smaller etching rate in Ar plasma etching, and as a result we can pretty much always end up in the AlO_x layer when etching.

2.7. Lead definition

After the nanowires are defined, we can connect them to leads. Again this is done through PMMA spin coating, aligning to the alignment marks, writing leads and development and Cr/Au evaporation finished with liftoff, which is very similar to the alignment marks definition steps. The main difference, however, is the leads are much bigger and requires a bigger current (~200pA) to expedite the writing process. This current, which is 30 times larger than the current used for the nanowire definition, has a big beam spotsize, and when defining two leads with a 2um gap in between, the actual gap will turn out to be much smaller.

The solution to this is to define the leads step by step with 4 (or even more) current values. At first we define the first layer of leads with a relatively small current, for example 26pA, that still have a relatively small spotsize. Then we ramp up the current for the second layer, and make the first two layers connected. And then repeat for the third and fourth layer with even higher current.

We have tried two types of leads design, as shown below and different colors corresponds to different layers where different beam currents are used. It seems that squared leads liftoff better than triangular ones.

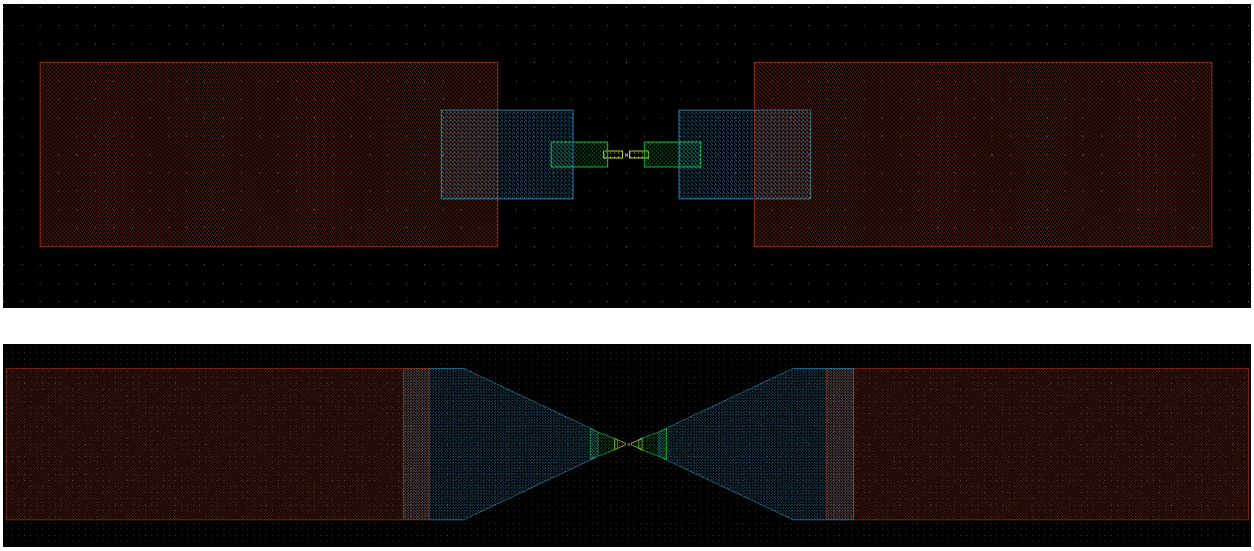

Figure 2.10 Two types of leads design in LayoutEditor. Different color of polygans corresponds to different layers with different ebeam current

As mentioned before, when changing the beam current, there might be shifts of the beam position even though it is not supposed to. And as a result, we sometimes end up with disconnected layers, making the leads non-conductive. In this case, leads with longer overlapping region between layers is preferred. Or we can redo the leads definition step and put on patches to connect the disconnected layers.

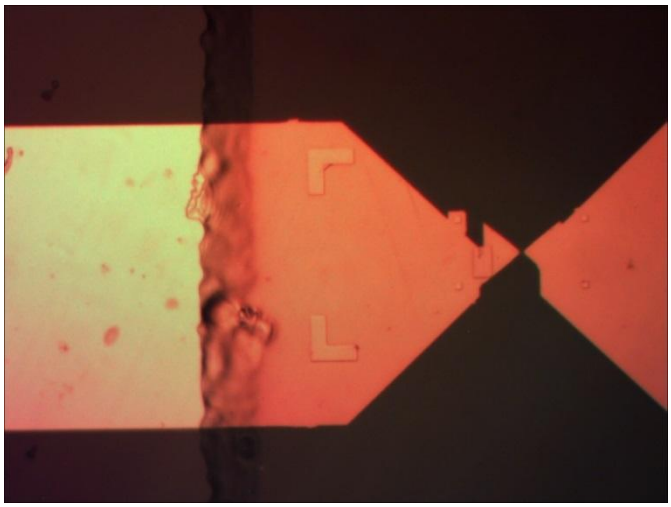

Figure 2.11 Optical image of leads where the first layer (inner most triangles) are shifted up to the right with respect to the other layers. As a result, layers are disconnected. And I patched the gap with an additional lithography step.

After leads liftoff, the GaAs/AlO_x/Py/Pt/Cr nanowire samples are ready to use. Leads are electrically connected to the wire through Cr layer, which is also conductive. For the Sapphire/Pt/Py/AlO_x nanowires, there is still Pt covered on the chip everywhere, including under the leads. We need to etch the substrate down to sapphire so that current applied and voltage signal to be read do not shunt through the Pt layer. This process, can be done with Ar plasma etching, but ion mill etching is preferred due to less edge magnetization damage. After etching, the nanowires are ready for measurement. In this case, Sapphire/Pt(5nm) extends from the nanowire out to under the leads, and current goes into the leads not from the top of the nanowire as in GaAs/AlO_x/Py/Pt/Cr samples, but through the bottom Pt layer. There is more conductive area, and it definitely works better.

2.8. Finished nanowires

Besides the 200nm wide nanowire with 1.8um gap in between the leads, we also fabricated nanowires varying the length and the width. Also nanowire with tapered shape are designed and fabricated, which will be covered in Chapter 4. We also made nanowires with a notch in the middle. All these different designs of nanowire can be processed just by changing the pattern design, while keeping the fabrication process. There are some SEM images of the nanowires that we have made.

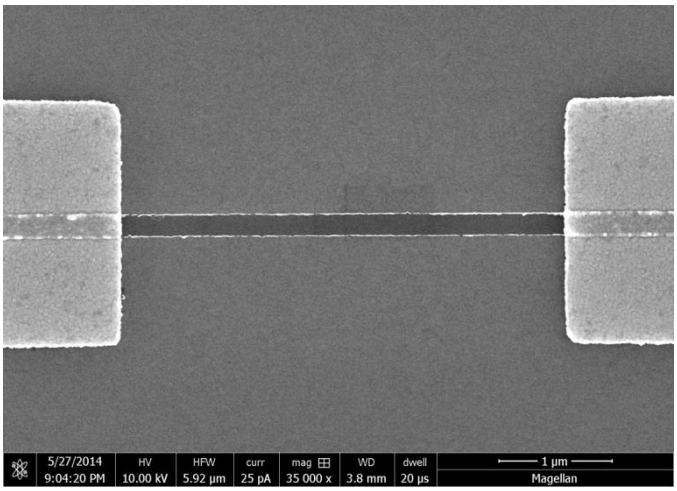

Figure 2.12 SEM image of a 4 µm long nanowire

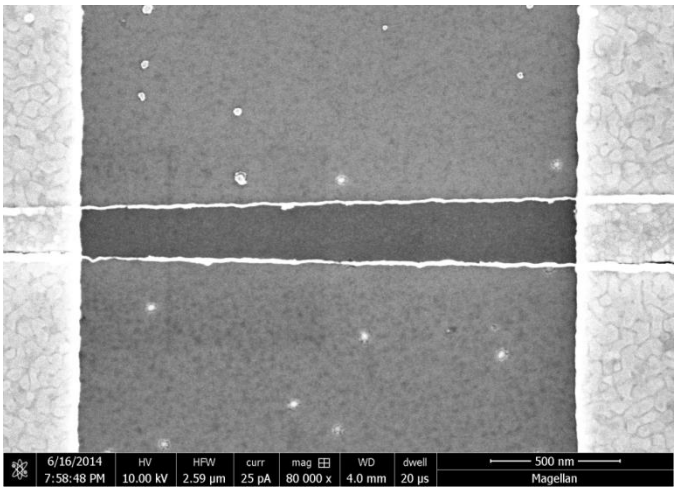

Figure 2.13 SEM image of a tapered nanowire

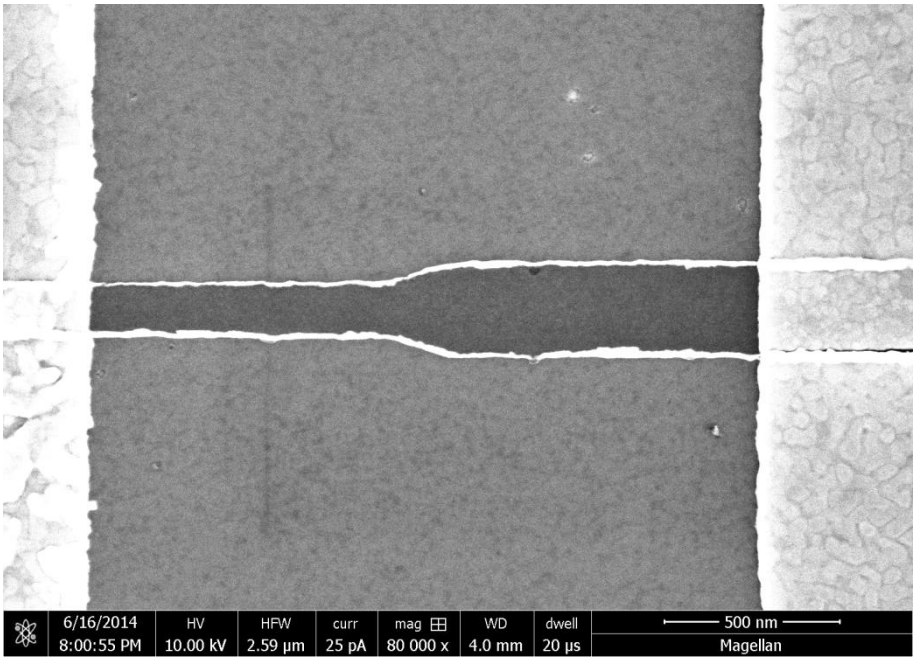

Figure 2.14 SEM image of a nanowire with a step increase of width in the middle

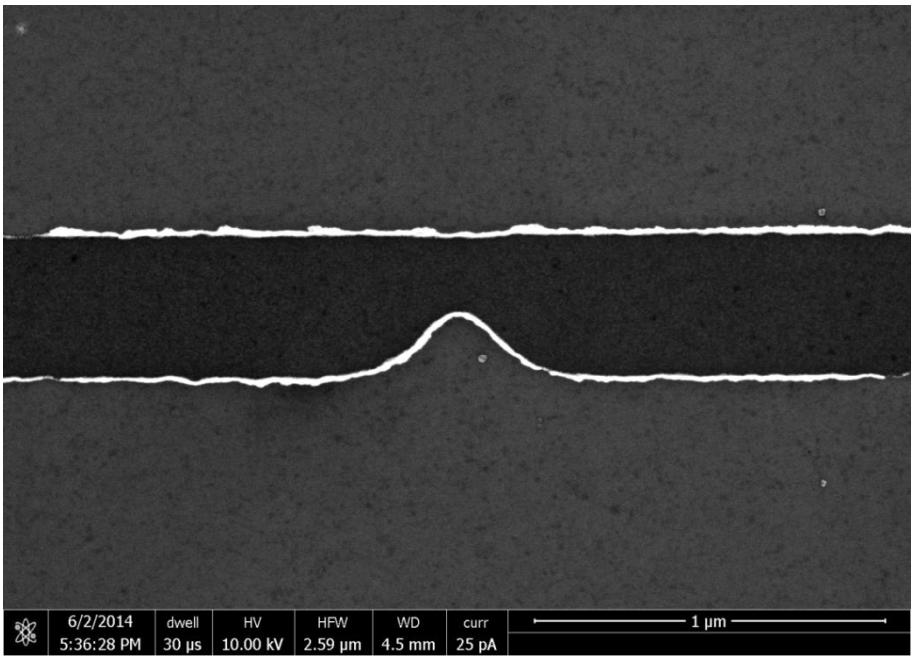

Figure 2.15 SEM image of a nanowire with a notch in the middle

Chapter 3.Experimental methods

3.1. Spin torque ferromagnetic resonance

Ferromagnetic resonance (FMR) is the main technique to study dynamical properties of magnetic materials. However, “conventional FMR detection methods lack the sensitivity to measure individual sub-100-nm-scale devices that are of interest for fundamental physics studies and for a broad range of memory and signal-processing applications” [1]. Sankey and Tulapurkar et al. demonstrated that they can excite precession not by applying an ac magnetic field as is done in other forms of FMR, but by using the ac spin-transfer torque from a spin-polarized ac current [1, 2]. When an alternating current is applied to the sample, spin transfer torque induces magnetization dynamics, leading to a changing sample resistance from the sample magnetoresistance. Alternating current and resistance get mixed and give rise to a direct voltage, which can be measured using lock-in technique. By sweeping the frequency of the applied alternating current, a peak in the direct voltage generated by the sample can be observed when the applied frequency matches the resonance frequency of the sample. This technique is called spin-torque ferromagnetic resonance [1] and has been widely used to understand magnetization dynamics induced by spin transfer torque. Analysis of the resonance frequencies, amplitudes, linewidths, and line shapes as a function of microwave power, dc current, and magnetic field provide detailed new information about the exchange, damping, and spin transfer torques that govern the dynamics in magnetic nanostructures. [1]

Fig 3.1 shows the schematic of our measurement setup, and we focus on the case of $Pt/Ni_{80}Fe_{20}$ nanowires. For ST-FMR measurement, modulated RF current is applied into the sample, which generates RF spin orbit torque and RF Oersted field. When RF frequency matches the natural resonance frequency, maximum driven oscillation amplitude is achieved, and this direct excitation is essentially spin Hall based ST-FMR [1]. More measurement details can be found in Dr. Chen's thesis. Driven Py magnetization can also be achieved parametrically when RF frequency matches not the resonance frequency, but twice the resonance frequency. Under this circumstance, RF current oscillates the effective damping and resonance frequency (from Oersted field oscillation) at twice the resonance frequency, which lowers the effective damping at the resonance frequency and can also excite magnetization dynamics. Like auto oscillation, nonlinear magnetization dynamics of parametric resonance is also a threshold effect: it only happens when RF modulation is higher than the RF threshold I_{th} and can bring the effective damping to zero, and this distinct onset behavior, together with the twice frequency drive can be used to differentiate parametric resonance from direct resonance.

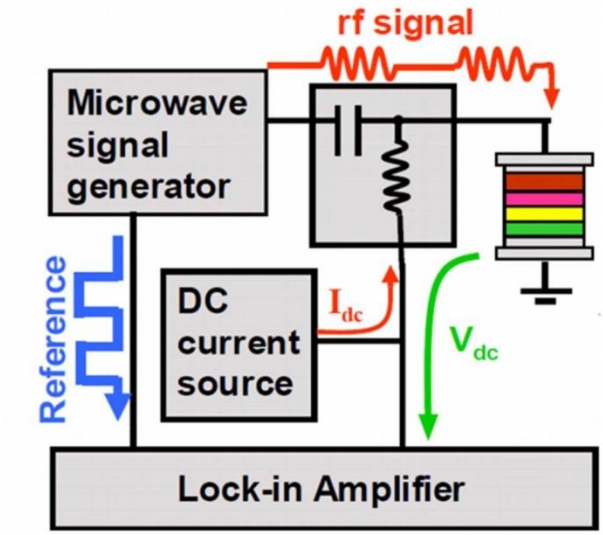

Figure 3.1 Schematic of ST-FMR measurement circuit.

First of all, the applied periodic microwave current will heat up the sample, result in a resistance change. It is called bolometric heating. However, this voltage signal is not dependent on magnetic field or frequency, and simply shifts the background of the entire signal. Second, for direct excitation, the microwave current I_{ac} applied to the nanowire excites magnetization dynamics in Py by the combined action of current-induced SO torques and the Oersted field from the current in Pt, and thereby generates AMR resistance oscillations at the frequency of the microwave drive; for parametric resonance, applied microwave current I_{ac} oscillates system parameter of effective damping and resonance frequency, achieving the same effect of Py magnetization dynamics and AMR resistance oscillations. For both cases of driven oscillation, mixing of the current and resistance oscillations as well as variation of the time-averaged sample resistance in response to the microwave drive [3] give rise to a direct voltage V_{dc} that is measured as a function of magnetic field H applied to the sample. They are known as photovoltage and photoresistance respectively. Peaks in $V_{dc}(H)$ arise from resonant excitation of spin wave eigenmodes of the nanowire.

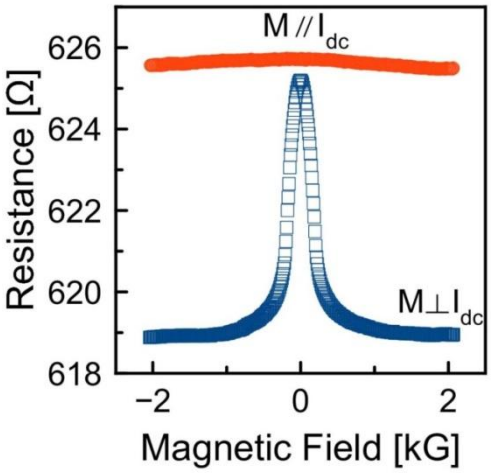

Figure 3.2 Resistance of a typical Pt/Py nanowire vs magnetic field along and perpendicular to the nanowire axis, due to anisotropic magnetoresistance, 1% in this case.

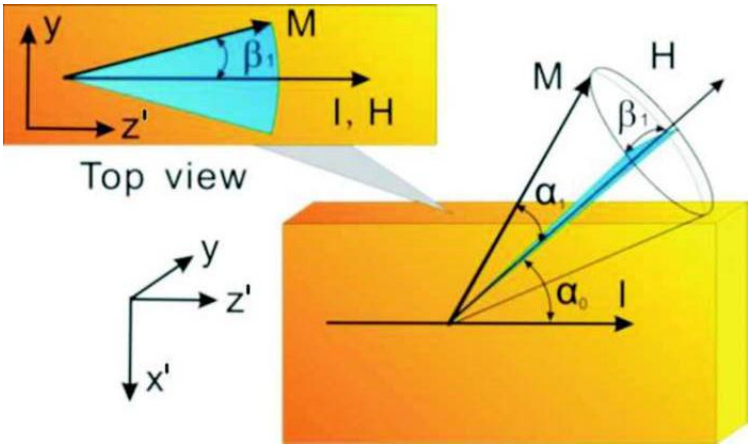

Figure 3.3 Meching, N. et al (2007) Sketch of the magnetization precession. The magnetic field H makes the angle α_0 with the current I. The magnetization oscillation toward I has the amplitude α_1 and that perpendicular to I β_1.

Here we aim to derive the mixed voltage signal for photovoltage and photoresistance in the configuration of Py nanowire for both direct excitation and parametric excitation. For anisotropic magnetoresistance, as shown in Fig 3.3, $R(t) = R_0 + R_A cos^2\theta(t)$, and θ(t) is the instantaneous angle between M and the current direction z'.

$\cos\theta(t) = \cos\alpha(t)\cos\beta(t)\,, where\ \alpha(t) = \alpha_0 + \alpha_1^t(t) = \alpha_0 + \alpha_1\cos(\omega t - \psi)\,, and\ \beta(t) = \beta_1^t(t) = -\beta_1 \sin(\omega t - \psi)$, as shown in Fig 3.3.

$cos^2\theta(t)$ can be expanded to second order in $\alpha_1\ and\ \beta_1$ [3]

$$cos^2\theta(t) \approx cos^2\alpha_0 - \alpha_1 sin2\alpha_0 \cos(\omega t - \psi) - \alpha_1^2 \cos 2\alpha_0 \cos^2(\omega t - \psi) - \beta_1^2 cos^2\alpha_0 sin^2(\omega t - \psi)$$

And as a result, for direct exciatation where $I_{ac}=I_0+I_1\cos(\omega t)$

$$U_{direct}(t) = [R_0 + R_A cos^2\theta(t)][I_0 + I_1\cos(\omega t)] = I_0(R_0 + R_A cos^2\alpha_0) - \frac{1}{2} I_1 R_A \alpha_1 sin2\alpha_0 \cos(\psi) - \frac{1}{2} I_0 R_A(\alpha_1^2 cos2\alpha_0 + \beta_1^2 cos^2\alpha_0)$$

Where $I_0(R_0 + R_A cos^2\alpha_0)$ is the bolometric voltage independent of oscillation amplitude, and $-\frac{1}{2}I_0R_A(\alpha_1^2 cos2\alpha_0 + \beta_1^2 cos^2\alpha_0)$ is the photoresistance part that is proportional to the DC current, and $-\frac{1}{2}I_1R_A\alpha_1 sin2\alpha_0 \cos(\psi)$ is the photovoltage part that is proportional to the AC current, and depend on the phase difference ψ between the drive and the oscillation.

And similarly, for paramatric resonance where $I_{ac}=I_0+I_1 \cos(2\omega t)$.

$$U_{parametric}(t) = [R_0 + R_A cos^2\theta(t)][I_0 + I_1 \cos(2\omega t)]$$

$$= I_0(R_0 + R_A cos^2\alpha_0) - \frac{1}{2}I_0R_A[\alpha_1^2 cos2\alpha_0 + \beta_1^2 cos^2\alpha_0]$$

$$- \frac{1}{4}I_1R_A[\alpha_1^2 cos2\alpha_0 + \beta_1^2 cos^2\alpha_0]cos2\psi$$

Where $I_0(R_0 + R_A cos^2\alpha_0)$ is the bolometric voltage independent of oscillation amplitude, and $-\frac{1}{2}I_0R_A(\alpha_1^2 cos2\alpha_0 + \beta_1^2 cos^2\alpha_0)$ is the photoresistance part that is proportional to the DC current, and it is exactly the same form as direct excitation, and $-\frac{1}{4}I_1R_A[\alpha_1^2 cos2\alpha_0 + \beta_1^2 cos^2\alpha_0]cos2\psi$ is the photovoltage part that is proportional to the AC current, and depend on the phase difference ψ between the drive and the oscillation.

In the case where $\alpha_0 = 90^o$, $U_{direct}(t)$ and $U_{parametric}(t)$ can be further simplified.

3.2. Electrostatic damage of devices

I want to dedicate something to the mystery of device dying. This is one thing I'm sure everybody that deals with nanodevices have tried to figure out at some point in their measurement. As devices go down in size, they become more and more sensitive to electrostatic discharges (ESD). As a result, nanoscale devices die during the course of measurement, and weeks, and even months of measurement time become useless when they die before complete set of data is taken from one device.

During my years of electrical measurement, I encountered numerous device dying, sometimes more than 10 devices a day! However this mostly happened during the early stage of my experimental career, because I did not form good habits and there are some operation errors which guarantee a device dying that I did not appreciate enough. And after asking around for experience on handling ESD sensitive devices, and summarizing from my own painful experience, I want to try to share my experience on the mystery of device dying.

According to Wikipedia, ESD is the sudden flow of electricity between two electrically charged objects caused by contact, an electrical short or dielectric breakdown. In our case, it is mostly due to contact. There are two types of electric sparks that kills the devices: discharge from human, and discharge from the circuit, which is pretty much always human operation related.

1. In order to minimize discharge from human operators, it is required that human operator ground themselves in the vicinity of and when handling ESD samples. This can be done by wearing an antistatic wrist strap that is connected through a good electrical conductor to the ground connections. The strap is bound with a stainless steel clasp

with a 1 megaohm resistor, which allows high-voltage charges to leak through but prevents a shock hazard when working with low-voltage parts. It will help prevent the buildup of static electricity on the human body and thus protect ESD sensitive devices. Besides the antistatic wrist strap, we also have antistatic garments in the lab that operators of super sensitive samples can try out. They have conductive threads in them, creating a wearable version of a faraday cage and shield ESD sensitive devices from harmful static charges from clothing on the operator. They also have to be connected to ground by a strap in order to work. Also it is recommended not to wear clothing that might produce excessive amount of ESD. These include wool, silk, and synthetic fabrics material clothing and shoes while handling ESD sensitive devices. We also have ESD safe packages which should always be used for storage and transportation of ESD samples and sample holders.

2. Even with the wearing of grounding straps, there would still be some built ups on the operator which might be enough to kill some devices. All the ESDs are created when the human operator is moving: walking around, shaking, the so called “hand in hair syndrome”, and standing up. Plastic and fabric cushioned chairs are known to create a lot of ESDs, despite the fact that they are more comfortable. The best option is a metallic chair that is preferably directly connected to the ground through metal legs. And during the process of standing up when most ESDs are created, it is recommended to firmly hold an exposed metallic part of the chair frame (e.g. a head of a metallic bolt connected to the metallic frame) and do not let go of it until fully standing up. Whenever I walk up to a station with ESD sensitive devices, I would touch conductive metal part that is

connected to the ground, but not to the ESD device, to dissipate ESD on my body during moving. A great candidate is the metallic gas cylinder.

3. Grounding boxes, and the correct procedure of using them. Grounding box is a switch that shorts the sample to ground when not measuring and the design and SOP of grounding boxes can be found in Xiao's thesis. It helps to minimize the possibility of device getting killed. The right procedure to use grounding boxes is to turn on and ground the device when the measurement is not taking place, or when any changes to the electrical circuit is needed. This including touching down and rising of the probe. One important thing I want to point out is that, most device dying are actually related to human errors, and the most common error is grounding the grounding box when current is still applied into the sample. This almost guarantees a device dying, and operators just have to make it a habit to check if the current source is turned off before turning on and off the grounding box.
4. Besides electrostatic discharge from human, device can also die if a high power electronic device is turned on or off in the same electrical power line. This happens because high power changes in the power line will result in a spike of voltage in the line, and a sample being measured electrically will experience this voltage spike. As a result, whenever I measure in room B116, I make sure that everybody else measuring in the same room is aware that my sample is ESD sensitive and they need to inform me before turning on or off any electronic device in the room so that I can ground my device first with the ground box. This is especially important for high power electronics like the pump, high power heater at the cryostation, magnet power supplies and so on, but it is less important for small power electronics like computer screens. However it is always

good to be careful. In the new B120 room, there are 4 power lines, and each measurement station is less affected by other stations in the same room.

5. For measurement with a probe, besides grounding the device with a ground box before rising or touching down the probe, there are some other things that need to be paid attention to. A good stable electrical contact should be made. Imagine a probe that suddenly lifts off from a device and then touches back down onto the device, when voltage is supplied into the probe, there would be extra charge built up at the probe tip when it detaches the sample, and these extra charges will kill the device once the probe retouch the sample. In the real case, it may not be that the probe is taking off from the sample plain, but more likely to have contact from time to time, even when the probe is always touched on the sample, and this serves the same way in charge building up as probes taking off. As a result, it is important to make non-flaky contact, and it would also be a good idea to have the probe station on a stage less affected by vibrations, for example, human activities like walking around, slamming the door. It was found in the past that on weekends when there are less human activities, samples on the probe station do die less often. The best scenario is putting the probe station on a vibration isolated stage.
6. Once I noticed one Tee connector in my electrical circuit was broken, resulting in excessive reflection of voltage back into the sample. The reflected voltage together with the applied voltage adds onto each other and killed many devices. After I replaced the bad Tee with a good one, device dying stopped. When devices are systematically dying, it is important to stop and check if any of the connections are flaky, or if any connectors need to be replaced.

7. Things that we have tried but didn't improve much include a humidifier and an air ionizer. I think the reason is, most device dying are still caused by human errors, or bad connection or vibrations or electrical shock, and humidifier or air ionizer would not help much with that. In the last two years of my measurement, I did not kill a single device, even when I have to transfer helium from external helium source, and I had to turn on and off the heater, the pump a lot. Being careful and form a good habit just goes a long way in measurement of ESD sensitive devices.

3.3. References

1. Sankey, J. C. *et al.* Spin-transfer-driven ferromagnetic resonance of individual nanomagnets. *Phys. Rev. Lett.* **96**, 227601 (2006).
2. Tulapurkar, A. A. et al, Spin-torque diode effect in magnetic tunnel junctions, *Nature*, **438**, 339 (2005)
3. Mecking, N., Gui, Y. S. & Hu, C. M. Microwave photovoltage and photoresistance effects in ferromagnetic microstrips. *Phys. Rev. B* **76**, 224430 (2007).

Chapter 4. Nanowire spin torque oscillator driven by spin orbit torques

Spin torque from spin current applied to a nanoscale region of a ferromagnet can act as negative magnetic damping and thereby excite self-oscillations of its magnetization, as we mentioned in the background. In contrast, spin torque uniformly applied to the magnetization of an extended ferromagnetic film does not generate self-oscillatory magnetic dynamics but leads to reduction of the saturation magnetization. Here we report studies of the effect of spin torque on a system of intermediate dimensionality -- a ferromagnetic nanowire. We observe coherent self-oscillations of magnetization in a ferromagnetic nanowire serving as the active region of a spin torque oscillator driven by spin orbit torques. Our work demonstrates that magnetization self-oscillations can be excited in a one-dimensional magnetic system and that dimensions of the active region of spin torque oscillators can be extended beyond the nanometer length scale.

4.1. Introduction

A current of spin angular momentum incident on a ferromagnet exerts torque on its magnetization and drives it out of equilibrium[1, 2]. Owing to its non-conservative nature, this spin torque (ST) can act as effective negative magnetic damping and thereby excite magnetization self-oscillations[3, 4]. ST oscillators (STO) have been realized in nanoscale spin valves[3, 5, 6, 7], point contacts to magnetic multilayers[8, 9, 10] and nanoscale magnetic tunnel junctions[11, 12, 13, 14, 15]. Recently, a new type of STO based on current-induced spin orbit (SO) torques in a Permalloy(Py)/platinum(Pt) bilayer was demonstrated[16, 17, 18]. Spin orbit torques[19, 20, 21] in this system can arise from the spin Hall effect in Pt[22, 23, 24, 25, 26, 27, 28] and the Rashba effect at the Pt/ Py interface[29, 30, 31, 32].

In all STOs studied to date, the active region where the negative ST damping exceeds the positive Gilbert damping of the ferromagnet was restricted to nanoscale dimensions. A recent study[33] of spatially uniform ST applied to an extended ferromagnetic film revealed that coherent self-oscillations of magnetization cannot be excited in this two-dimensional (2D) magnetic system. Instead, ST was shown to significantly reduce the saturation magnetization of the film[33]. The absence of ST-driven self-oscillations in a 2D ferromagnet was attributed to amplitude-dependent damping arising from nonlinear magnon scattering that prevents any of the multiple interacting spin wave modes of the system from reaching the state of large-amplitude self-oscillations. As a result, the energy and angular momentum pumped by ST into the film is redistributed among a large number of spin wave modes, leading to reduction of the saturation magnetization of the film. This

study raises an important question about the role of the magnetic system dimensionality in ST-induced magnetization dynamics.

In this article, we demonstrate that spatially uniform ST can excite self-oscillations of magnetization in a 1D magnetic system—a ferromagnetic nanowire. We report studies of ST-driven dynamics in a Pt/Py bilayer nanowire, in which SO torques excite self-oscillations of magnetization over a 1.8 μm long active region. This nanowire STO exhibits two types of self-oscillatory modes that arise directly from the edge and bulk spin wave eigenmodes of the Py nanowire[34]. Our work suggests that geometric confinement of the spin wave spectrum in the 1D nanowire geometry limits the phase space for nonlinear magnon scattering compared with the 2D film geometry and thereby enables STOs with a spatially extended active region.

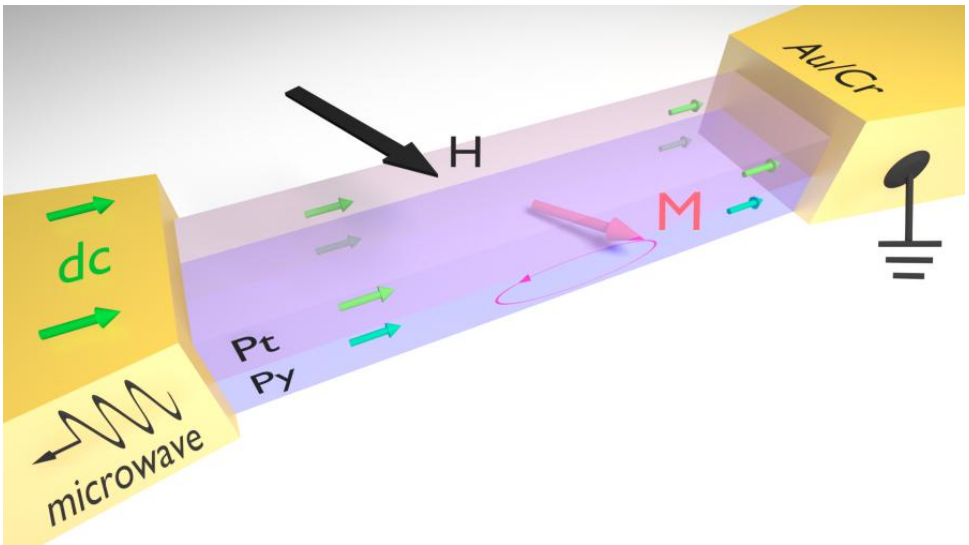

Figure 4.1 Schematic of a Pt/Py nanowire STO device: external magnetic field is shown as a black arrow, precessing Py magnetization is shown as a red arrow, green arrows indicate the flow of direct electric current applied to the nanowire, microwave voltage generated by the sample is depicted as a wave with an arrow.

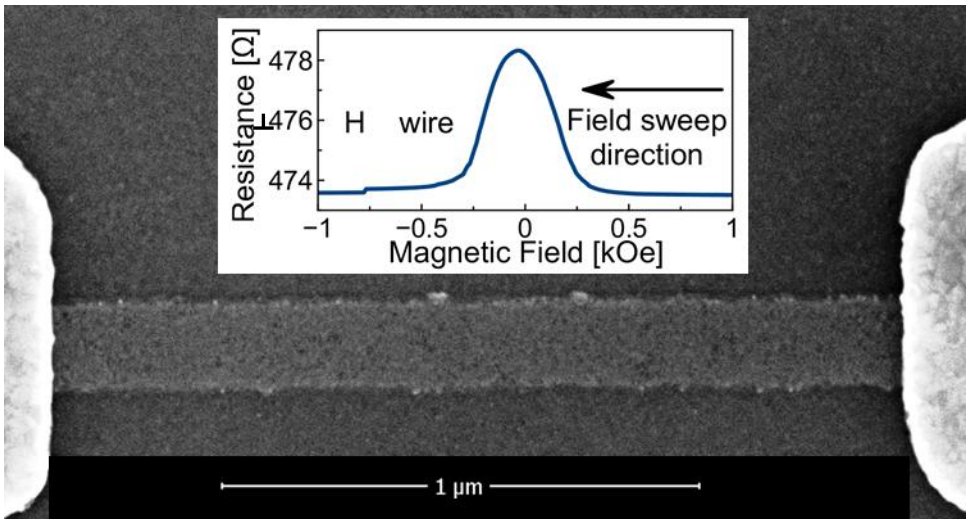

Figure 4.2 Scanning electron micrograph of the Pt/Py nanowire STO. The Pt/Py nanowire is the grey strip in the lower part of the image. The bright areas on both sides of the image are Au/Cr leads. Scale bar, 1 μm. The inset shows resistance versus in-plane magnetic field applied perpendicular to the nanowire measured at the bath temperature T_b=4.2 K and a bias current of 0.5 mA. The black arrow shows the magnetic field sweep direction.

4.2. Results

4.2.1 Sample description

Sample material stack information and nanofabrication are discussed in detail in Chapter 2. Dimension of nanowires are 6 μm long and 190 nm wide, two Au(35 nm)/ Cr(7 nm) leads are attached to each nanowire with a 1.8 μm gap between the leads, which defines the active region of the device as shown in Fig. 4.1. The resistance of the device measured at bath temperature T_b=4.2 K versus magnetic field applied in the sample plane perpendicular to the nanowire is shown in the inset of Fig. 4.2. This plot reveals that the anisotropic magnetoresistance (AMR) of the Pt/Py bilayer is 1%.

4.2.2 Electrical measurements

To study self-oscillatory magnetic dynamics excited by SO torques, we apply a saturating magnetic field (H>0.5 kOe) in the plane of the sample in a direction nearly perpendicular to the nanowire axis. In this configuration, SO torques applied to the Py magnetization act as effective magnetic damping[25]. We apply a direct current bias I_{dc} to the nanowire and measure the microwave signal emitted by the device using a spectrum analyzer [3]. The microwave signal $V_{ac} \sim I_{dc}\delta R_{ac}$ is generated by the AMR resistance oscillations δR_{ac} arising from the magnetization self-oscillations [18]. Microwave signal emission, shown in Fig. 4.3, is only observed above a critical current I_c with the current polarity corresponding to SO torques acting as negative damping [25]. We measured the microwave emission for five nominally identical devices and found similar results for all these samples.

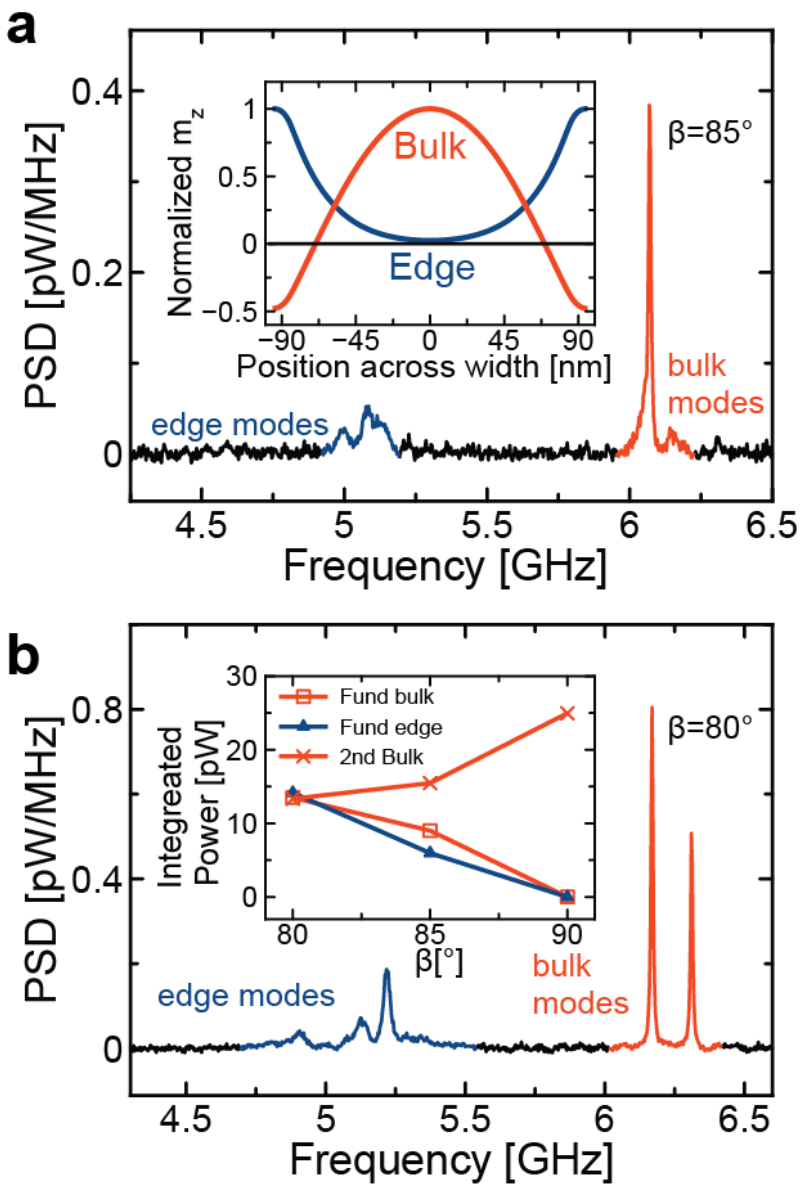

Figure 4.3 Power spectral density (PSD) of the microwave signal emitted by the Pt/Py nanowire at direct current bias I_{dc}=2.45 mA, bath temperature T_b=4.2 K and magnetic field H=890 Oe applied in the plane of the sample at an angle (a) β=85° and (b) β=80° with respect to the nanowire axis. The red, blue and green sections of the PSD curves correspond to the bulk spin wave modes, edge spin wave modes and the baseline, respectively. The inset in a shows the spatial profiles of the edge (blue) and bulk (red) spin wave modes across the nanowire width given by micromagnetic simulations. The inset in b shows angular (β) dependence of the integrated power in the fundamental harmonic of the bulk group of spectral peaks (red squares), the second harmonic of the bulk group of peaks (red crosses) and the fundamental harmonic of the edge group of peaks (blue triangles) measured at I_{dc}=2.4125, mA and H=890 Oe. Lines are guides to the eye.

For all samples, the microwave emission spectra for $I_{dc}>I_c$ exhibit two groups of closely spaced peaks with a frequency gap between the groups of ~1 GHz. Each group consists of one to four distinct emission peaks separated from each other by tens to hundreds of mega Hertz. The high- and low-frequency groups of peaks appear at similar critical currents. Both groups of peaks are observed in the entire range of magnetic fields (H=0.5–1.5 kOe) employed in this study. For the high-frequency group of peaks, microwave emission is observed not only at the fundamental frequency shown in Fig. 4.3, but also at the second harmonic. As illustrated in the inset of Fig. 4.3b, the emitted power at the fundamental frequency is zero for magnetic field applied at an angle$\beta=90°$ with respect to the nanowire axis and increases with decreasing β. In contrast, the emitted power in the second harmonic has a maximum at $\beta=90°$ and decreases with decreasing β. Such angular dependence of the emitted power in the fundamental and second harmonic is expected for a microwave signal arising from AMR. For the low-frequency group of peaks, no emission is seen at the second harmonic, which can be explained by the smaller amplitude of magnetization precession reached by these modes and an equilibrium magnetization direction within the mode excitation area being closer to the nanowire axis. Figure 4.4 illustrates the dependence of the emission spectra on I_{dc} for H=890 Oe and $\beta=85°$.

To determine the origin of the microwave emission signals, we make measurements of the spectrum of spin wave eigenmodes of the nanowire using ST ferromagnetic resonance (ST-FMR)[35, 36, 37]. In this technique, a microwave current I_{ac} applied to the nanowire excites magnetization dynamics in Py by the combined action of current-induced SO torques and the Oersted field from the current in Pt, and thereby generates AMR resistance oscillations

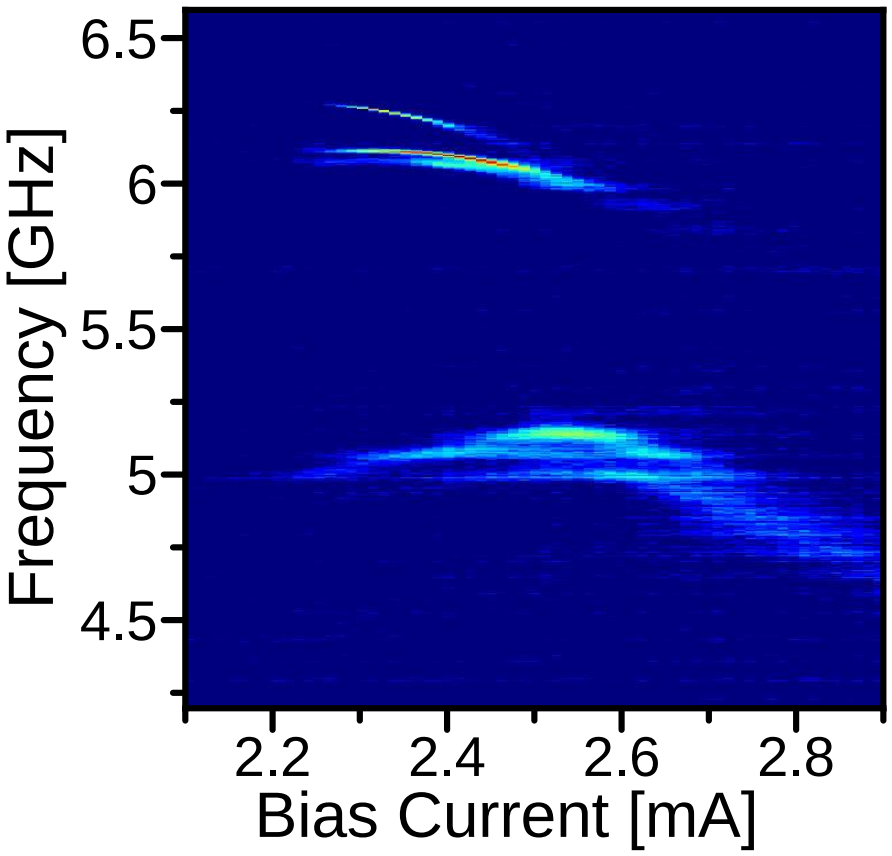

Figure 4.4 Dependence of the emission spectrum on I_{dc} for H=890 Oe and β=85°.

at the frequency of the microwave drive[37]. Mixing of the current and resistance oscillations as well as variation of the time-averaged sample resistance in response to the microwave drive[38, 39] give rise to a direct voltage V_{dc} that is measured as a function of magnetic field H applied to the sample. Peaks in $V_{dc}(H)$ arise from resonant excitation of spin wave eigenmodes of the nanowire. An ST-FMR spectrum of spin wave eigenmodes measured at $\beta=85°$, drive frequency of 6 GHz and $I_{dc}=2.0$ mA$<I_c$ is shown in Fig. 4.5.

Similar to the microwave emission spectra, we observe two groups of modes in the ST-FMR spectra. In Fig. 4.6, we compare the field dependence of the eigenmode frequencies measured by ST-FMR at $I_{dc}<I_c$ to the frequencies of self-oscillatory modes measured at I_c. This figure demonstrates that the frequencies of all self-oscillatory modes at I_c coincide with the frequencies of spin wave eigenmodes of the system measured by ST-FMR. Therefore, all self-oscillatory modes of the system arise directly from spin wave eigenmodes of the nanowire. This type of eigenmode self-oscillation is qualitatively different from the spin wave bullet mode excited by SO torques in a planar point contact to an extended ferromagnetic film [16]. The bullet mode is a nonlinear type of oscillation, self-localized to a region with dimensions below 100 nm and with frequency below the spectrum of spin wave eigenmodes of the film[40].

It is well-known that spin wave eigenmodes of a transversely magnetized thin-film ferromagnetic nanowire can be classified as bulk and edge eigenmodes[34, 41, 42, 43] These eigenmodes have spatially inhomogeneous profiles along the wire width with reduced (enhanced) amplitude near the wire edges for the bulk (edge) eigenmodes. The frequencies of the edge spin wave modes lie below those of the bulk modes due to reduced

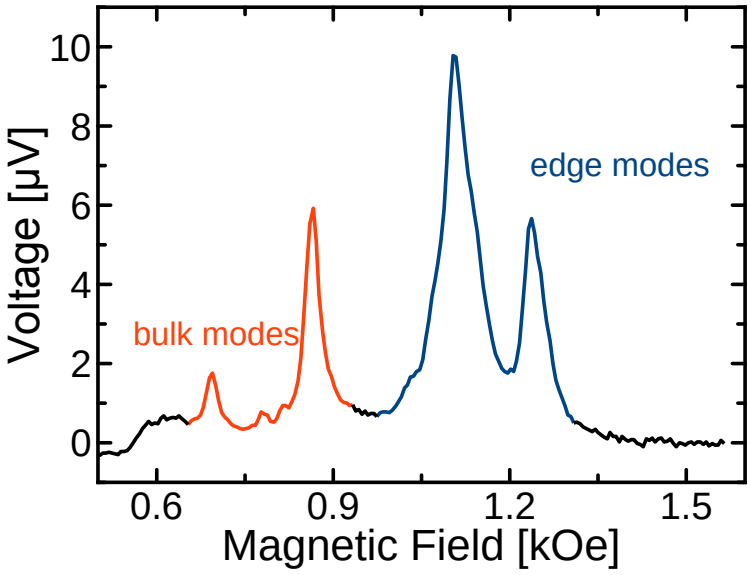

Figure 4.5 ST-FMR spectrum of the nanowire device measured at the microwave drive frequency of 6 GHz, β=85° and I_{dc}=2.0 mA<I_c. The red, blue and green sections of the curve represent the bulk modes, edge modes and the baseline, respectively.

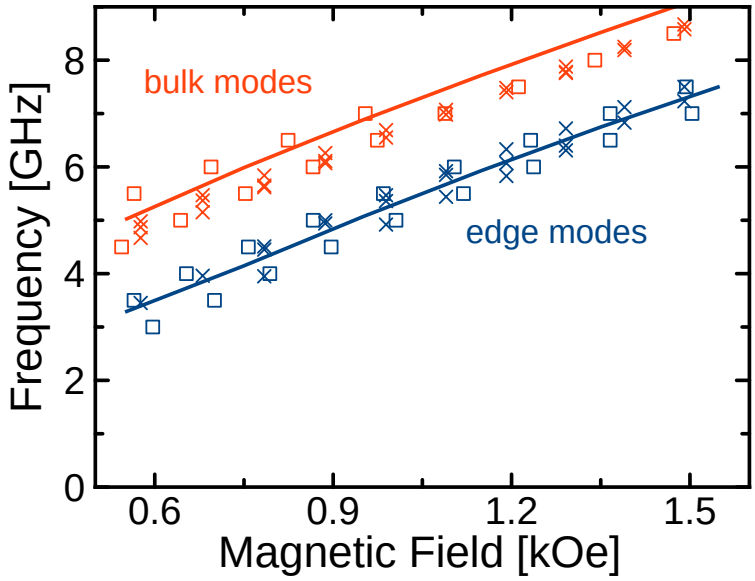

Figure 4.6 Frequency versus magnetic field applied at β=85°: (squares) spin wave eigenmodes measured by ST-FMR, (crosses) self-oscillatory modes at I_c, and (lines) bulk and edge spin wave eigenmodes given by micromagnetic simulations for an ideal nanowire. Colour scheme: red and blue represent bulk and edge spin wave modes, respectively.

internal magnetic field near the wire edges[41]. The frequencies of all eigenmodes are sensitive to the values of magnetic parameters of the Py film, which are different from their bulk values due to the influence of proximate nonmagnetic layers. In addition, the frequencies of the edge modes depend on the edge roughness and spatial variation of the film magnetic properties (magnetic dilution) at the nanowire edges induced by etching[43].

Assuming translational invariance along the nanowire axis, we perform micromagnetic simulations to find the spectrum of spin wave eigenmodes for magnetic field applied in the sample plane at β=85°.

We find that the two lowest frequency spin wave modes are the edge and bulk modes, whose spatial profiles (defined as normalized out-of-plane amplitude of dynamic magnetization m_z) across the wire width are shown in the inset of Fig. 4.3a. The frequencies of these two modes versus in-plane magnetic field are shown in Fig. 4.6.

It is clear from Fig. 4.6 that the frequencies of the calculated edge (bulk) modes are similar to the low (high) frequency groups of eigenmodes measured by ST-FMR and observed in STO measurements. We thus conclude that the high (low) frequency groups of experimentally observed eigenmodes are closely related to the bulk (edge) eigenmodes of an ideal nanowire with translational invariance along the nanowire axis. As demonstrated by our micro-focus Brillouin light scattering (BLS) measurements described below, the fine splitting within a group originates from the spin wave spectrum quantization along the nanowire length. Such quantization can be imposed by reflection of spin waves at the edge of the Au/Cr leads, where the effective magnetic damping rapidly varies as a function of

position along the wire. Figure 4.7 shows the dependence of the integrated microwave power emitted by the STO device on direct bias current I_{dc} for the three spectral peaks comprising the bulk group. The sum of the integrated powers in the three peaks versus I_{dc} is shown as well. Although the power in each individual peak exhibits irregularities as a function of I_{dc}, the sum of integrated powers of the entire group of bulk peaks is a smooth function of I_{dc}. The same trend is found for the edge group of peaks. As discussed in the Methods section, the maximum integrated power emitted by the bulk mode corresponds to the sample resistance oscillations that are 15% of the full AMR amplitude. Similar maximum amplitude of resistance oscillations is found for the edge

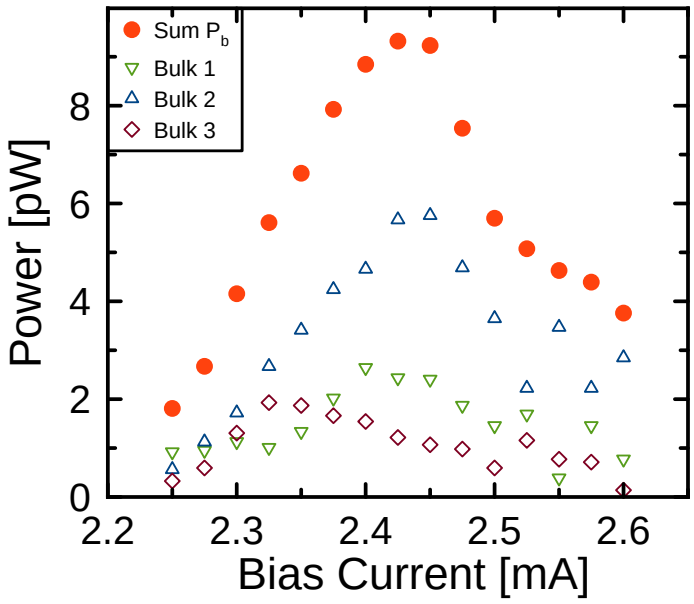

Figure 4.7 Bias current dependence of the integrated emitted power in three individual peaks of the bulk group of self-oscillatory modes as well as the sum of integrated powers of all bulk modes P_b.

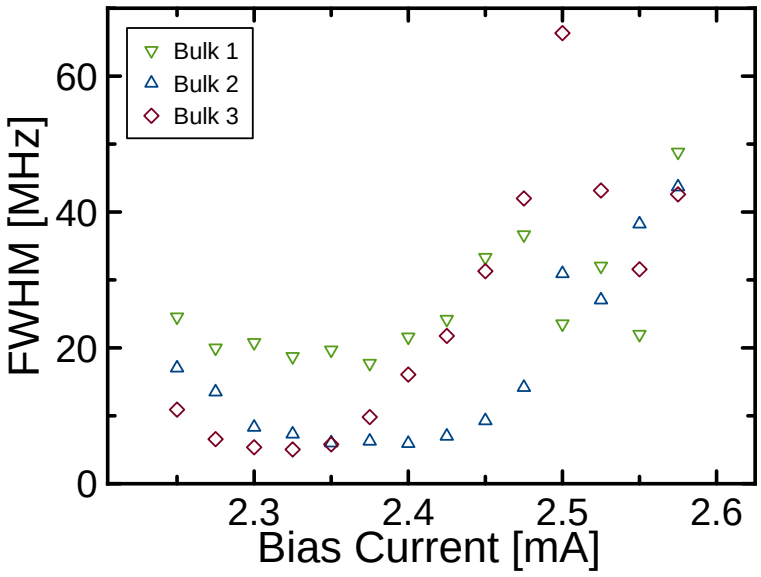

Figure 4.8 Bias current dependence of the spectral linewidths (FWHM) of the individual peaks in the bulk group. Symbols in c and d: (green triangles) bulk mode 1, (blue triangles) bulk mode 2, (purple diamonds) bulk mode 3 and (red circles) the total power of three bulk modes.

mode. This demonstrates that large-amplitude magnetization oscillations can be excited by SO torques in both the bulk and the edge modes of the nanowire. Figure 4.8 shows the full width at half maximum (FWHM) of three spectral peaks of the bulk group versus the bias current. The minimum FWHM for each of the peaks is observed near the current value corresponding to the maximum integrated power of the peak, which is typical for STO dynamics [4].

We also make measurements of the microwave signal emission as a function of temperature. Figure 4.9a,b shows the dependence of the total integrated power in the bulk and edge groups of peaks measured at several values of the bath temperature T_b. The integrated power decreases with increasing T_b and vanishes at $T_b \approx 250$ K. The actual temperature of the nanowire is significantly higher than T_b due to Ohmic heating. The nanowire temperature can be estimated from measurements of the nanowire resistance as

functions of T_b and I_{dc}[18]. As described in the Methods section, the actual nanowire temperature at I_c and T_b=4.2 K is ~150 K. Figure 4.9c illustrates the temperature dependence of the nanowire STO spectral linewidth. This figure shows FWHM of the dominant (highest integrated power) bulk and edge peaks versus temperature. For each peak, the FWHM is measured at the current bias that maximizes the integrated power of the peak. The spectral linewidth of the edge peak decreases with increasing temperature, which cannot be explained by a single-mode STO theory[4]. However, such temperature dependence has been previously observed for multi-mode STOs and was successfully explained by an STO theory taking into account coupling between multiple self-oscillatory modes[48]. The linewidth of the dominant bulk peak is an order of magnitude smaller than that of the dominant edge peak for $T_b \leq 100$ K but it rises precipitously to a value similar to that of the edge peak for $T_b > 100$ K, which might result from enhanced coupling between the bulk and the edge modes for $T_b > 100$ K.

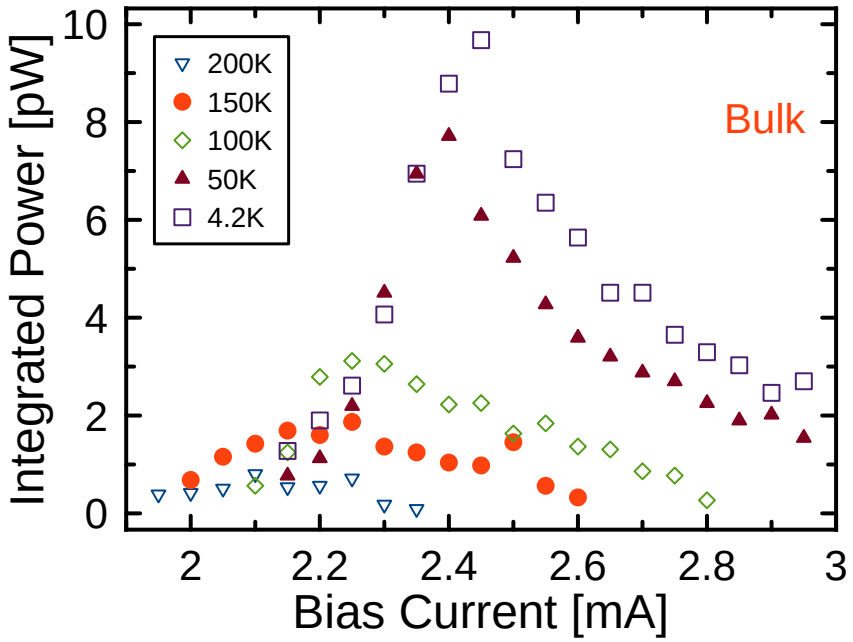

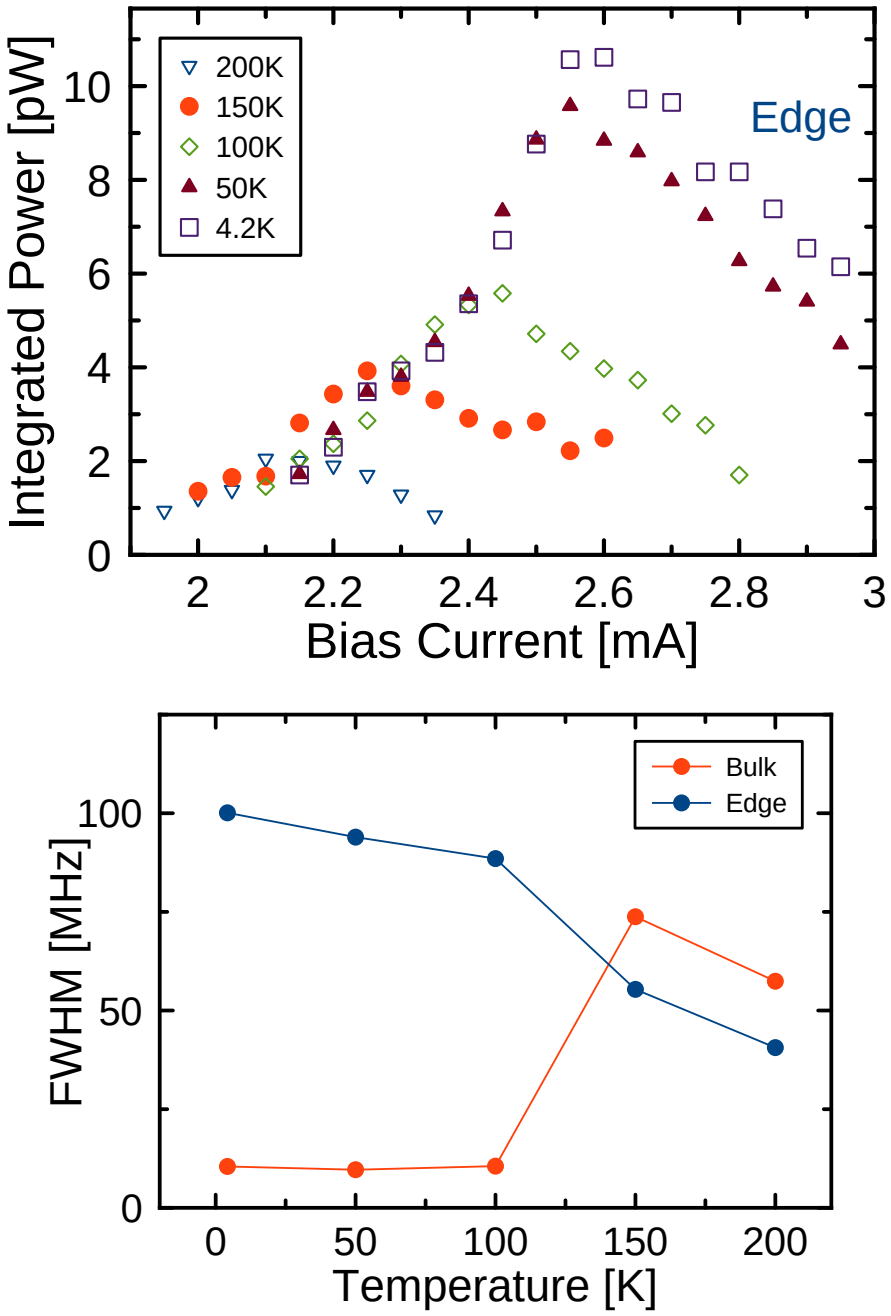

Figure 4.9 Bias current dependence of the integrated microwave power emitted by the bulk (a) and edge (b) spin wave modes measured at β=85°, H=890 Oe and several values of the bath temperature Tb=200 K (blue triangles), 150 K (red dots), 100 K (green diamonds), 50 K (yellow triangles) and 4.2 K (purple squares). (c) Temperature dependence of the spectral linewidth (FWHM) of the highest power bulk (red circles) and edge (blue squares) self-oscillatory modes measured at the bias current of the maximum integrated power of the mode.

4.2.3. BLS measurements

To better understand the nature of the self-oscillatory dynamics induced by SO torques in the Pt/Py nanowire system and to directly confirm that the self-oscillatory modes occupy the entire active region of the nanowire, BLS measurements[49] of the current-driven magnetization dynamics in this system is made by our collaborators Vladislav E. Demidov and Sergej O. Demokritov at University of Münster. Since a 5 nm thick layer of Pt is not sufficiently transparent for BLS studies, we make a separate batch of samples for BLS measurements with the reverse order of deposition of the AlO_x, Py and Pt layers. These AlO_x(2 nm)/Py(5 nm)/Pt(7 nm)/(sapphire substrate) nanowire samples are prepared by e-beam lithography and lift-off technique as described in the Methods section. The microwave signal emission from these samples is similar to that of the samples in Fig 4.1 to Fig 4.9, with two notable differences: the amplitude of self-oscillations of the edge mode is significantly higher than that of the bulk mode and the microwave emission from the edge mode persist up to T_b=300 K. These differences are likely to originate from the different sample fabrication procedure: the lift-off fabrication process creates less nanowire edge damage than the Ar plasma etching process.

The main results of the BLS measurements are presented in Fig. 4.10. Figure 3.10a shows a representative BLS spectrum measured by placing the probing laser spot at the centre of the nanowire. In agreement with the results of electronic measurements of samples with Pt on top, the BLS spectrum exhibits a series of auto-oscillation peaks with the typical frequency separation of hundreds of mega Hertz, which belong to the group of edge modes. By using the high-spatial resolution of the BLS measurements, we identify the

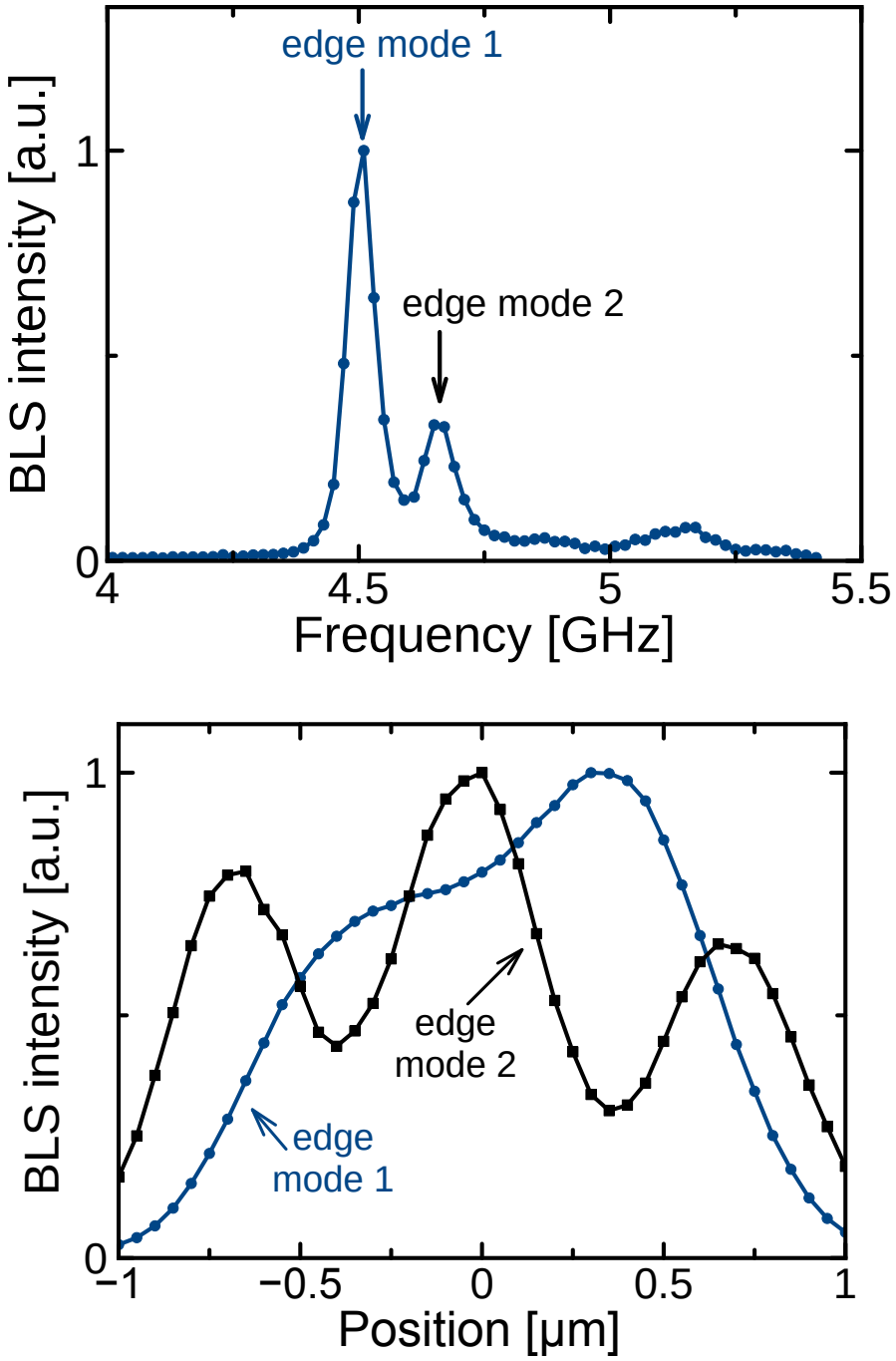

Figure 4.10 (a) BLS spectrum acquired by placing the probing laser spot at the centre of the nanowire. BLS intensity is proportional to the intensity of the dynamic magnetization. The blue, red and green sections of the curve represent the edge mode 1, edge mode 2 and the baseline, respectively. (b) Spatial profiles of the intensity of the dynamic magnetization in the section parallel to the nanowire axis: (blue circles) edge mode 1 and (red squares) edge mode 2. The data were obtained at H=550 Oe and the bias current I_{dc}=2.4 mA.

individual auto-oscillation peaks within the group. For this we fix the BLS detection frequency at the frequency of one of the peaks and record spatial profiles of the dynamic magnetization by moving the probing laser spot along the nanowire axis with the spatial step size of 50 nm. As seen in Fig. 4.10b, the spatial profiles corresponding to the two peaks are fundamentally different. While the profile for the first edge mode exhibits a slightly distorted bell-like shape, the profile for the second peak possesses three maxima. Based on the obtained data we conclude that the individual auto-oscillation peaks within the groups correspond to the standing-wave modes quantized in the direction parallel to the nanowire axis [50]. The first peak corresponds to the combination of the fundamental mode having no nodes and the antisymmetric mode possessing one nodal line at the centre. These two modes are indistinguishable in the BLS spectrum, likely due to their small frequency separation. The second peak apparently corresponds to the mode possessing two nodal lines at the positions of the minima of the measured profile. We note that, since the BLS technique is sensitive to the intensity of the dynamic magnetization, the measured profile does not show a change of the sign across the positions of the nodal lines.

4.3. Discussion

Recent experiments[33] demonstrated that application of spatially uniform SO torques to an extended ferromagnetic film does not result in excitation of magnetic self-oscillations because the amplitudes of all spin wave modes of the film are limited by nonlinear magnon scattering processes. Therefore, our observation of self-oscillatory dynamics excited by SO torques in the entire 1.8 μm long active region of a ferromagnetic

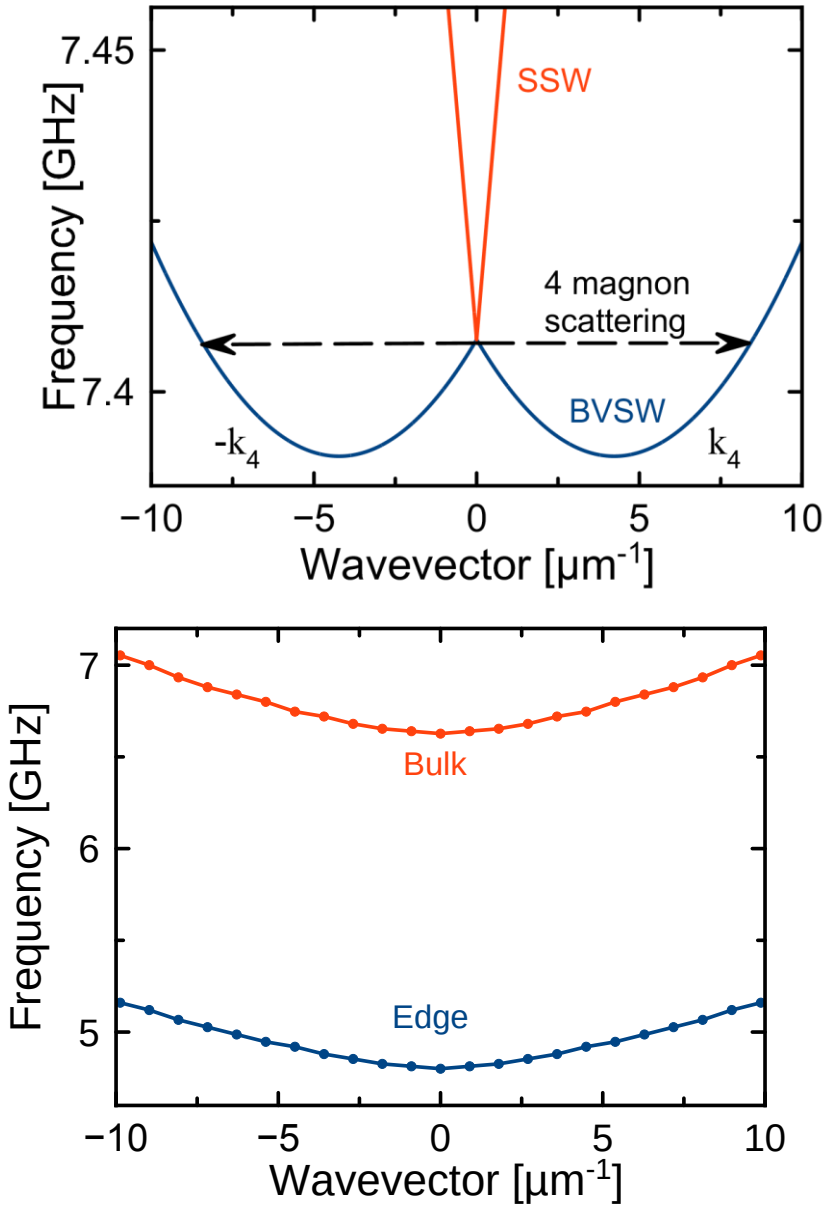

Figure 4.11 (a) Spin wave dispersion relation for BVSW (red) and SSW (blue) modes of a 5-nm thick Py film at H=890 Oe (ref. 51). Arrows indicate energy- and momentum-conserving four-magnon scattering of two uniform mode magnons into two BVSW magnons with wave vectors k_4 and $-k_4$. (b) Spin wave dispersion relation of the 190 nm wide nanowire numerically calculated for β=85° and H=890 Oe. The red squares and blue circles indicate the bulk and edge modes, respectively. Lines are guides to the eye. Energy- and momentum-conserving four-magnon scattering is not allowed within both the bulk and the edge mode branches of the nanowire spin wave dispersion.

nanowire is surprising. We argue that quantization of the spin wave spectrum in the nanowire geometry reduces the number of available nonlinear magnon scattering channels and thereby enables excitation of self-oscillatory dynamics of the low-energy spin wave eigenmodes of the nanowire.

Figure 4.11a shows the spin wave dispersion relation of a 5-nm thick extended Py film calculated for spin wave propagating parallel (backward volume spin waves (BVSW)) and perpendicular (surface spin waves (SSW)) to the in-plane magnetization vector [51]. Energy- and momentum-conserving four-magnon scattering processes from the uniform (k=0) mode into spin wave modes with a finite wave vector k_4 are allowed for the BVSW but not for the SSW modes as schematically illustrated in Fig. 4.11a. This nonlinear scattering channel is always present in the 2D film geometry and it contributes to the nonlinear damping of the uniform mode. When such a film is patterned into a nanowire aligned perpendicular to the magnetization direction, the BVSW mode spectrum becomes quantized and the energy-conserving four-magnon scattering channel becomes suppressed for wires narrower than $\sim \pi k_4^{-1}$, which is ≈0.5 μm for our 5-nm thick Py nanowires. Figure 4.11b shows the spin wave dispersion relation numerically calculated for our 190-nm wide nanowire sample. The frequencies of the bulk and edge modes are shifted below the frequencies of spin waves in the extended film shown in Fig. 4.11a by the demagnetizing field of the nanowire. The dispersion branches of both the edge and the bulk spin wave modes do not have minima at $k \neq 0$ and therefore do not support the energy- and momentum-conserving four-magnon scattering within each of the branches.

Since some nonlinear magnon scattering processes (such as the four-magnon process) responsible for limiting the amplitude of low-frequency spin wave modes in the 2D film are eliminated in the nanowire, ST excitation of large-amplitude self-oscillatory spin wave modes may become possible above the critical current. At higher currents, SO torques increase the occupation numbers for all magnon modes, which results in enhanced scattering in the remaining nonlinear channels and the associated decrease of the amplitude of self-oscillations seen in Fig. 4.7, as well as in the reduction of the saturation magnetization and the associated decrease of the self-oscillatory mode frequency with current seen in Fig. 4.4. Our data in Fig. 4.9 showing decreasing self-oscillation amplitude with increasing temperature suggest that enhanced population of thermal magnons and magnon–phonon scattering might also play a role in suppression of the self-oscillatory dynamics. Development of a detailed theory accounting for all magnon scattering channels in the nanowire in the presence of SO torques is required for quantitative explanation of our experimental data, and we hope that our work will stimulate the development of such a theory.

In conclusion, we demonstrated that spatially uniform STs can excite self-oscillations of magnetization in a 1D ferromagnetic system—a Py nanowire. The self-oscillatory modes induced by ST in this system directly arise from the bulk and edge spin wave eigenmodes of the nanowire. The 1D nanowire geometry offers unique advantages for studies of magnetization dynamics driven by STs over the 2D extended thin-film system, in which spatially uniform ST does not excite magnetization self-oscillations. Our results suggest that the self-oscillatory dynamics in the nanowire geometry is enabled by geometric

confinement of magnons that suppresses nonlinear magnon scattering. Our work demonstrates the feasibility of STOs with the active region dimensions extended beyond the nanometre length scale.

4.4 Methods

4.4.1. BLS measurements

Micro-focus BLS measurements were performed at room temperature by focusing light produced by a continuous-wave single-frequency laser operating at a wavelength of 532 nm into a diffraction-limited spot. The light scattered from magnetic oscillations was analyzed by a six-pass Fabry–Perot interferometer TFP-1 (JRS Scientific Instruments, Switzerland) to obtain information about the BLS intensity proportional to the square of the amplitude of the dynamic magnetization at the location of the probing spot.

4.4.2. Estimate of the amplitude of resistance self-oscillations

In this section, we estimate the maximum amplitude of the resistance oscillations achieved by the bulk and edge modes in the self-oscillatory regime. The measured integrated power at the fundamental frequency emitted by the bulk group of modes P_b (corrected for frequency-dependent attenuation and amplification in the measurement circuit) is plotted as a function of direct bias current Idc in Fig. 4.7. This power is directly related to the amplitude of the nanowire resistance oscillations δR_{ac} at the fundamental frequency of magnetization self-oscillations. These resistance oscillations arise from AMR of the nanowire. The microwave voltage generated by the nanowire STO

device at the fundamental frequency of the bulk mode $I_{dc}\delta R_{ac}$ is detected by a 50 Ω microwave spectrum analyzer as microwave power P_b (ref. 3):

$$P_b = \frac{1}{2R_{50}}(I_{dc}\delta R_{ac}\frac{R_{50}}{R+R_{50}})^2 \qquad (1)$$

where $R_{50} \equiv 50\ \Omega$ is the spectrum analyzer impedance and R is the nanowire resistance. From this equation, we can express the amplitude of resistance oscillations at the fundamental frequency as a function of the emitted power:

$$\delta R_{ac} = \frac{R+R_{50}}{I_{dc}\sqrt{R_{50}}}\sqrt{2P_b} \qquad (2)$$

Using equation (2) and the maximum experimentally measured integrated power in the bulk group of modes P_b=10 pW at I_{dc}=2.45 mA as shown in Fig. 4.9a, we evaluate $\delta R_{ac} \approx 0.15\ \Omega$. A similar maximum value of δR_{ac} arising from the edge mode self-oscillations is calculated from the data in Fig. 4.9b. These values of δR_{ac} are substantial fractions of the full AMR amplitude of 1 Ω shown in the inset in Fig. 4.2b. This demonstrates that large amplitude of magnetization self-oscillations can be achieved by both the bulk and the edge modes of the nanowire STO.

4.4.3. Sample temperature

Direct current bias I_{dc} can significantly increase the temperature of the nanowire due to Ohmic heating. To estimate the actual temperature of the nanowire at large I_{dc}, we compare measurements of the wire resistance as a function of temperature at small I_{dc}=0.1 mA to measurements of the wire resistance versus I_{dc} taken at the bath temperature T_b=4.2 K (ref. 18). These data shows that resistance of the nanowire is

approximately quadratic in both T_b and I_{dc}. This allows us to estimate the actual temperature of the nanowire directly. For example, at I_{dc}=2.0 mA, the actual temperature of the nanowire T≈150 K.

4.5. References

1. Slonczewski, J. C. Current-driven excitation of magnetic multilayers. *J. Magn. Magn. Mater.***159**, L1–L7 (1996).
2. Berger, L. Emission of spin waves by a magnetic multilayer traversed by a current. *Phys. Rev. B* **54**, 9353–9358 (1996).
3. Kiselev, S. I. *et al.* Microwave oscillations of a nanomagnet driven by a spin-polarized current. *Nature* **425**, 380–383 (2003).
4. Slavin, A. N. & Tiberkevich, V. Nonlinear auto-oscillator theory of microwave generation by spin-polarized current. *IEEE Trans. Magn.* **45**, 1875–1918 (2009).
5. Ozyilmaz, B., Kent, A. D., Sun, J. Z., Rooks, M. J. & Koch, R. H. Current-induced excitations in single cobalt ferromagnetic layer nanopillars. *Phys. Rev. Lett.* **93**, 176604 (2004).
6. Mistral, Q. *et al.* Current-driven microwave oscillations in current perpendicular-to-plane spin-valve nanopillars. *Appl. Phys. Lett.* **88**, 192507 (2006).
7. Braganca, P. M. *et al.* Nanoscale magnetic field detection using a spin torque oscillator.*Nanotechnology* **21**, 235202 (2010).
8. Rippard, W. H., Pufall, M. R., Kaka, S., Russek, S. E. & Silva, T. J. Direct-current induced dynamics in point $Co_{90}Fe_{10}/Ni_{80}Fe_{20}$ contacts. *Phys. Rev. Lett.* **92**, 027201 (2004).
9. Ruotolo, A. *et al.* Coherent dynamics of a magnetic vortex-antivortex lattice. *Nat. Nanotech.***4**, 528–532 (2009).
10. Mohseni, S. M. *et al.* Spin torque generated magnetic droplet solitons. *Science* **339**,1295–1298 (2013).
11. Nazarov, A. V. *et al.* Spin transfer stimulated microwave emission in MgO magnetic tunnel junctions. *Appl. Phys. Lett.* **88**, 162504 (2006).

12. Deac, A. M. *et al.* Bias-driven high-power microwave emission from MgO-based tunnel magnetoresistance devices. *Nat. Phys.* **4**, 803–809 (2008).

13. Houssameddine, D. *et al.* Spin transfer induced coherent microwave emission with large power from nanoscale MgO tunnel junctions. *Appl. Phys. Lett.* **93**, 022505 (2008).

14. Georges, B. *et al.* Origin of the spectral linewidth in nonlinear spin-transfer oscillators based on MgO tunnel junctions. *Phys. Rev. B* **80**, 060404 (2009).

15. Rowlands, G. E., Katine, J. A., Langer, J., Zhu, J. & Krivorotov, I. N. Time domain mapping of spin torque oscillator effective energy. *Phys. Rev. Lett.* **111**, 087206 (2013).

16. Demidov, V. E. *et al.* Magnetic nano-oscillator driven by pure spin current. *Nat. Mater.* **11**,1028–1031 (2012).

17. Liu, L., Pai, C.-F., Ralph, D. C. & Buhrman, R. A. Magnetic oscillations driven by the spin Hall effect in 3-Terminal magnetic tunnel junction devices. *Phys. Rev. Lett.* **109**, 186602(2012).

18. Liu, R. H., Lim, W. L. & Urazhdin, S. Spectral characteristics of the microwave emission by the spin Hall nano-oscillator. *Phys. Rev. Lett.* **110**, 147601 (2013).

19. Haney, P. M., Lee, H.-W., Lee, K.-J., Manchon, A. & Stiles, M. D. Current induced torques and interfacial spin-orbit coupling: semiclassical modeling. *Phys. Rev. B* **87**, 174411 (2013).

20. Kim, J. *et al.* Layer thickness dependence of the current-induced effective field vector in Ta|CoFeB|MgO. *Nat. Mater.* **12**, 240–245 (2012).

21. Martinez, E., Emori, S. & Beach, G. S. D. Current-driven domain wall motion along high perpendicular anisotropy multilayers: the role of the Rashba field, the spin Hall effect, and the Dzyaloshinskii-Moriya interaction. *Appl. Phys. Lett.* **103**, 072406 (2013).

22. Dyakonov, M. I. & Perel, V. I. Possibility of orienting electron spins with current. *JETP Lett.***13**, 467 (1971).

23. Hirsch, J. E. Spin Hall effect. *Phys. Rev. Lett.* **83**, 1834–1837 (1999).

24. Zhang, S. Spin Hall effect in the presence of spin diffusion. *Phys. Rev. Lett.* **85**, 393–396(2000).

25. Ando, K. *et al.* Electric manipulation of spin relaxation using the spin Hall effect. *Phys. Rev. Lett.* **101**, 036601 (2008).

26. Fan, X. *et al.* Observation of the nonlocal spin-orbital effective field. *Nat. Commun.* **4**, 1799(2013).

27. Hoffmann, A. Spin Hall effects in metals. *IEEE Trans. Magn.* **49**, 5172–5193 (2013).

28. Bai, L. *et al.* Universal method for separating spin pumping from spin rectification voltage of ferromagnetic resonance. *Phys. Rev. Lett.* **111**, 217602 (2013).

29. Bychkov, Y. u. A. & Rashba, E. I. Properties of a 2D electron gas with lifted spectral degeneracy. *JETP Lett.* **39**, 78–81 (1984).

30. Sinova, J. *et al.* Universal intrinsic spin Hall effect. *Phys. Rev. Lett.* **92**, 126603 (2004).

31. Obata, K. & Tatara, G. Current-induced domain wall motion in Rashba spin-orbit system.*Phys. Rev. B* **77**, 214429 (2008).

32. Miron, I. M. *et al.* Current-driven spin torque induced by the Rashba effect in a ferromagnetic metal layer. *Nat. Mater.* **9**, 230–234 (2010).

33. Demidov, V. E. *et al.* Control of magnetic fluctuations by spin current. *Phys. Rev. Lett.* **107**,107204 (2011).

34. Duan, Z. *et al.* Spin-wave modes in permalloy/platinum wires and tuning of the mode damping by spin Hall current. *Phys. Rev. B* **90**, 024427 (2014).

35. Tulapurkar, A. A. *et al.* Spin-torque diode effect in magnetic tunnel junctions. *Nature* **438**,339–342 (2005).

36. Sankey, J. C. *et al.* Spin-transfer-driven ferromagnetic resonance of individual nanomagnets.*Phys. Rev. Lett.* **96**, 227601 (2006).

37. Liu, L., Moriyama, T., Ralph, D. C. & Buhrman, R. A. Spin-torque ferromagnetic resonance induced by the spin Hall effect. *Phys. Rev. Lett.* **106**, 036601 (2011).

38. Wang, C. *et al.* Bias and angular dependence of spin-transfer torque in magnetic tunnel junctions. *Phys. Rev. B* **79**, 224416 (2009).

39. Mecking, N., Gui, Y. S. & Hu, C. M. Microwave photovoltage and photoresistance effects in ferromagnetic microstrips. *Phys. Rev. B* **76**, 224430 (2007).

40. Slavin, A. & Tiberkevich, V. Spin wave mode excited by spin-polarized current in a magnetic nanocontact is a standing self-localized wave bullet. *Phys. Rev. Lett.* **95**, 237201 (2005).

41. Bayer, C. *et al.* Spin-wave excitations in finite rectangular elements. *Top. Appl. Phys.* **101**,57–103 (2006).

42. Park, J. P., Eames, P., Engebretson, D. M., Berezovsky, J. & Crowell, P. A. Spatially resolved dynamics of localized spin-wave modes in ferromagnetic wires. *Phys. Rev. Lett.* **89**,277201 (2002).

43. McMichael, R. D. & Maranville, B. B. Edge saturation fields and dynamic edge modes in ideal and nonideal magnetic film edges. *Phys. Rev. B* **74**, 024424 (2006).

44. Donahue, M. J. & Porter, D. G. OOMMF User's Guide, Version 1.0, Report No. NISTIR 6376 (National Institute of Standards and Technology, 1999).

45. Krivorotov, I. N. *et al.* Temperature dependence of spin-transfer-induced switching of nanomagnets. *Phys. Rev. Lett.* **93**, 166603 (2004).

46. Rantschler, J. O. *et al.* Surface anisotropy of permalloy in NM/NiFe/NM multilayers. *J. Appl. Phys.* **97**, 10J113 (2005).

47. Nembach, H. T., Shaw, J. M., Boone, C. T. & Silva, T. J. Mode- and size-dependent Landau-Lifshitz damping in magnetic nanostructures: evidence for nonlocal damping. *Phys. Rev. Lett.* **110**, 117201 (2013).

48. Muduli, P. K., Heinonen, O. G. & Akerman, J. Temperature dependence of linewidth in nanocontact based spin torque oscillators: effect of multiple oscillatory modes. *Phys. Rev. B***86**, 174408 (2012).

49. Demokritov, S. O. & Demidov, V. E. Micro-Brillouin light scattering spectroscopy of magnetic nanostructures. *IEEE Trans. Magn.* **44**, 6–12 (2008).

50. Ulrichs, H., Demidov, V. E., Demokritov, S. O. & Urazhdin, S. Parametric excitation of eigenmodes in microscopic magnetic dots. *Phys. Rev. B* **84**, 094401 (2011).

51. De Wames, R. E. & Wolfram, T. Dipole-exchange spin waves in ferromagnetic films. *J. Appl. Phys.* **41**, 987–993 (1970).

Chapter 5. Reduction of phase noise in nanowire spin orbit torque oscillators

Spin torque oscillators (STOs) are compact, tunable sources of microwave radiation that serve as a test bed for studies of nonlinear magnetization dynamics at the nanometer length scale. In particular, the spin torque in an STO can be created by spin-orbit interaction, as we have demonstrated in Chapter 3, but low spectral purity of the microwave signals generated by spin orbit torque oscillators hinders practical applications of these magnetic nanodevices. Here we demonstrate a method for decreasing the phase noise of spin orbit torque oscillators based on Pt/$Ni_{80}Fe_{20}$ nanowires. We experimentally demonstrate that tapering of the nanowire, which serves as the STO active region, significantly decreases the spectral linewidth of the generated signal. We explain the observed linewidth narrowing in the framework of the Ginzburg-Landau auto-oscillator model. The model reveals that spatial non-uniformity of the spin current density in the tapered nanowire geometry hinders the excitation of higher order spin-wave modes, thus stabilizing the single-mode generation regime. This non-uniformity also generates a restoring force acting on the excited self-oscillatory mode, which reduces thermal fluctuations of the mode spatial position along the wire. Both these effects improve the STO spectral purity.

5.1. Introduction

The discovery of giant spin Hall effect in nonmagnetic heavy metals such as Pt[1-3], W[4] and Ta[3,5,6,11] creates new opportunities for the manipulation of magnetization by spin currents, including switching and excitation of self-oscillations of magnetization[4-10]. Spin-orbit interaction in such heavy metals results in large spin-dependent deflection of electrons participating in electric charge current[13-17], which can be viewed as a pure spin current flowing perpendicular to the charge current[18-20]. This pure spin current can be injected from the heavy metal into an adjacent ferromagnet and apply spin torque to its magnetization[21,22]. Due to its non-conservative nature, this spin orbit torque can act as magnetic anti-damping[23,24] leading to the decrease of the relaxation rates of spin waves (SWs), which was observed in both metallic[2,12,25,26] and insulating[3,27] ferromagnets.

A spin orbit torque uniformly applied to a spatially extended ferromagnetic film cannot reduce the spin wave damping to zero, and therefore, cannot excite self-oscillations of magnetization in the film even at high spin current densities [28]. The origin of this anti-damping saturation is the non-linear spin wave interactions, which distribute the injected energy and angular momentum among a continuum of SWs with different wave vectors, so that the net damping rate for any SW mode remains positive[7]. Patterning of the ferromagnetic film into nanoscale dots discretizes the spin wave spectrum and closes many of the nonlinear SW scattering channels. In such a case, the relaxation rate of the lowest-energy SW mode of the nanodot can reach zero, and self-oscillations of the mode can be

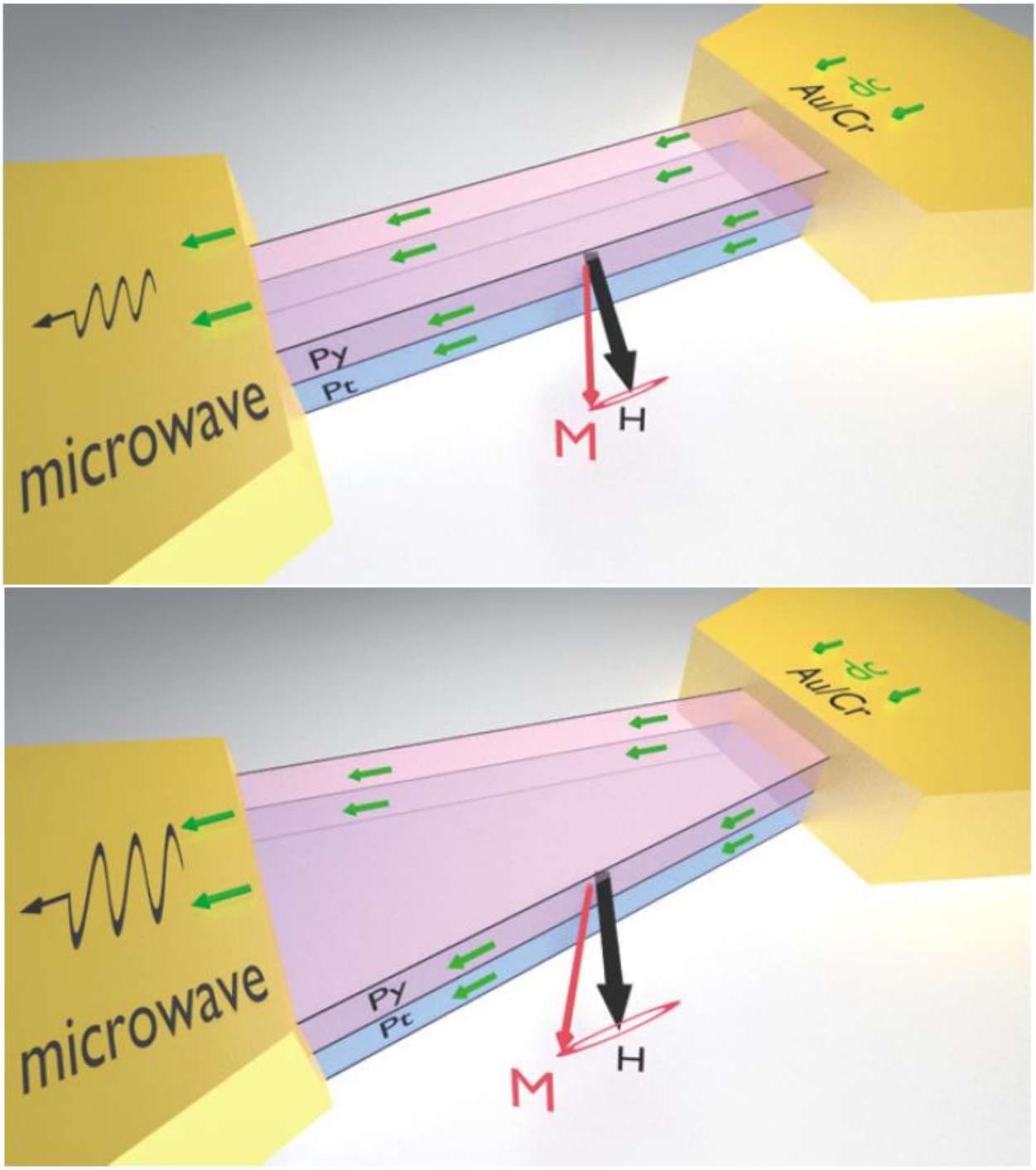

Figure 5.1 Schematic of the straight (a) and tapered (b) nanowire STO: applied magnetic field, electric bias current and precessing magnetization are shown by black, green and red arrows, respectively.

excited by the spin current [8]. Another route to excitation of self-oscillations by spin orbit torques is the application of a high spin current density to a nanoscale region of an extended ferromagnetic film by using the current concentrators [7,9,29,30]. In this case a nonlinear self-localized spin wave “bullet" mode can be excited [9,31,32]. Since the frequency of the bullet mode lies below the SW spectrum, the resonant scattering processes from this mode into a SW continuum are forbidden, which enables the self-sustained excitation of this large-amplitude mode [7,9,29,30]. The characteristic dimensions of this bullet mode is determined by the exchange length of the ferromagnet, and are typically below 100 nm [31,33].

Recently, we have shown that the spin orbit torques can excite self-oscillations of magnetization in micrometer-scale ferromagnets, namely in quasi-one-dimensional ferromagnetic nanowires [10]. The geometric confinement of the spin waves in nanowires suppresses some nonlinear scattering channels such as four-magnon scattering[34,35], which turns out to be sufficient for the excitation of sustainable self-oscillations over micrometer-scale regions of the nanowire.[10] In spite of the large excitation volume and the associated diminished impact of the random thermal torques on the magnetization dynamics, the spectral linewidth of the microwave signal generated by nanowire STOs was found to be comparable to that of nanoscale STOs [23,36-50].

This result can be attributed to the simultaneous excitation of several SW modes in nanowire auto-oscillators, because it is known that the interactions between the simultaneously excited self-oscillatory modes can substantially increase the linewidths of the generated modes[51,52]. Therefore, new methods for selective excitation of a single

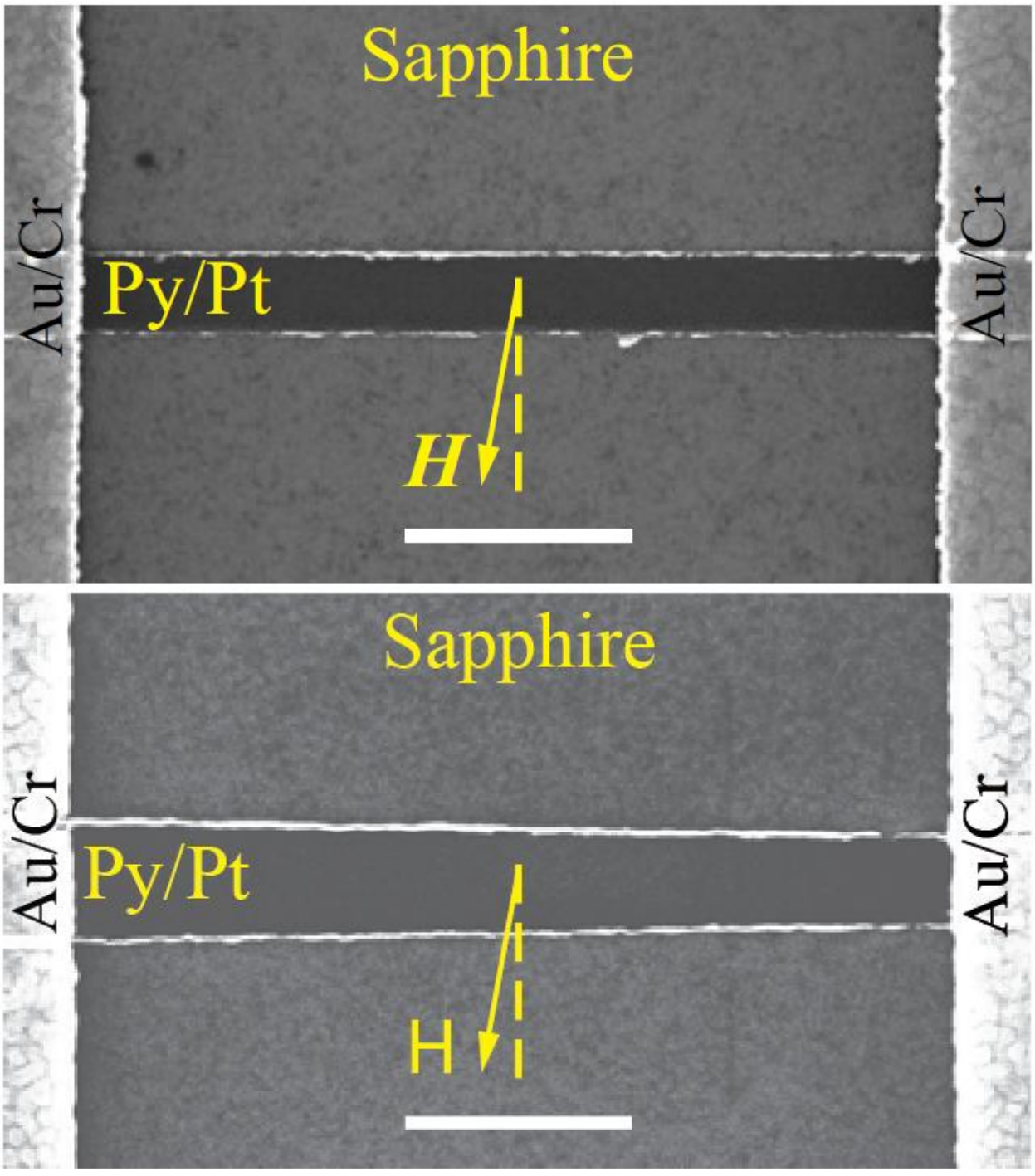

Figure 5.2 Scanning electron micrographs (SEM) of the straight (a) and tapered (b) nanowire STO samples. 500 nm white scale bars are shown in each SEM image.

self-oscillatory mode in a nanowire STO are highly desirable for the development of STO devices with high spectral purity.

In this paper, we report experiments demonstrating that the single-mode regime of operation and the associated phase noise reduction can be achieved via proper design of the nanowire STO shape. We show that STOs based on tapered nanowires, such as the one shown in Fig. 5.2b exhibit reduced phase noise, and a wider bias current range of single mode operation in comparison to the straight nanowire STOs of similar dimensions.

We employ numerical simulations to show that the spatial non-uniformity of the spin current density in the tapered nanowire STO is the key factor contributing to the improved phase noise. These simulations also reveal that the spin orbit torques excite a self-localized micrometer-scale bullet mode if nanowire SW modes exhibit negative nonlinear frequency shift. In the tapered nanowire devices, the spatial nonuniformity of the spin current density stabilizes the single-mode generation regime at higher bias currents. It also generates a confining potential for the bullet, which reduces the thermal fluctuations of the spatial position of this mode along the nanowire length, resulting in the reduction of the STO phase noise.

5.2. Results

5.2.1. Experiment

The nanowire STO samples based on AlO_x(2 nm)/Py(5 nm)/Pt(7 nm) multilayers were patterned on a sapphire substrate via e-beam lithography and liftoff as described in Chapter 2 (here Py = Permalloy = $Ni_{80}Fe_{20}$). The wires are 6 μm long with two Au (35

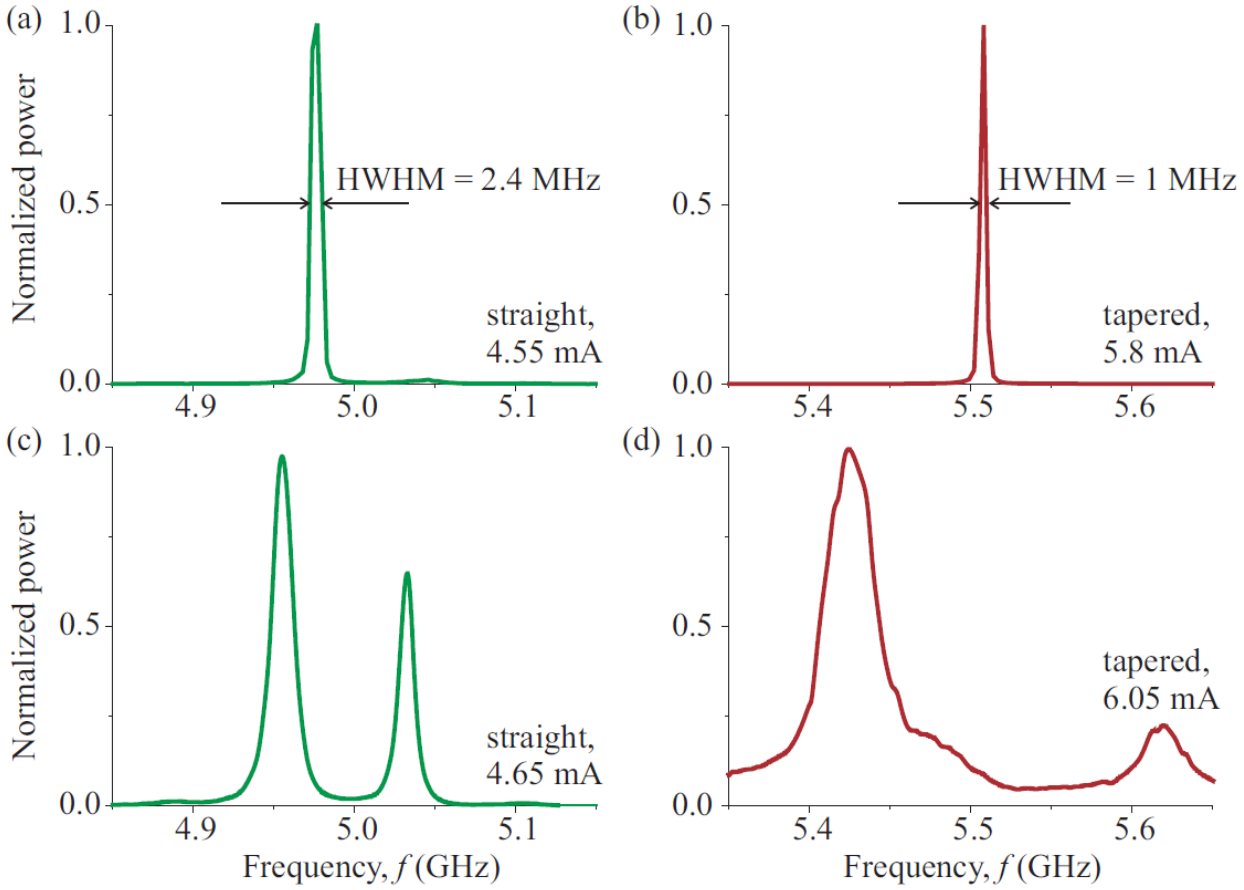

Figure 5.3 Normalized power spectra generated by the straight (a, c) and tapered (b, d) nanowire STOs at two bias current values.

nm)/Cr(7 nm) leads attached to each wire as shown in Fig. 5.1. The 1.9 μm long nanowire section between the leads is the STO active region, in which direct bias current applied to the wire generates the anti-damping spin orbit torque. The width of the straight nanowires is 190 nm, while the width of the tapered nanowires increases from 190 nm to 250 nm within the active region.

In our measurements, the magnetization of nanowires is saturated by a 700 Oe in-plane external magnetic field applied at the angle of 80^o with respect to the wire axis as shown in Fig. 5.1. Direct current I_{dc} applied to the nanowire excites self-oscillations of magnetization when the bias current exceeds a certain critical value (I_{dc} > 4.45mA for the straight wire and I_{dc} > 5.675mA for the tapered wire). The critical current is higher for the tapered nanowire because of its greater average width. Magnetization self-oscillations are converted into a microwave signal via anisotropic magneto-resistance of the Py layer [10]. The output microwave signal is amplified by a low-noise amplifier and measured by a spectrum analyzer.

All measurements reported in this paper were made at the bath temperature of 4.2 K, although the sample temperature near the critical current is approximately 150 K due to heating of the nanowire by the bias current [10]. We studied 3 straight and 3 tapered nanowire samples and found similar results for all these devices. In this paper, we present the data for one representative straight and one representative tapered nanowire STO. The spectra of microwave signals generated by the straight and tapered nanowire STOs at two bias current values above the critical currents are presented in Fig. 5.3. Here we only show the low-frequency group of peaks observed in the spectra. At higher bias currents, we have also detected a group of low-amplitude peaks, having frequency that was 0.8 GHz higher

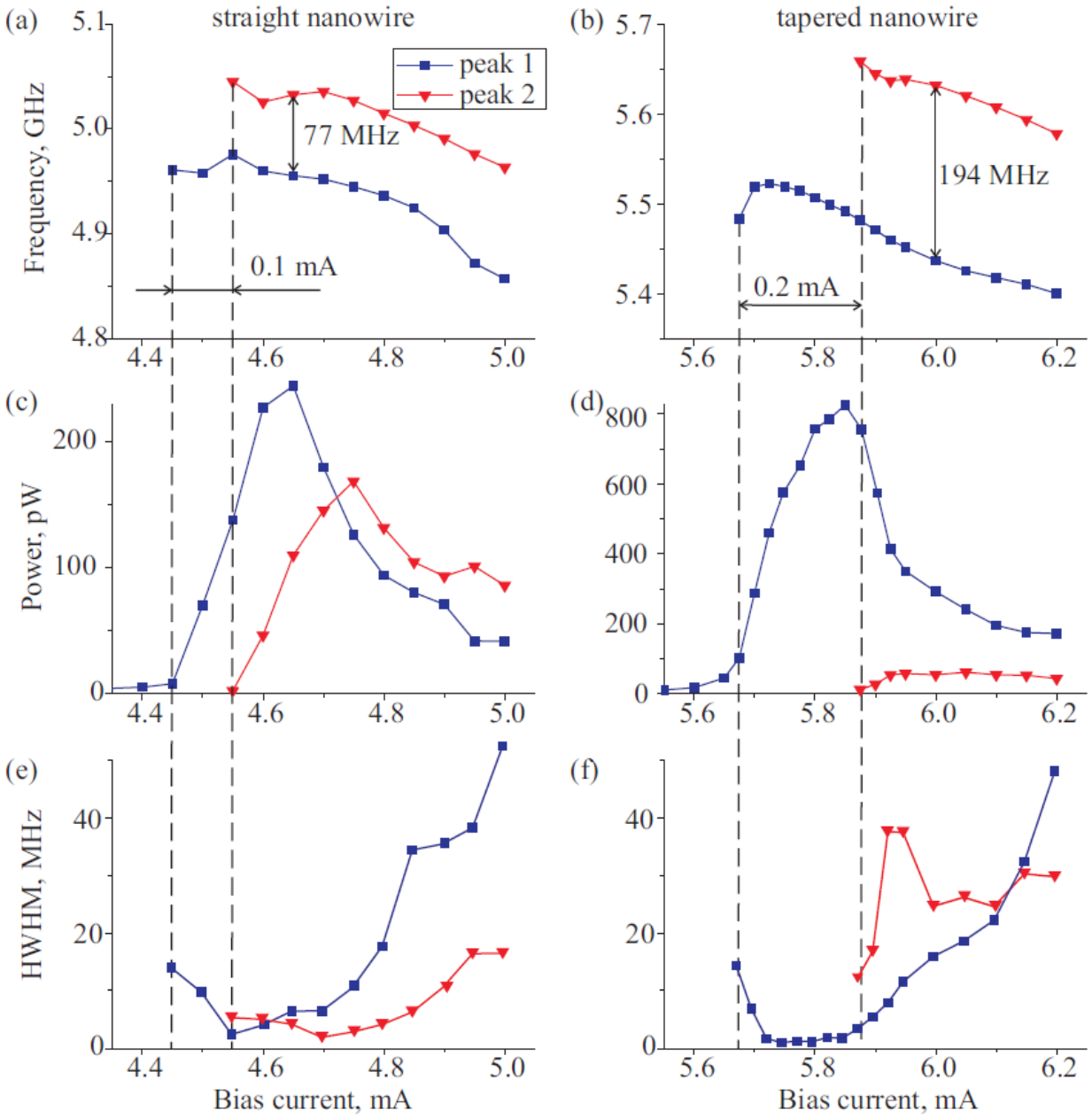

Figure 5.4 Measured dependence of the auto-oscillation frequency (a, b), integrated microwave emission power (c, d) and HWHM (e, f) on the bias current for the first (blue squares) and second (red triangles) peaks in the auto-oscillation spectra.

than the frequency of the low-frequency peaks. Following the analysis of Ref. 10, we identify the low-frequency peaks as the spin wave modes localized at the wire edges ("edge modes")[53,54], while the high-frequency peaks arise from the spin wave modes that have their maximum amplitudes within the central part of the wire ("bulk modes"). We also directly verified these conclusions using micromagnetic simulations of the spin wave spectra in the straight and tapered nanowires, as discussed in the next section. Since the critical current for the excitation of bulk modes is significantly higher than the range of the bias currents discussed in this work, we do not discuss the bulk modes in the rest of this paper.

For both the straight and tapered nanowire STOs, we observed a single spectral peak in a range of bias currents above the critical current I_c (Fig. 5.3(a,b)). The frequency of this first peak is higher in the tapered nanowire STO than in the straight nanowire STO. This happens because the average demagnetizing field decreases with the increase of the wire width and the average tapered wire width is greater than that of the straight wire. The emission power in the first peak increases with increasing bias current until the second peak appears in the spectrum at the second critical current (I_2 = 4.55mA for the straight nanowire STO; I_2 = 5.875mA for the tapered nanowire STO) as shown in Fig. 5.3(c,d). For $I > I_2$, the integrated power in the first mode decreases, and the spectral linewidth of this mode increases with increasing current, as illustrated in Fig. 5.3(c,d) and Fig. 5.4. At even higher bias current values, the third edge mode appears in the microwave emission spectra.

Here we will not discuss this complicated regime, and will restrict our discussion to the single- and double-mode STO operation regimes, focusing on the differences between

the straight and tapered nanowire devices. While the general features of the emission spectra as a function of the bias current are qualitatively similar for the straight and tapered nanowire STOs, there are significant quantitative differences. First, the current range of the single-mode operation of the tapered nanowire STO (0.2 mA) is twice as wide as that for the straight nanowire STO (0.1 mA) as illustrated in Fig. 5.4. Second, the frequency gap between the first and the second peaks in the generation spectrum is much wider for the tapered nanowire STO in comparison to the straight nanowire STO. Third, the minimum spectral linewidth (half width at half maximum or HWHM) in the single-mode auto-oscillation regime is significantly smaller for the tapered nanowire STO (1.0 MHz) than for the straight nanowire STO (2.4 MHz), as shown in Fig. 5.3. All these large quantitative differences between the two types of the STO cannot be attributed to a small difference of the average demagnetization fields, which results in a 10% difference in the edge mode frequency. In the next section we explain the origin of the observed significant impact of the nanowire shape on the spectral properties of nanowire STOs.

5.2.2. Theory

In order to visualize the spatial profiles of the observed self-oscillatory edge modes, our collaborator Tobias Schneider performed micromagnetic simulations of the magnetization dynamics in the nanowire STO. First, we employed the spectral mapping technique to calculate the edge spin wave mode profile in the linear regime (see Methods for details). Since the applied magnetic field makes different angles to the two edges of the tapered nanowire sample, the frequencies of the modes localized at the opposite edges are different. The spatial profile of the lowest-frequency edge mode calculated by the spectral

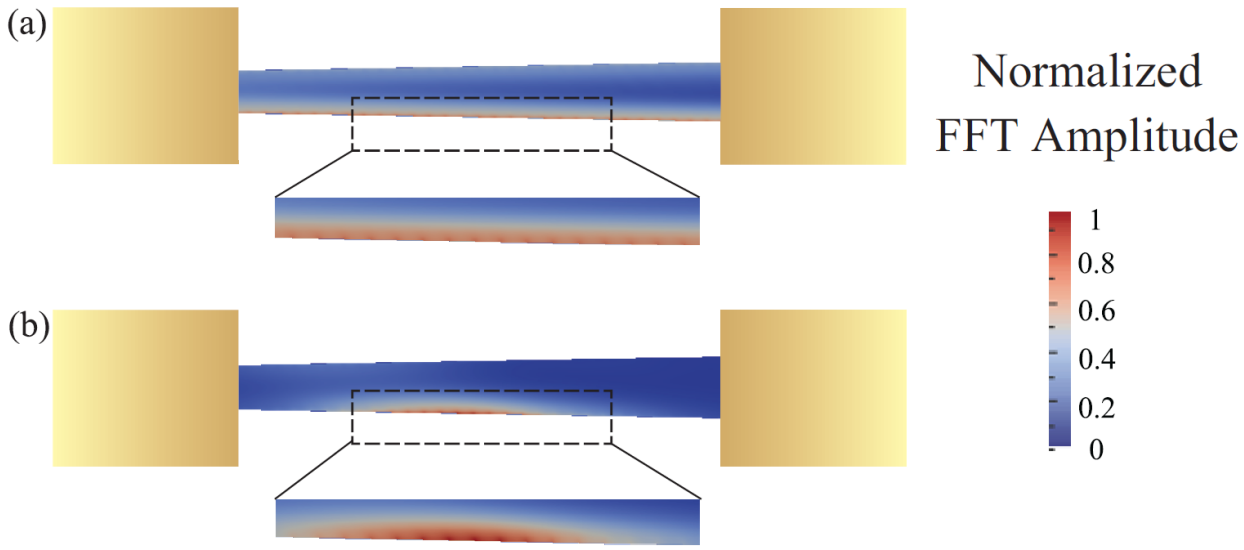

Figure 5.5 (a) Spatial profile of the lowest-frequency linear SW mode of the tapered nanowire. (b) Spatial profile of the self-oscillatory bullet mode excited by direct current exceeding the critical value. Dashed rectangles show a zoomed in view of the edge mode. Yellow rectangles represent the Au/Cr leads.

mapping technique for the tapered nanowire STO is shown in Fig. 5.5(a). The mode extends over the entire nanowire length and is strongly localized near one of the edges. We have also performed micromagnetic simulations of the self-oscillatory magnetic dynamics in this nanowire sample driven by spin orbit torque. Such simulations are very time-consuming because of the significant spatial extent of the nanowire and long transient dynamics. For this reason, we performed these simulations for only a single value of the bias current above the critical current. The spatial profile of the self-oscillatory mode driven by direct current is shown in Fig. 5.5(b). It is clear from this figure that the self-oscillatory nonlinear mode directly originates from the linear edge mode but shows a higher degree of localization near the middle of the nanowire STO active region. We also applied this type of micromagnetic analysis to the straight nanowire STO and observed a similar behavior with the main difference being localization of the edge mode at both edges of the nanowire due to the higher symmetry of the system. We note that in real nanowire samples, equivalence of the two edges is broken due to the random edge roughness and non-uniform edge damage, and thus the localization of the lowest-frequency edge mode near one of the edges is expected as well.

Since detailed micromagnetic simulations of the self-oscillatory dynamics as a function of the direct bias current are prohibitively time-consuming, our collaborator Roman Verba, Vasil Tiberkevich and Andrei N. Slavin develop a one-dimensional model describing current-driven magnetization dynamics in a nanowire STO. This model describes magnetization dynamics in the framework of nonlinear Ginzburg-Landau equation that is derived as a small-amplitude approximation of the Landau-Lifshitz equation:

$$\frac{\partial b}{\partial t} + (i + \alpha_G)\widehat{\Omega} * b + iN|b|^2 b - \sigma J(y)(1 - |b|^2)b = 0 \qquad (1)$$

Here b = b(y, t) is the complex amplitude of the dynamic magnetization in the excited SW mode, which depends only on the coordinate along the wire axis (y-axis) (the mode profile along the wire width, i.e. its localization near the wire edge, is assumed to be constant), α_G is the Gilbert damping constant, N is the nonlinear frequency shift, J(y) is the spatial distribution of the bias current density along the nanowire axis and σ is the spin orbit torque efficiency constant (see Methods).

The frequency operator $\widehat{\Omega}$ is given by:

$$\widehat{\Omega} * b \equiv \omega_0 b - \omega_M \lambda_{ex}^2 \frac{\partial^2 b}{\partial y^2} + \frac{\omega_M}{2\omega_0} \int G_{yy}(y - y')b(y')dy' \qquad (2)$$

where ω_0 is the spin wave resonance frequency in the linear regime, $\omega_M = \gamma\mu_0 M_s$ and λ_{ex} is the exchange length. In contrast to the previous studies[31], we also take into account the magnetodipolar interaction in the Damon-Eshbach geometry via the magnetostatic Green's function G_{yy}.

The sign of the nonlinear frequency shift N is the key factor determining the type of self-oscillatory magnetization dynamics driven by spin orbit torque. It is known that for negative nonlinear shift, a nonlinear self-localized solitonic bullet mode is favored under the action of anti-damping spin torque; while for positive nonlinear shift, no self-localization is found [9,31,32]. Fig. 5.4 demonstrates that the nonlinear frequency shift of the edge SW mode in our system is negative (N < 0), and, therefore, we should expect self-localization of the excited self-oscillatory mode. We also note that in the previously studied nanowire STO samples prepared via Ar plasma etching [10], positive nonlinear shift of the edge mode was observed, and the nonlinear mode self-localization did not take place. This

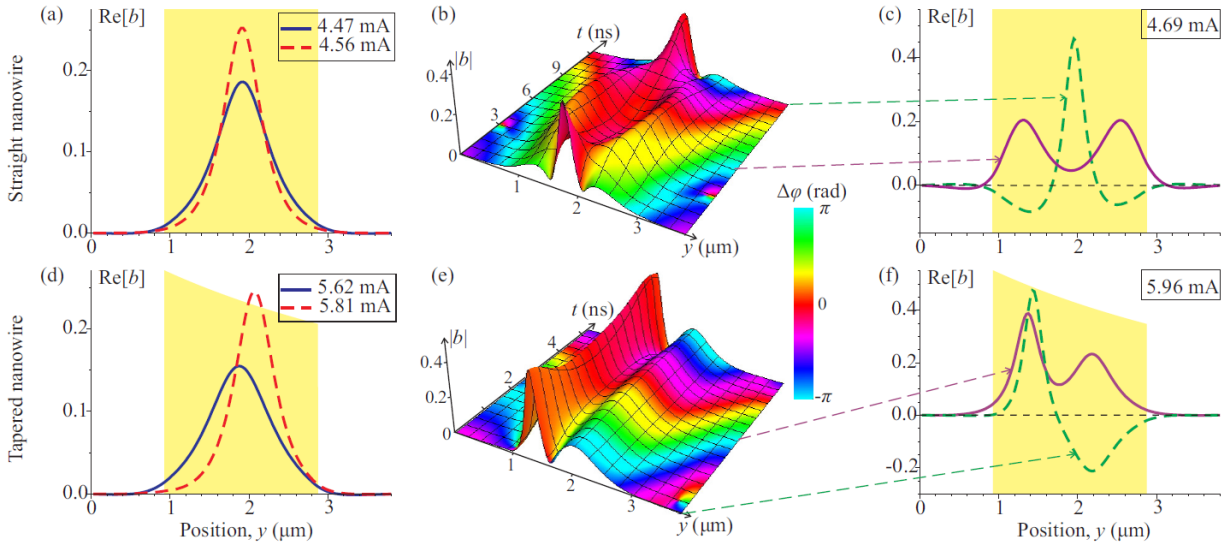

Figure 5.6 Profiles of the self-oscillatory bullet mode in the single-mode regime calculated from Eq. (1) for the straight (a) and tapered (d) nanowire STOs at different bias currents. The height of the yellow shaded area represents the spin current density within the STO active region. (b, e) Time evolution of the amplitude |b| and relative phase Δϕ (see Methods) of the magnetization oscillations in the double-bullet regime of self-oscillations. (c, f) Snapshots of the dynamic magnetization profile Re[b] at two values of time.

demonstrates a strong sensitivity of the nanowire STO properties to the degree of magnetic edge damage, which depends on the sample fabrication technique (see Methods for details). Fig. 5.5(b) illustrates that the excited self-oscillatory mode given by micromagnetic simulations is indeed a nonlinear self-localized bullet mode, as expected for $N < 0$. The self-localization is evident from the smaller spatial extent of the nonlinear mode in Fig. 5.5(b) along the wire length compared to the size of the linear mode in Fig. 5.5(a). The characteristic dimension of this bullet mode is approximately 1 μm, which is one order of magnitude larger than the size of the self-oscillatory bullet modes excited by spin torque in extended thin films in point contact STOs[9,31-33,40,42]. Such increase of the bullet size is a result of the enhanced role of the magnetic dipole interaction in the nanowire geometry. A detailed study of the effect of dipolar interaction on the bullet size will be presented elsewhere.

Fig. 5.6 illustrates the bullet mode profiles obtained from the numerical solution of the Ginzburg-Landau equation (see Methods for details). In the straight nanowire STO, a single bullet mode with its maximum in the center of the wire is excited above the critical current as shown in Fig. 5.6(a). The amplitude of this bullet mode increases and its width decreases with increasing bias current, which is a clear evidence of the nonlinear self-localization. When the current density reaches a second critical current I_2, another bullet mode is excited within the SHO active region as illustrated in Fig. 5.6(c). A similar type of the two-bullet excitation was previously observed in a point contact STO [55]. The double-bullet solution at $I > I_2$ is not stationary - the magnetization profile oscillates between the single-bullet and double-bullet configurations, as illustrated in Fig. 5.6(b, c). As a result of these mode profile oscillations, the spectrum of the voltage signal generated by the STO

develops two prominent peaks in agreement with our experimental observations. At higher currents, additional bullet modes sequentially enter the active region, and the resulting magnetization dynamics becomes very complex.

For the tapered nanowire STO, we solve the same Ginzburg-Landau equation, but with a spatially dependent current density J(y). Similar to the straight nanowire case, a nonlinear edge bullet mode is excited at the threshold current I_c. With increasing bias current, the size of this bullet mode decreases and the center of the mode shifts towards the wider end of the nanowire as shown in Fig. 5.6(d). At a higher critical current I_2, a second bullet mode appears in the left part of the active region (where current density is higher). In contrast to the straight nanowire, where the mode profile oscillates between one- and two-bullet mode configurations, two different bullet modes coexist at all times in the tapered nanowire, as evident from Fig. 5.6(e). These two bullets oscillate with different frequencies - the left bullet experiencing higher current density has a lower oscillation frequency, as illustrated in Fig. 5.6(e) by the linear increase of the phase difference between the two bullet solutions $\Delta\phi$ with time (see Methods for details). This can be also seen in Fig. 5.6(f) where the two different bullet modes are in phase at one moment of time, and have opposite phases at a later moment. The Fourier transform of the voltage signal arising from this double-bullet dynamics exhibits two distinct spectral peaks corresponding to the two different bullet mode frequencies.

Fig. 5.7 shows the calculated self-oscillatory mode frequencies given by Eq.(1) versus the magnitude of the direct bias current. These dependences are in good agreement with the experimental data in Fig. 5.4: the single-mode current range (I_2 - I_c) and the inter-mode

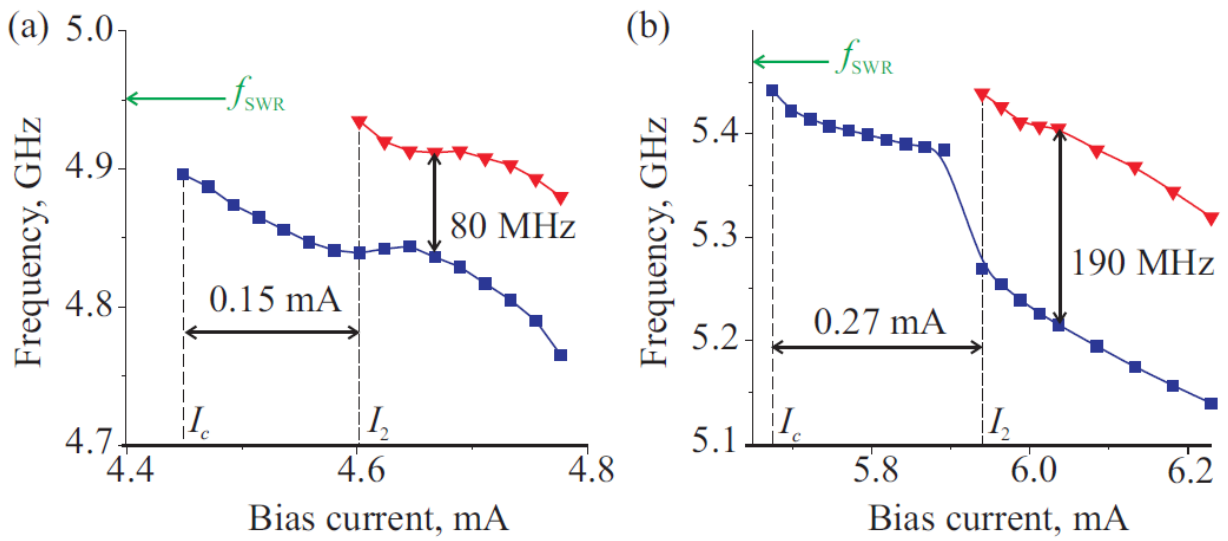

Figure 5.7 Self-oscillatory mode frequency as a function of the bias current calculated by numerically solving Eq.(1) for the straight (a) and tapered (b) nanowire STOs; blue squares - first bullet mode, red triangles - second bullet mode. Lines are guide for eyes and green arrows show the resonance frequency of the edge mode in the linear regime $f_{SWR} = \omega_0/2\pi$.

frequency gap in the double-mode regime are significantly wider for the tapered nanowire STO. The wider single-mode current range is a direct consequence of the current-induced shift of the position of the first bullet mode away from the center of the active region towards the wider end of the nanowire (towards lower current density). This current-induced shift allows the first bullet mode to remain within a region of lower current density (and thus, within a single-mode regime) over a wider range of the applied bias currents. The wider inter-mode frequency gap in the tapered wire arises from the spatially non-uniform current density as well. Since the two bullet modes are spatially separated along the wire length, they are exposed to different spin current densities in the tapered nanowire device. This results in significantly different amplitudes of the two bullet modes, as illustrated in Fig. 5.6(e), and due to the nonlinear frequency shift, an enhancement of the inter-mode frequency gap.

The reduced phase noise of the tapered nanowire STO can be also explained by the spatially non-uniform spin current density. In the straight nanowire devices, the bullet mode position is weakly confined to the center of the nanowire by its interaction with the active region boundaries. Therefore, its position along the wire is highly susceptible to thermal fluctuations, resulting in fluctuations of measured voltage signal. In contrast, the bullet position in the tapered nanowire is mainly determined by the nonuniformity of the applied current density. Therefore, there is a current-induced restoring force that reduces the amplitude of thermal fluctuations of the bullet position along the wire length, thereby reducing the mode's phase noise. Another important effect which reduces the phase noise in the tapered nanowire STO is the enhanced bias current range of a single-mode

generation. This results in higher generation power in the single-mode regime, which decreases the phase noise of the generated signal [23, 56].

5.3. Discussion

In this work, we demonstrate that phase noise of nanowire-based spin orbit torque oscillators can be significantly reduced via the nanowire shape design. We experimentally show that the single-mode regime of the STO operation is extended over a wider current range in the tapered nanowire STOs compared to the straight nanowire STOs. The degree of spectral purity of the microwave signal generated by the tapered nanowire STO is also significantly improved in comparison to the straight nanowire STO devices.

To understand the observed effect of the nanowire shape on the STO operation, we developed a one-dimensional Ginzburg-Landau model of a nanowire STO. This model reveals that non-linear self-localized bullet modes are excited in the nanowire under the action of spin orbit torque if the excited spin wave modes possess negative non-linear frequency shift. These bullet modes have micrometer-scale spatial dimensions, which is an order of magnitude greater than the dimensions of the bullet modes excited in point contact STO devices, due to the enhanced role of magnetodipolar interaction in one-dimensional systems.

The model demonstrates that spatially non-uniform spin current density in tapered nanowire STOs is the key factor leading to the phase noise reduction in these devices. The non-uniform spin current density results in a current-induced displacement of the bullet mode from the nanowire center towards the region of lower current density, which extends the single-mode generation regime to a wider range of bias currents. In addition,

the nonuniform current density provides a restoring force that reduces the amplitude of thermal fluctuations of the bullet mode position along the nanowire length, thereby decreasing the STO phase noise. The model also predicts a transition to a double-mode regime of the STO operation experimentally observed at higher values of the bias current.

5.4. Methods

5.4.1. Sample information.

Fabrication of the STO devices are discussed in detail in Chapter 2, and liftoff technique is used for all straight and tapered nanowires.

The liftoff technique employed for fabrication of the nanowire STOs minimizes the nanowire edge damage, thereby decreasing the critical current for excitation of the edge mode self-oscillations. The critical current for excitation of the edge modes is lower than that for the bulk modes for the samples studied in this work. This result is in contrast with Chapter 3 [10], in which the critical currents of the bulk and edge groups of modes were nearly identical. The reason for this difference is the different methods of the device fabrication. Ar plasma etching of the nanowires employed in Ref. 10 creates significant edge damage, increases the damping parameter in the edge region, thereby increasing the critical current for excitation of the edge modes.

5.4.2. Micromagnetic simulations.

Micromagnetic simulations are performed by using a modified version of the MuMax3 software package by Tobias Schneider[57]. The computational domain containing the entire 6 μm long nanowire is discretized into 4096X256X1 cells, which results in the cell size of approximately 1.5X1.5X5 nm^3. The saturation magnetization M_s = 530X10^3 A/m and

the exchange stiffness A = 0.5X 10^{-11} J/m were previously determined for this type of STO samples [10]. Spin wave eigenmode frequencies of the nanowire are found as peak positions in the Fourier transform of the dynamics magnetization excited by a sinc-shaped out-of-plane magnetic field pulse of 0.5 Oe amplitude and 50 ps duration [59]. The eigenmode spatial profiles are reconstructed by plotting the cell-specific Fourier amplitudes at the mode eigenfrequency. The auto-oscillatory mode of the system is found by solving the LLG equation with antidumping spin torque applied to the 1.9 μm long active region of the nanowire. The simulation time is set to 2.5 μs to minimize the transient contributions to the self-oscillatory dynamics. The spatial profile of the auto-oscillatory mode is reconstructed by plotting the cell-specific Fourier amplitudes at the self-oscillatory mode frequency.

5.4.3. Numerical solution of the Ginzburg-Landau equation.

The Ginzburg-Landau equation (Eq. (1)) is derived for a dimensionless complex magnetization amplitude b, which is related to the dynamic magnetization components as $b = (M_y + i\varepsilon M_z)/\sqrt{1+\varepsilon^2}M_s$. Here ξ describes the ellipticity of the magnetization precession, which is assumed to be constant. The values of ω_0 and δ used in the simulations are chosen to fit the experimentally measured frequency of self-oscillations at the threshold, and the threshold bias current I_c. The value of the nonlinear frequency shift N = -0.1 ω_M is derived from the measured dependence of the first self-oscillatory mode frequency on the bias current [23]. The other material parameters: $\lambda_{ex} = \sqrt{2A/\mu_0 M_s^2}$, $\omega_M = \gamma\mu_0 M_s$, α_G are chosen to be identical to those used in our micromagnetic simulations. The integral kernel G_{yy} is approximated by the Green's function of a 25 nm

wide wire [58], because the localization length of the edge mode given by our micromagnetic simulations is approximately 25 nm. The spatial domain is discretized into sufficiently small cells, and the resulting set of equations is solved in the time domain starting from a random distribution of b until a stationary state of magnetic self-oscillations is reached. To illustrate dynamics of the relative phase between the two bullets in the double-bullet solution of Eq. (1), we multiplied b(t) by $\exp[i\omega_1 t]$, where $\omega 1$ is the frequency of the first bullet mode. The relative phase between the two bullets shown in Fig. 5.6(b,e) is simply $\Delta\ \Phi = \mathrm{Arg}\ [b(t)e^{i\omega 1t}]$. This part is done by Roman Verba, Vasil Tiberkevich and Andrei N. Slavin.

5.5 References

1. Kimura, T., Otani, Y., Sato, T., Takahashi, S. and Maekawa, S. Room-temperature reversible spin Hall effect. *Phys. Rev. Lett.* **98**, 156601 (2007).

2. Ando, K., et al. Electric manipulation of spin relaxation using the spin Hall effect. *Phys. Rev. Lett.* **101**, 036601 (2008).

3. Hahn, C., Loubens, G. de., Klein, O., Viret, M., Naletov, V. V. and Youssef, J. Ben. Comparative measurements of inverse spin Hall effects and magnetoresistance in YIG/Pt and YIG/Ta. *Phys. Rev. B*. **87**, 174417 (2013).

4. Pai, C.-F., Liu, L., Tseng, H. W., Ralph, D. C. and Buhrman, R. A. Spin transfer torque devices utilizaing the giant spin Hall effect of tungsten. *Appl. Phys. Lett.* **101**, 122404 (2012).

5. Liu, L., Pai, C.-F., Li, Y., Tseng, H. W., Ralph, D. C. and Buhrman, R. A. Spin-torque switching with the giant spin Hall effect of tantalum. *Science* **336**, 555 (2012).

6. Woo, S. -H., Mann, M., Tan, A. J., Caretta, L. and Beach, G. S. D. Enhanced spin-orbit torques in Pt/Co/Ta heterostructures. *Appl. Phys. Lett*. **105**, 212404 (2014).

7. Demidov, V. E., et al. Magnetic nano-oscillator driven by pure spin current. *Nat. Mater.* **11**, 1028 (2012).

8. Liu, L., Pai, C.-F., Ralph, D. C. and Buhrman, R. A. Magnetic oscillations driven by the spin Hall effect in 3-terminal magnetic tunnel junction devices. *Phys. Rev. Lett*. **109**, 186602 (2012).

9. Liu, R. H., Lim, W. L. and Urazhdin, S. Spectral characteristics of the microwave emission by the spin Hall nano-oscillator. *Phys. Rev. Lett*. **110**, 147601 (2013).

10. Duan, Z., et al. Nanowire spin torque oscillator driven by spin orbit torques. *Nature Comm.* **5**, 5616 (2014).

11. Kim, J., et al. Layer thickness dependence of the current-induced effective field vector in Ta|CoFeB|MgO. *Nature Mater*. **12**, 240 (2012).

12. Tserkovnyak, Y. and Bender, S. A. Spin Hall phenomenology of magnetic dynamics. *Phys. Rev. B* **90**, 014428 (2014).

13. Zhang, S., Spin Hall effect in the presence of spin diffusion. *Phys. Rev. Lett*. **85**, 393 (2000).

14. Sinova, J., Culcer, D., Niu, Q., Sinitsyn, N. A., Jungwirth, T. and MacDonald, A. H. Universal intrinsic spin Hall effect. *Phys. Rev. Lett*. **92**, 126603 (2004).

15. Haney, P. M., Lee, H.-W., Lee, K.-J., Manchon, A. and Stiles, M. D. Current induced torques and interfacial spin-orbit coupling: Semiclassical modeling. *Phys. Rev. B* **87**, 174411 (2013).

16. Fan, X., Wu, J., Chen, Y., Jerry, M. J., Zhang, H. and Xiao, J. Q. Observation of the nonlocal spin-orbital effective field. *Nature Comm* **4**, 1799 (2013).

17. Bhowmik, D., You, L. and Salahuddin, S. Spin Hall effect clocking of nanomagnetic logic without a magnetic field. *Nature Nanotech*. **9**, 59 (2014).

18. Dyakonov, M. I. and Perel, V. I. Possibility of orienting electron spins with current. *Sov. Phys. JETP Lett*. **13**, 467 (1971).

19. Hirsch, J. E. Spin Hall effect. *Phys. Rev. Lett*. **83**, 1834 (1999).

20. Hoffmann, A. Spin Hall effects in metals. *IEEE Trans. Magn*. **49**, 5172 (2013).

21. Slonczewski1996, J. C. Current-driven excitation of magnetic multilayers. *J. Magn. Magn. Mater*. **159**, L1 (1996).

22. Berger, L. Emission of spin waves by a magnetic multilayer traversed by a current. *Phys. Rev. B* **54**, 9353 (1996).

23. Slavin, A. and Tiberkevich, V. Nonlinear auto-oscillator theory of microwave generation by spin-polarized current. *IEEE Trans. Magn*. **45**, 1875 (2009).

24. Bazaliy, Ya. B., Jones, B. A. and Zhang, S.-C.Modification of the Landau-Lifshitz equation in the presence of a spin-polarized current in colossal- and giant-magnetoresistive materials. *Phys. Rev. B* **57**, R3213 (1998).

25. Demidov, V. E., Urazhdin, S., Edwards, E. R. J. and Demokritov, S. O. Wide-range control of ferromagnetic resonance by spin Hall effect. *Appl. Phys. Lett*. **99**, 172501 (2011).

26. Rousseau, O. and Viret, M. Interaction between ferromagnetic resonance and spin currents in nanostructures. *Phys. Rev. B* **85**, 144413 (2012).

27. Hamadeh, A., et al. Full control of the spin-wave damping in a magnetic insulator using spin orbit torque. *Phys. Rev. Lett*. **113**, 197203 (2014).

28. Demidov, V. E., et al. Control of magnetic fluctuations by spin current. *Phys. Rev. Lett.* **107**, 107204 (2011).

29. Demidov, V. E., Urazhdin, S., Zholud, A., Sadovnikov, A. V. and Demokritov, S. O. Nanoconstriction-based Spin-Hall nano-oscillator. *Appl. Phys. Lett*. **105**, 172410 (2014).

30. Demidov, V. E., et al. Spin-current nano-oscillator based on nonlocal spin injection. Sci. Rep. 5, 8578 (2015).

31. Slavin, A. and Tiberkevich, V. Spin wave mode excited by spin-polarized current in a magnetic nanocontact is a standing self-localized wave bullet. *Phys. Rev. Lett*. **95**, 237201 (2005).

32. Bonetti, S., et al. Experimental evidence of self-localized and propagating spin wave modes in obliquely magnetized current-driven nanocontacts. *Phys. Rev. Lett*. **105**, 217204 (2010).

33. Consolo, G., et al. Excitation of self-localized spin-wave bullets by spin-polarized current in in-plane magnetized magnetic nanocontacts: A micromagnetic study. *Phys. Rev. B* **76**, 144410 (2007).

34. Pincus, P., Sparks, M. and LeCraw, R. C. Ferromagnetic relaxation. II. The role of four-magnon processes in relaxing the magnetization in ferromagnetic insulators. *Phys. Rev.* **124**, 1015 (1961).

35. Dobin, A. Yu. and Victora, R. H. Intrinsic nonlinear ferromagnetic relaxation in thin metallic films. *Phys. Rev. Lett*. **90**, 167203 (2003).

36. Grollier, J., Cros, V., and Fert, A. Synchronization of spin-transfer oscillators driven by stimulated microwave currents. *Phys. Rev. B* **73**, 060409 (2006).

37. Georges, B., et al. Origin of the spectral linewidth in nonlinear spin-transfer oscillators based on MgO tunnel junctions. *Phys. Rev. B* **80**, 060404 (2009).

38. Houssameddine, D., et al. Spin-torque oscillator using a perpendicular polarizer and a planar free layer. *Nature Mater*. **6**, 447 (2007).

39. Ozyilmaz, B., Kent, A. D., Sun, J. Z., Rooks, M. J. and Koch, R. H. Current-induced excitations in single cobalt ferromagnetic layer nanopillars. *Phys. Rev. Lett*. **93**, 176604 (2004).

40. Tsoi, M., et al. Generation and detection of phase-coherent current-driven magnons in magnetic multilayers. *Nature* **406**, 46 (2000).

41. Kiselev, S., et al. Microwave oscillations of a nanomagnet driven by a spin polarized current. *Nature* **425**, 380 (2003).

42. Rippard, W. H., Pufall, M. R., Kaka, S., Russek, S. E. and Silva, T. J. Direct-current induced dynamics in point $Co_{90}Fe_{10}/Ni_{80}Fe_{20}$ contacts. *Phys. Rev. Lett*. **92**, 027201 (2004).

43. Deac, A. M., et al. Bias-driven high-power microwave emission from MgO-based tunnel magnetoresistance devices. *Nature Phys*. **4**, 803 (2008).

44. Arai, H., Matsumoto, R., Yuasa, S. and Imamura, H. Spin-torque-induced oscillation at zero bias field in a magnetoresistive nanopillar with a free layer with first- and second-order uniaxial anisotropy. *Appl. Phys. E*. **8**, 8 (2015).

45. Mistral, Q., et al. Current-driven microwave oscillations in current perpendicular-to-plane spinvalve nanopillars. *Appl. Phys. Lett*. **88**, 192507 (2006).

46. Nazarov, A. V., et al. Spin transfer stimulated microwave emission in MgO magnetic tunnel junctions. *Appl. Phys. Lett*. **88**, 162504 (2006).

47. Tserkovnyak, Y., et al. Nonlocal magnetization dynamics in ferromagnetic heterostructures. *Rev. Mod. Phys.* **77**, 1375 (2005).

48. Zeng, Z., et al. Ultralow-current-density and bias-field-free spin-transfer nano-oscillator. *Sci. Rep*. **3**, 1426 (2013).

49. Krivorotov, I. N., et al. Time-domain measurements of nanomagnet dynamics driven by spin transfer torques. *Science* **307**, 228 (2005).

50. Wang, Y. and Sham, L. J. Quantum dynamics of a nanomagnet driven by spin-polarized current. *Phys. Rev. B* **85**, 092403 (2012).

51. Iacocca, E., Heinonen, O., Muduli, P. K., and Akerman, J. Generation linewidth of modehopping spin torque oscillators. *Phys. Rev. B* **89**, 054402 (2014).

52. Sharma, R., Durrenfeld, P., Iacocca, E., Heinonen, O. G., Akerman, J. and Muduli, P. K. Modehopping mechanism generating colored noise in a magnetic tunnel junction based spin torque oscillator. *Appl. Phys. Lett*. **105**, 132404 (2014).

53. Jorzick, J., et al. Spin wave wells in nonellipsoidal micrometer size magnetic elements. *Phys. Rev. Lett*. **88**, 047204 (2002).

54. Park, J. P., Eames, P., Engebretson, D. M., Berezovsky, J. and Crowell, P. A. Spatially resolved dynamics of localized spin-wave modes in ferromagnetic wires. *Phys. Rev. Lett*. **89**, 277201 (2002).

55. Ulrichs, H., Demidov, V. E. and Demokritov, S. O. Micromagnetic study of auto-oscillation modes in spin-Hall nano-oscillators. *Appl. Phys. Lett.* **104**, 042407 (2014).

56. Kim, J.-V., Tiberkevich, V. and Slavin, A. N. Generation linewidth of an auto-oscillator with a nonlinear frequency shift: spin-torque nano-oscillator. *Phys. Rev. Lett*. **100**, 017207 (2008).

57. Vansteenkiste, A., et al. The design and verification of MuMax3. *AIP Advances* **4**, 107133 (2014).

58. Guslienko, K. Y. and Slavin, A. N. Magnetostatic Green's functions for the description of spin waves in finite rectangular magnetic dots and stripes. *J. Magn. Magn. Mater*. **323**, 2418 (2011).

59. Venkat, G., et al. Proposal for a standard micromagnetic problem: Spin wave dispersion in a magnonic waveguide. *IEEE Trans. Magn*. **49**, 524 (2013).

Chapter 6.Parametric resonance in Pt/Py nanowires tuned by Spin Hall Effect

Parametric resonance and direct linear excitation of Pt/$Ni_{80}Fe_{20}$ nanowires are experimentally studied and compared. It is found that, for each spin wave mode of edge and bulk mode that is directly excited in the nanowire, it can also be parametrically excited by driving at twice the resonance frequency. Pure spin current generated by Pt layer due to spin Hall effect can tune the relaxation characteristics and the threshold current of the parametric excitation of each mode to a large degree, and the linear dependence of onset current on spin Hall effect can be used to accurately fit for the critical current of each mode that is excited in the nanowire.

6.1 Introduction

Pure spin current from spin Hall effect, as demonstrated in Chapter 4 and 5, can excite steady state self-oscillation in nanowire spin hall oscillators. The ability to controllably change the dynamical magnetic damping with pure spin current also provides a unique opportunity to study nonlinear dynamic magnetic phenomena, since the threshold of these nonlinear behaviors linearly depends on the relaxation characteristics, which can be tuned by spin Hall effect. He we demonstrate parametric resonance in Pt/Py nanowires tuned by the spin Hall effect. We show that we can excite parametric resonance at relatively low microwave power, and achieve large amplitude of parametric resonance of both bulk and edge spin wave modes. We demonstrate the using the linearly dependence of microwave threshold on spin Hall effect, we can accurately determine mode dependent damping parameter, thus providing insights into mode dependent oscillation dynamics.

6.2 Results

The nanowire devices studied in this work are patterned from Pt(5)/Py(5)/AlO_x(4nm)/GaAs (Py = Permalloy=$Ni_{80}Fe_{20}$) multilayers deposited by magnetron sputtering. Multilayer nanowires that are 6 μm long and 190 nm wide are defined via e-beam lithography and Ar plasma etching. Two Au(35)/Cr(7) leads are attached to each nanowire with 1.8 um gap between the leads, which defines the active region of the device as shown in Fig. 6.1. When current is applied into the nanowire, spin Hall effect from Pt layer generates and injects pure spin current into Py layer from spin Hall effect [5,6,7,8,9,10], which modifies the effective damping [1,2]. Zero effective damping and Py magnetization auto oscillation can be reached under high enough DC current, which is

known as critical current I_c [Chapter 3, 4]. Besides auto oscillation, driven oscillation can be achieved with RF current, which generates RF spin orbit torque and RF Oersted field. When RF frequency matches the natural resonance frequency, maximum driven oscillation amplitude is observed, and this direct excitation is essentially spin Hall based ST-FMR[12]. Driven Py magnetization can also be achieved parametrically when RF frequency matches not the resonance frequency, but twice the resonance frequency. Under this circumstance, RF current modifies the effective damping and resonance frequency (from Oersted field oscillation) at twice the resonance frequency, which lowers the effective damping at the resonance frequency and can also excite magnetization dynamics [15, 16, 17, 18, 19, 20, 21, 22, 23, 24, 25]. Like auto oscillation, nonlinear magnetization dynamics of parametric resonance is also a threshold effect: it only happens when RF modulation is higher than the RF threshold I_{th} when it can bring the effective damping to zero, and this distinct onset behavior, together with the twice frequency drive can be used to differentiate parametric resonance from direct resonance. I_{th} is proportional to the relaxation characteristics, which is known to be able to be tuned by pure spin current from spin Hall effect, and can be tuned by DC current in the Pt/Py nanowire [18, 24]. In this chapter, we focus on driven oscillation of Py magnetization with RF current, under the influence of DC which is smaller than the critical current I_c.

To study RF driven magnetization dynamics, we apply a saturating magnetic field (H>450 Oe) in the plane of the sample at the direction perpendicular to the nanowire axis (±0.1 degrees). In this configuration, spin current polarization from spin Hall effect is parallel to saturated magnetization along the nanowire hard axis, and modulation of

effective damping is maximized. We apply a DC current in the direction that lowers the effective damping and with magnitude smaller than I_c, which lowers the effective damping to a smaller value. A modulated RF current is also applied into the nanowire through a bias tee, and the rectified voltage is monitored by a lock-in amplifier [11]. This setup allows to measure direct excitation and parametric excitation of Py magnetization at the same time. When driven magnetization dynamics is achieved, either from direct excitation or parametric excitation, Py resistance oscillates from the anisotropic magnetoresistance.

For hard axis field direction, spin current polarization is parallel to saturated magnetization and spin torque is minimum and ineffective in the excitation of direct excitation. Also dynamic Oersted field is parallel to the static saturated magnetization. At the same time, $\cos^2\theta$ dependence of Py layer anisotropic magnetoresistance does not mix with the direct linear drive to give a dc voltage, and as a result, direct dynamic magnetization is hard to excite and hard to detect electrically. But it is the optimum field direction for parametric excitation of saturated magnetization: both dynamic Oersted field and effective damping oscillation are maximum in this configuration. At the same time, $\cos^2\theta$ dependence of Py layer AMR oscillation mixes well with the twice frequency RF current drive in the parametric resonance. As a result, bigger oscillation amplitude and voltage signal can be expected from parametric resonance.

Using the Landau Liftshitz Gilbert equations for the macrospin of a thin film, we can derive that voltage signal of parametric resonance is composed of photoresistance and photovoltage, and grows from 0 from threshold current I_{th} in the following pattern.

$$V = I_{DC}\Delta R + I_{rf}R_{rf}\cos(2\psi) \propto 2I_{DC}\sqrt{I_{rf}^2 - I_{th}^2} + (I_{rf}^2 - I_{th}^2)$$

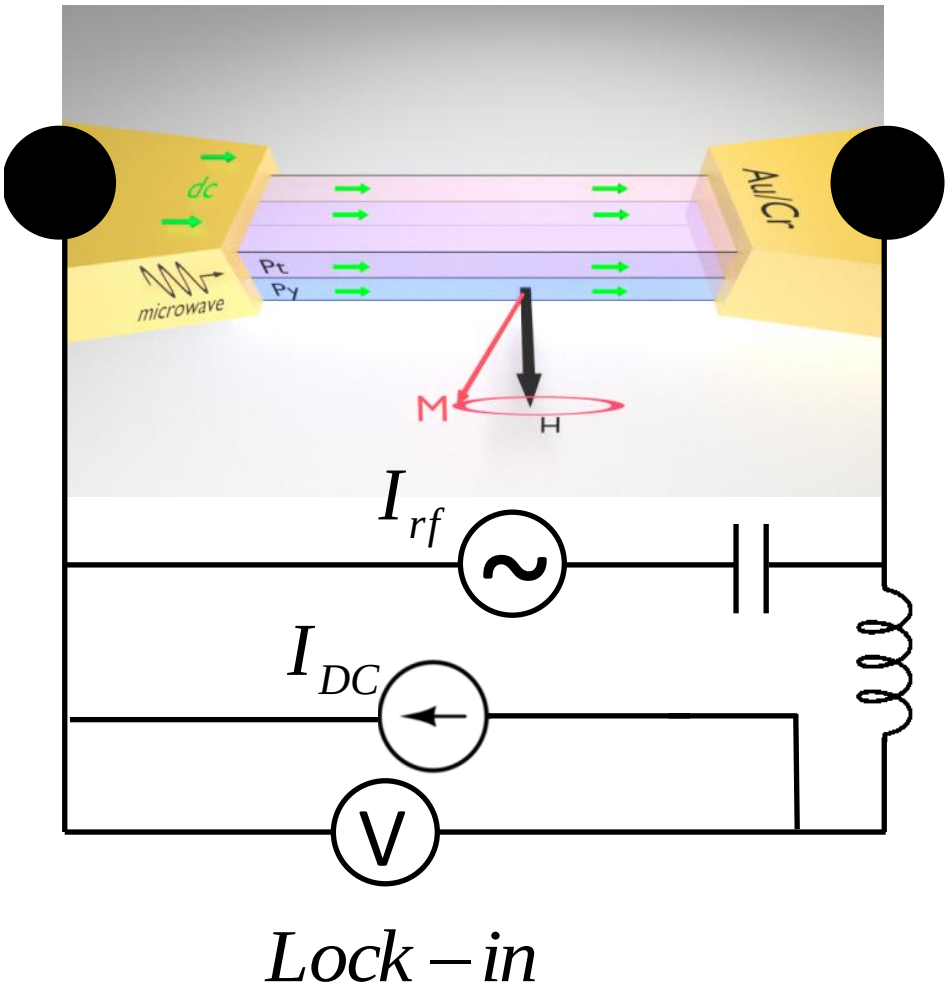

Figure 6.1 Layout of the experiment setup. Constant I_{DC} and modulated fixed frequency I_{rf} are applied to the Pt/Py nanowire and rectified voltage FMR signal is measured as a function of external field by the Lock-in amplifier.

Spin pumping combined with inverse SHE in the Pt layer can also give rise to an additional dc voltage term.[10, 12] However, due to the second order in θ_{SH}, as well as the strong ellipticity of the oscillation, this contribution is orders of magnitude smaller than the signal and is negligible.[12]

In Fig 6.2. We plot voltage spectra of the measurement as a function of frequency and magnetic field, with Irf=0.3mA and I_{DC}=2.2mA, which is just below the oscillation critical current and brings down the effective damping close to 0. We can see that multiple modes are excited. By comparing to Ferromagnetic Resonance (FMR) data from a similar sample, [Chapter 3], we can identify the two lowest frequency modes as direct excitation of edge mode and bulk mode (marked as E and B in the figure). This is due to the nonuniform internal spatial magnetic field from the demagnetization field which resulted in smaller effective at the edge of the nanowire [14]. It can be seen that bulk mode signal quickly drops to zero as hard axis field magnitude increases, and this is expected for ineffective drive of parallel spin current and ineffective voltage mixing to the saturated bulk magnetization as we mentioned before. For the edge mode, however, the signal is always pronounced even for the maximum field of 1500 Oe in the measurement. It means that edge mode excitation region, which is located along the edges of the nanowire, is never aligned along the field direction in the measurement due to stronger demagnetization field. Also it can be noted that bulk and edge mode frequencies in Fig 6.2 are slightly smaller than FMR frequencies in Chapter 4, which is due to the bigger Oersted field from the DC current used here.

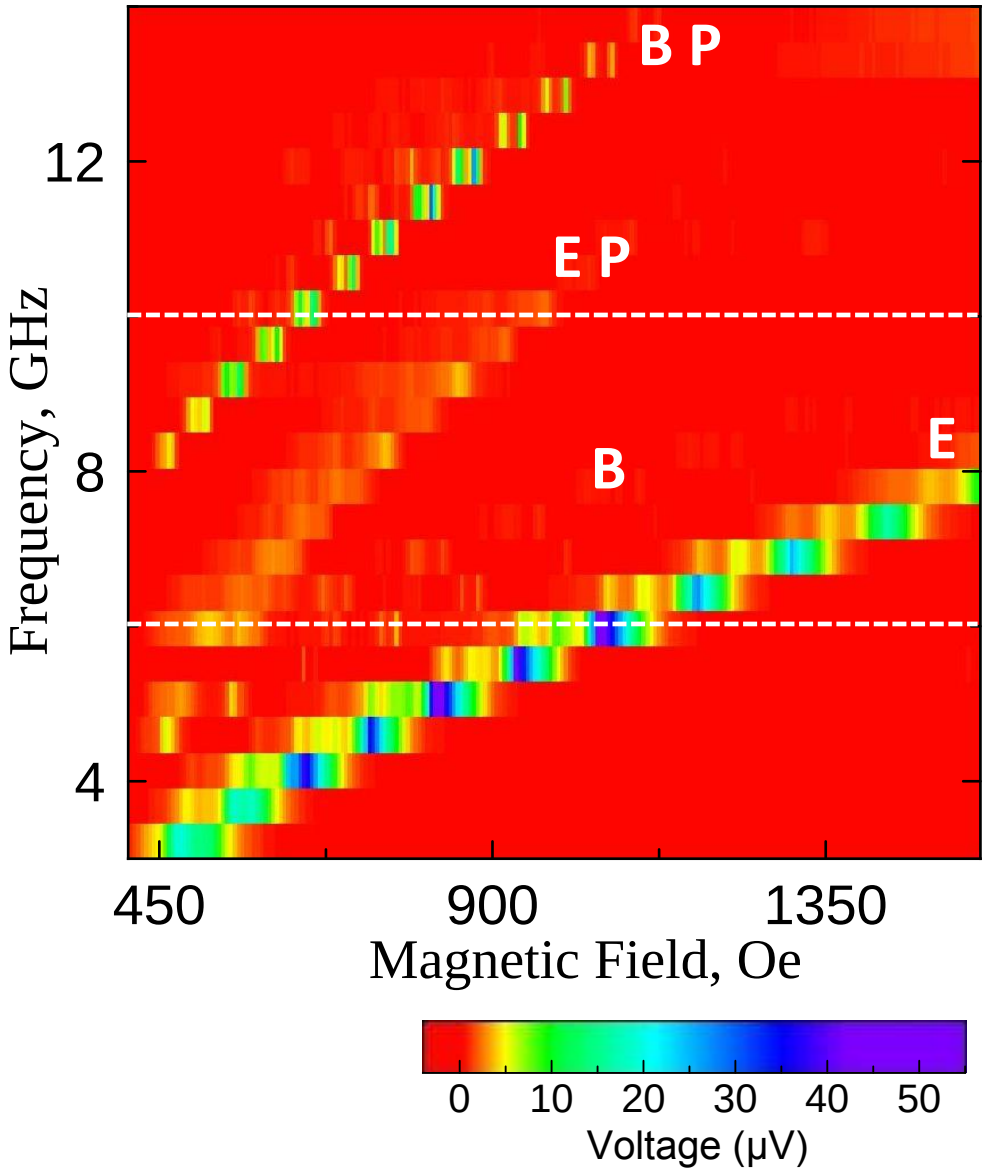

Figure 6.2 Voltage spectra at I_{DC} =2.2mA and I_{rf}=0.3mA as a function of RF frequency. E, B, EP, BP indicates modes that can be identified as edge mode, bulk mode, and parametrically driven edge and bulk mode. Dotted white lines indicate applied RF at 6 and 10 GHz, corresponding to one and two modes excited parametrically.

Two additional modes at higher frequencies, with frequencies close to twice these of edge and bulk modes, can be identified as parametrically excited edge and bulk modes (marked as EP and BP in the figure). Both spin wave modes can be parametrically excited. Even though the same DC magnitude, and as a result Oersted field, is used in the measurement, parametrically excited modes drive frequency is not exactly twice as the direct excitation of bulk and edge modes. This is due to different excitation amplitude of parametric resonance and nonlinear frequency shift as oscillation amplitude increases. As we can see, bulk mode parametric resonance has bigger signal than direct excitation of bulk mode, but edge mode parametric resonance has weaker signal than direct excitation of edge mode. This again confirms that bulk mode is more aligned to the hard axis field, while edge mode excitation region, is more parallel to the nanowire despite the perpendicular field applied. Higher order modes are also excited and visible, which is clearer in Fig 6.3 and we will come back to later. Dotted white line in Fig 6.2 corresponds to frequencies where there is only one mode parametrically excited at 6GHz and at 10GHz where there are two parametrically excited modes.

In order to compare directly and parametrically excited oscillation, we plot voltage signals at I_{DC} =1.8mA and 6GHz I_{rf} with varying magnitudes In Fig 6.3. From Fig 6.2, we can identify the mode at around 500Oe to the parametrically excited edge mode, and the mode at around 1100 Oe to be the directly excited edge mode. Directly excited edge mode grows in magnitude as I_{rf} increases, but is always visible even at low I_{rf} current. This is expected for direct excitation, the voltage signal of which has square dependence on the I_{rf} and we start seeing the voltage signal once it is above the noise level. The parametrically excited edge mode, on the other hand, has a threshold behavior, but it grows much faster in magnitude after the threshold. Also as oscillation amplitude and voltage grow, linewidth also becomes wider and more asymmetric,

which is caused by the nonlinearity of the dynamical system. There is also a nonlinear resonance frequency (field) shift that is associated with the growth of oscillation amplitude. It can be seen that higher order edge modes, with lower fields, can also be parametrically excited with higher threshold currents, which is consistent with higher critical currents of higher order modes. [Chapter 4] In directly excited edge mode, however, mainly the fundamental mode is seen in the I_{rf} range of measurement due to the small oscillation amplitude. The lineshape of the direct linear excitation of edge mode is mainly symmetric, which means that it is mainly pure spin current excited, instead of Oersted field driven [12], and indicates a stronger spin torque contribution than Oersted field contribution in our nanowire. This is due to the small Oersted field from current in Pt layer acting on Py layer in the spin Hall geometry, which is less than 10% of external applied field according to our estimation. The quantitative voltage values are plotted and fitted to in Fig 6.4(a, b). We fit PR voltage up to a value where oscillation is still non–chaotic and can get I_{rf} threshold from the fitting. Direct excitation of edge mode voltage magnitude can also be fitted up to voltage where it is still linear oscillation pretty well. In Fig 6.5, we plot voltage spectrum at 10GHz where parametrically excited bulk mode and edge mode are excited at around 700 Oe and 1000 Oe respectively, as a function of I_{rf} at 4 different I_{DC} currents. It can be seen that, at each I_{DC}, there is a threshold I_{rf} for the bulk mode and edge mode respectively, and as I_{DC} increases, spin torque from spin Hall effect lowers the effective damping of the modes, and threshold currents I_{rf}, which is proportional to the static effective damping, become smaller for both bulk mode and edge mode. At the same I_{rf} current, much higher oscillation amplitude can be excited for higher I_{DC} currents compared with a smaller I_{DC}. Also higher order spin wave modes are excited in the PR bulk mode, similar as higher order parametrically excited

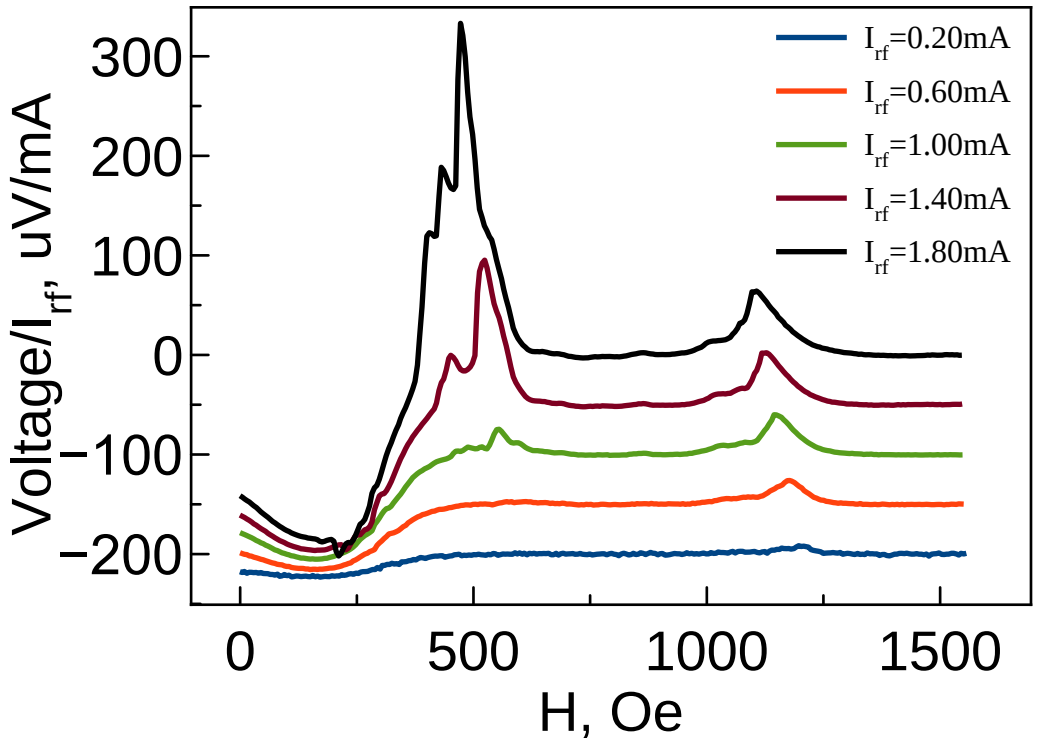

Figure 6.3 Voltage signals at I_{DC} =1.8mA and 6 GHz RF as a function of I_{RF}. (offseted)

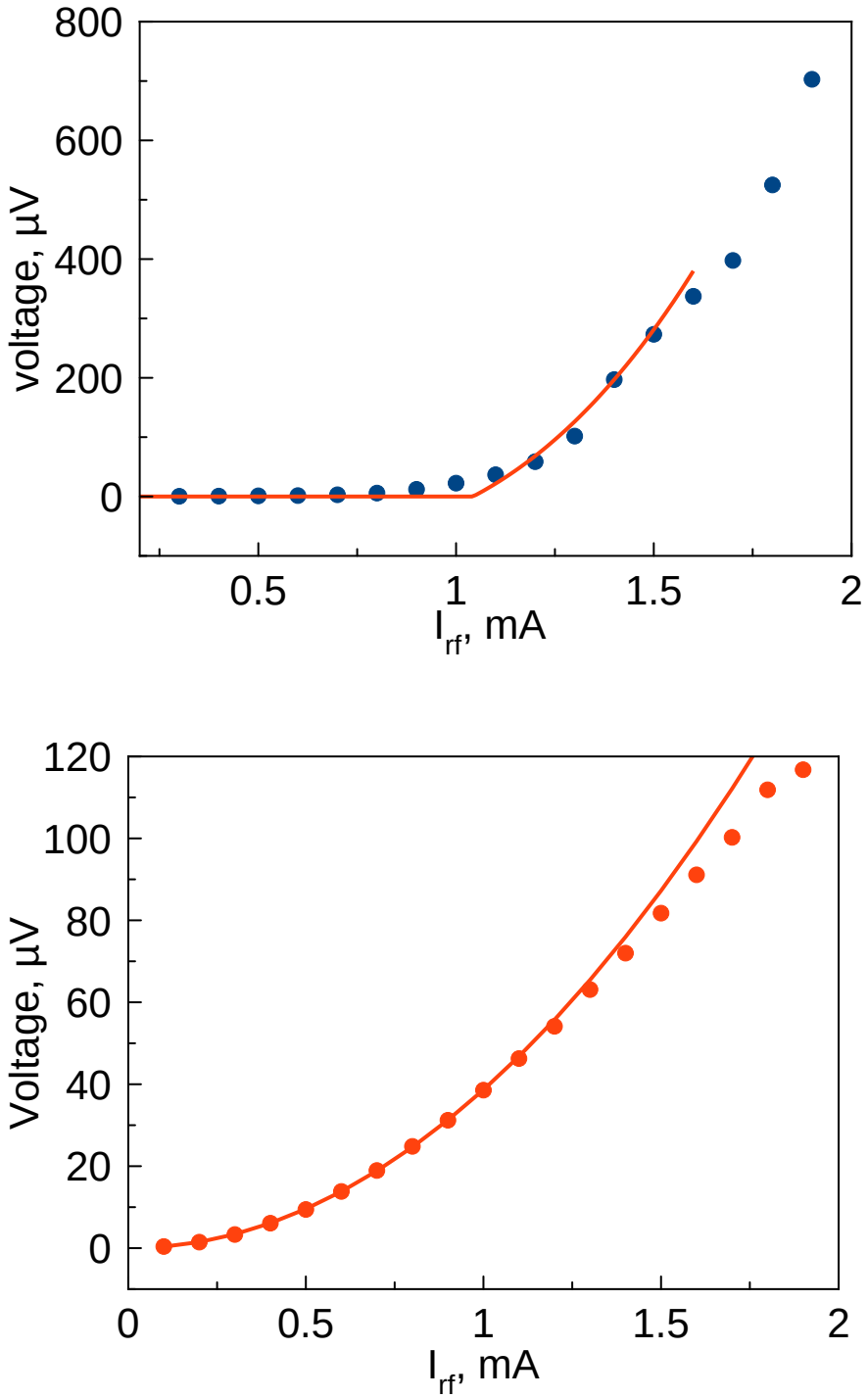

Figure 6.4 (a) Parametrically excited edge mode and normal edge mode voltage dependence on I_{rf} are plotted in dots and fittings plotted in lines in (a,b) respectively.

edge modes in Fig 6.3. However, parametrically excited edge mode doesn't show higher order spin wave modes at 10GHz, even at higher signal and oscillation levels than Fig 6.3 at 6GHz. It might be the coexistence of high amplitude parametrically bulk mode is limiting the higher order edge more, or that high order modes is less pronounced at higher fields. In parametrically excited edge modes, there is splitting in the peak, which might due to oscillation at two edges of the nanowire. Both edge and bulk modes become increasingly more asymmetric at higher oscillation amplitude, and show increase in resonance field as oscillation increases as expected. In Fig 6.6(a, b) quantitative voltage magnitude is plotted for parametrically excited bulk and edge mode as a function of I_{rf} for different I_{DC}. It can be clearly seen that the threshold at which voltage starts to quickly grow above 0 lowers as I_{DC} increases, for both bulk and edge mode. We can fit each trace to the model and get I_{rf} threshold currents from the fitting.

Using the fitted RF threshold current values from bulk and edge mode as a function of I_{DC} in Fig 6.6, we can extract the critical currents I_c for these two modes from a linear fit and extrapolation, as in Fig 6.7. Extrapolation to I_{DC}=0 mA yields the RF threshold with 0 DC current, which is much higher than the RF current range used in our experiment, and explains why no parametric resonance can be excited in our chase without the help of spin Hall effect. Extrapolation to I_{rf}=0 mA yields the critical currents I_c of bulk and edge mode. These values are higher than the critical current values where we first observe auto-oscillations in these kind of devices[Chapter 4], which makes sense since auto-oscillation is thermally assisted and thermal noise would lower the critical current. As for the different slopes for bulk and edge mode, they are mainly due to different magnetization directions between the bulk and edge excitation magnetization area. As a result, spin Hall efficiency and parametric drive efficiency differs for these two modes.

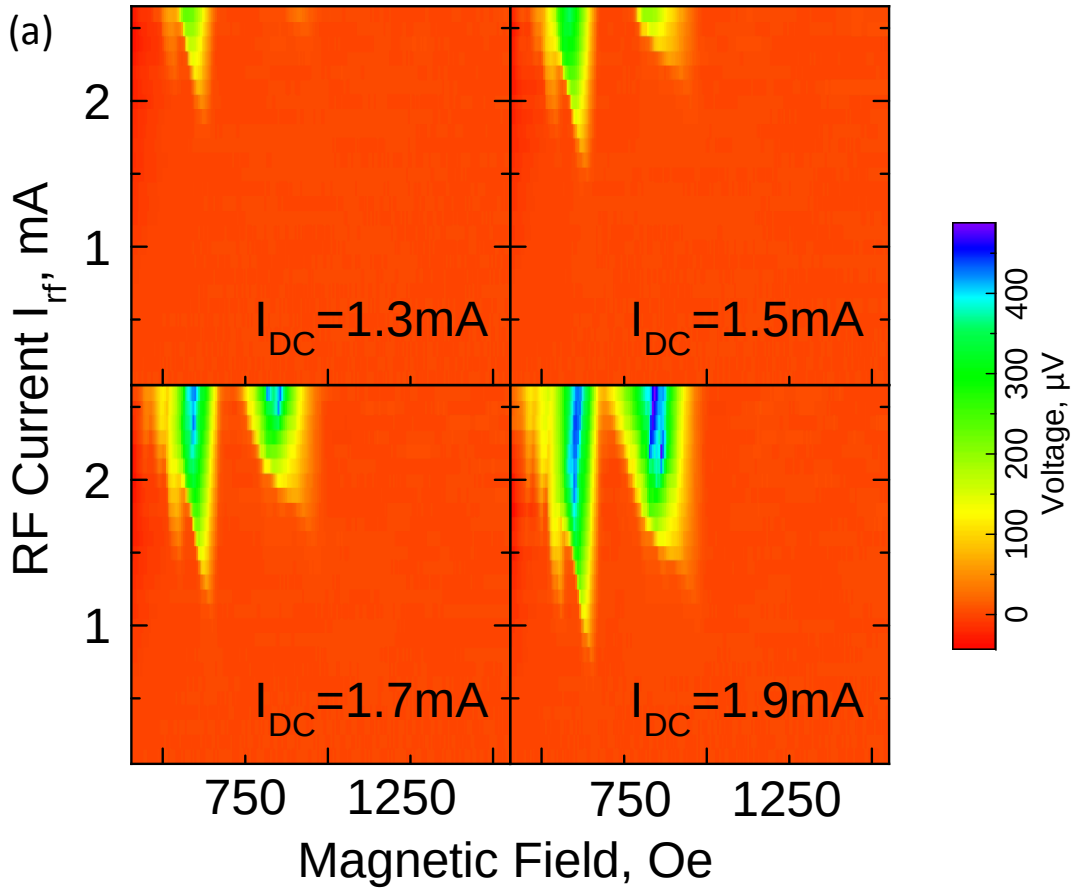

Figure 6.5 Voltage spectra as a function of I_{rf} for 4 I_{DC} values at 10GHz.

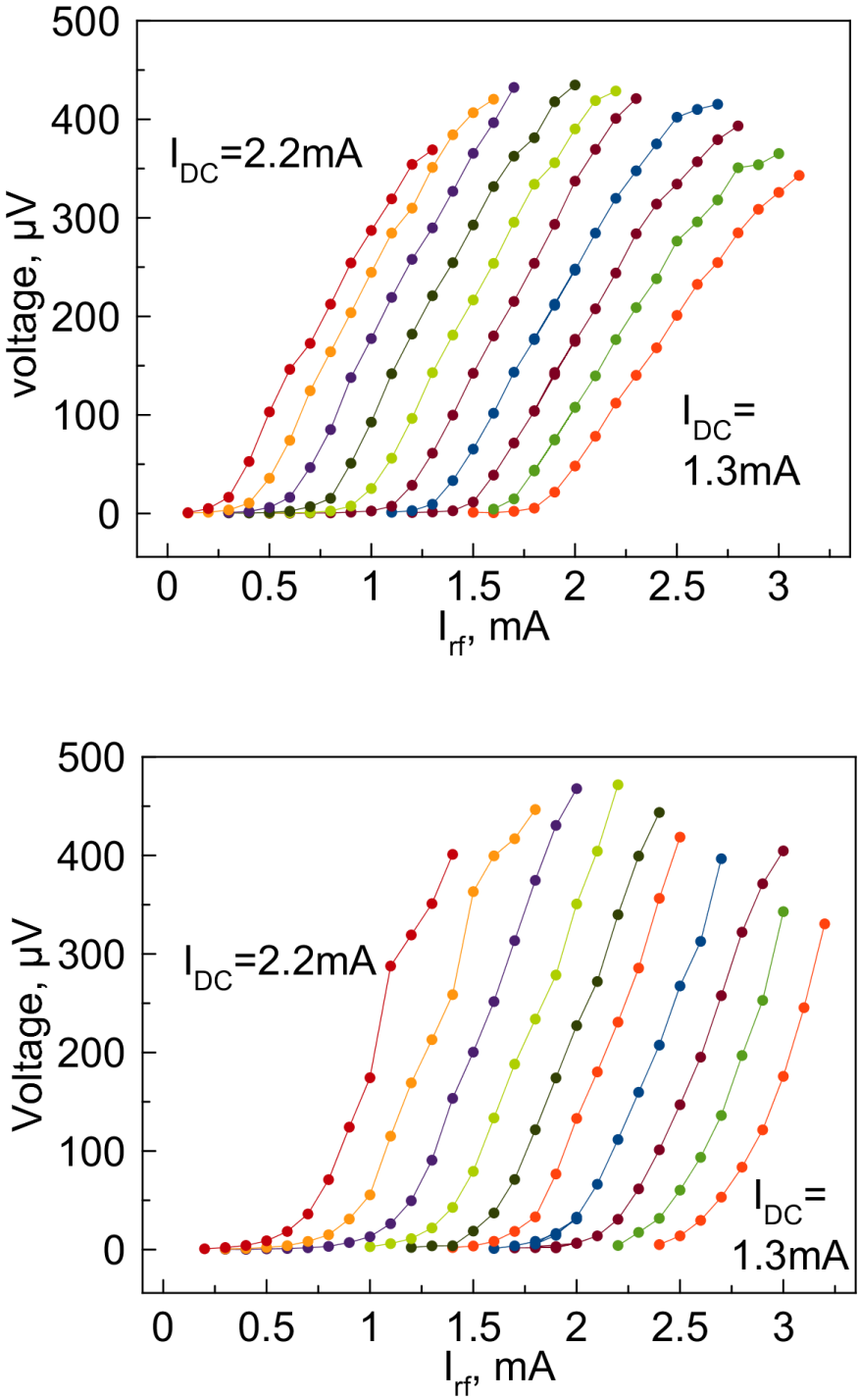

Figure 6.6 Parametrically excited bulk mode and edge mode voltages dependence on I_{rf} for each mode plotted in dots respectively in (a,b) at different I_{DC}. Lines are guide for eyes.

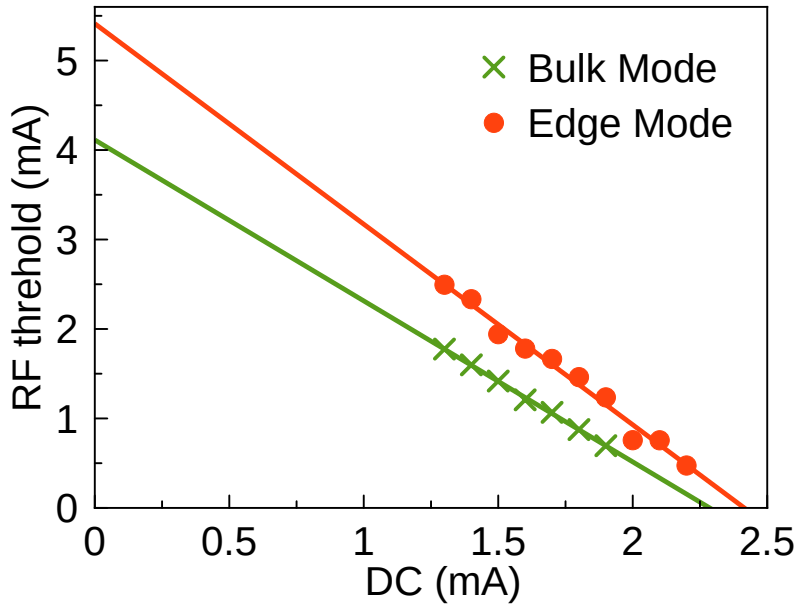

Figure 6.7 Fitted RF threshold as a function of I_{DC} for bulk mode (in green crosses), edge mode (in red dots), and linear fittings in lines.

6.3 Discussion

In conclusion, we have demonstrated that parametric resonance of spin-wave modes in Pt/Py nanowires can be excited at small RF current. Compared with the linearly excited spin wave modes, parametric resonance show strong non-linearity and oscillates at half the frequency of the drive. It also excites multiple dynamic modes of short wavelength, allowing study of the otherwise hard to excite dynamics. Injection of pure spin currents provides an efficient mechanism for control of the parametric instability, and allows the precise determination of spin wave modes dynamical properties. Our studies open up possibilities of studying dynamical characteristics and complex nonlinear phenomena in nanomagnets. Also the wide range of control of resonance amplitude at the same microwave drive, combined with the electrical measurement and low threshold of the

system makes it useful for potential applications such as parametric amplifiers of spin waves.

1. Slonczewski, J. C. Current-driven excitation of magnetic multilayers. *J. Magn. Magn. Mater.***159**, L1–L7 (1996).
2. Berger, L. Emission of spin waves by a magnetic multilayer traversed by a current. *Phys. Rev. B* **54**, 9353–9358 (1996).
3. Haney, P. M., Lee, H.-W., Lee, K.-J., Manchon, A. & Stiles, M. D. Current induced torques and interfacial spin-orbit coupling: semiclassical modeling. *Phys. Rev. B* **87**, 174411 (2013).
4. Dyakonov, M. I. & Perel, V. I. Possibility of orienting electron spins with current. *JETP Lett.***13**, 467 (1971).
5. Hirsch, J. E. Spin Hall effect. *Phys. Rev. Lett.* **83**, 1834–1837 (1999).
6. Zhang, S. Spin Hall effect in the presence of spin diffusion. *Phys. Rev. Lett.* **85**, 393–396(2000).
7. Ando, K. *et al.* Electric manipulation of spin relaxation using the spin Hall effect. *Phys. Rev. Lett.* **101**, 036601 (2008).
8. Fan, X. *et al.* Observation of the nonlocal spin-orbital effective field. *Nat. Commun.* **4**, 1799(2013).
9. Hoffmann, A. Spin Hall effects in metals. *IEEE Trans. Magn.* **49**, 5172–5193 (2013).
10. Bai, L. *et al.* Universal method for separating spin pumping from spin rectification voltage of ferromagnetic resonance. *Phys. Rev. Lett.* **111**, 217602 (2013).
11. Sankey, J. C. *et al.* Spin-transfer-driven ferromagnetic resonance of individual nanomagnets.*Phys. Rev. Lett.* **96**, 227601 (2006).
12. Liu, L., Moriyama, T., Ralph, D. C. & Buhrman, R. A. Spin-torque ferromagnetic resonance induced by the spin Hall effect. *Phys. Rev. Lett.* **106**, 036601 (2011).
13. Mecking, N., Gui, Y. S. & Hu, C. M. Microwave photovoltage and photoresistance effects in ferromagnetic microstrips. *Phys. Rev. B* **76**, 224430 (2007).
14. McMichael, R. D. & Maranville, B. B. Edge saturation fields and dynamic edge modes in ideal and nonideal magnetic film edges. *Phys. Rev. B* **74**, 024424 (2006).
15. Ulrichs, H., Demidov, V. E., Demokritov, S. O. & Urazhdin, S. Parametric excitation of eigenmodes in microscopic magnetic dots. *Phys. Rev. B* **84**, 094401 (2011).

16. Demidov, V. E., Urazhdin, S., Edwards, E. R. J. and Demokritov, S. O. Wide-range control of ferromagnetic resonance by spin Hall effect. *Appl. Phys. Lett.* **99**, 172501 (2011).

17. Rousseau, O. and Viret, M. Interaction between ferromagnetic resonance and spin currents in nanostructures. *Phys. Rev. B* **85**, 144413 (2012).

18. Wang, C., Seinige, H. and Tsoi, M. Current-driven parametric resonance in magnetic multilayers. *J. Phys. D: Appl. Phys*. **46** 285001 (2013)

19. Hahn, C., de Loubens, G., Viret, M., Klein, O., Naletov, V. V. and Ben Youssef, J. Detection of Microwave Spin Pumping Using the Inverse Spin Hall Effect. *Phys. Rev. Lett.* **111**, 217204 (2013)

20. Bracher, T., Pirro, P., Obry, B., Leven, B., Serga, A. A. and Hillebrands, B. Mode selective parametric excitation of spin waves in a $Ni_{81}Fe_{19}$ microstripe. *Appl. Phys. Lett.* **99**, 162501 (2011)

21. Guo, F., Belova, L. M. and McMichael, R. D. Parametric pumping of precession modes in ferromagnetic nanodisks. *Phys. Rev. B* **89**, 104422 (2014)

22. Urazhdin, S., Tiberkevich, V. and Slavin, A. Parametric Excitation of a Magnetic Nanocontact by a Microwave Field. *Phys. Rev. Lett.* **105**, 237204 (2010)

23. Ulrichs, H., Demidov, E. V., Demokritov, O. S. and Urazhdin, S. Parametric excitation of eigenmodes in microscopic magnetic dots. *Phys. Rev. B* **84**, 094401 (2011)

24. Edwards, E. R. J., Ulrichs, H., Demidov, E. V., Demokritov, O. S. and Urazhdin, S. Parametric excitation of magnetization oscillations controlled by pure spin current. *Phys. Rev. B* **86**, 134420 (2012)

25. Epshtein, E. M. and Zilberman, P. E. Parametric instability of a magnetic junction under modulated spin-polarized current. *J. Magn. Magn. Mater.* **324**, 880 (2012)